THE UNIVERSITY OF CHICAGO

GEOMETRIC AND BIOELECTRIC CUES TO CELL MECHANICS

A DISSERTATION SUBMITTED TO
THE FACULTY OF THE DIVISION OF THE PHYSICAL SCIENCES
IN CANDIDACY FOR THE DEGREE OF
DOCTOR OF PHILOSOPHY

DEPARTMENT OF CHEMISTRY

BY
ERIK N. SCHAUMANN

CHICAGO, ILLINOIS
AUGUST 2020

This work is dedicated in memory of Molly M. Yerger, 1969-2016. Thank you for always encouraging me and believing in me, whether it was to climb mountains or engage with science, even when I had such little belief in myself. I love you and miss you, Aunt Molly.

The cause why these can never attain to their intentions is this: Because by this way, Nature will not be extracted nor separated with human dis-junctions, as by terrene Glasses and Instruments.

Paracelsus, *Of the Transmutation of Metals*

TABLE OF CONTENTS

LIST OF FIGURES

LIST OF TABLES

ACKNOWLEDGMENTS

This work reflects not only the scientific developments during my time as a graduate student, but the personal developments in my life as well. As such, acknowledging the true number of people who have contributed in one way or another to this dissertation is not practically feasible. Nevertheless, certain key figures have played exceptionally important roles in this process, and I will attempt to mention as many of them as I can here. Whether or not I would have made it to the stage of writing a dissertation without them is unknowable, but I suspect I would not have, and in any case, without their influence this work would look dramatically different. To everybody listed here and to everybody else, you have my perpetual thanks.

My thesis advisors, Margaret Gardel and Bozhi Tian, have both been important positive influences throughout my time in graduate school. As my advisor since first year, Margaret in particular has been an incredible role model both as a scientist and as a person. While my time in the Tian Lab has been considerably shorter, I have learned so much and grown so much as a scientist in these last two years. I am honored to have had the chance to work with both of them.

I have been fortunate enough to grow up with a family that has always emphasized the important of a love of learning, and which has continued to be supportive throughout my graduate school career. My mother, father, stepmother, and stepfather have all been essential in bringing me to this point. Thank you for everything. My aunt and uncle Elinor and Mark provided much needed familial support during my time in California and have always been a joy to see. My uncle Dale imbued within me a love of nature that helps remind me to continue with scientific research because it can help make the world a better place for all. My aunt, Molly, to whom this work is dedicated, was beloved by all for her kindness, wit, brilliance, and compassion. She was always present to support me, from the first time I said I wanted to rock climb, through my academic struggles in high school, and beyond. Though her suicidal ideation came to a tragic conclusion, her memory continues to shape me and to

make me a better person, day by day.

Finally, my friends and coworkers here in Chicago and elsewhere have all been truly wonderful people to me. I simply cannot express enough gratitude. Kade Head-Marsden and Becca Thompson all got me through the first year of grad school and were great friends afterwards. Kelliann Koehler has never stopped advocating for me to advocate for myself, and I am profoundly thankful for her every day. Yvonne Beckham has perpetually been both supportive and helpful, and many of my fondest memories have taken place around lunches in her office. Jenna Bagley is a stellar person and a great friend. Michael Busch, who I stayed with in California, has been supportive for nearly ten years. I will always remember cramming down fancy mochi and somehow watching all of Evangelion way past anybody's bedtime. Tim Fessenden, Patrick McCall, Samantha Stam, and Guillermina Ramirez-San Juan were all great to have as senior grad students to learn from and talk to. Dani Scheff's laughter fills any room she occupies, and I greatly appreciate having somebody else with whom to ironically - but secretly unironically - enjoy Malort. Tracy Chmiel has been a welcome presence in the desk across the corner, and I am honored to work with somebody so intelligent, warm, and thoughtful, all at the same time. Steven Redford has been a terrific friend, as a coworker and source of interesting and helpful conversations about image analysis, but as we can all agree is far more important, as a fellow appreciator of Mongolian biker folk metal.

ABSTRACT

As our understanding of multi-scale biological phenomena has improved, it has become increasingly evident that much remains to be learned by examining the mechanical and electrical characteristics of cells. This realization has occurred alongside technological developments enabling us to map out cell-level biological processes with unprecedented spatial and temporal resolution, both in terms of our ability to detect such processes, and increasing specificity of targeted perturbations. In this dissertation, I present the results of research I have conducted to gain further insights into these areas. This research has been decisively multidisciplinary, with inspiration coming from across the natural sciences. It is divided into two broad categories based on the physical phenomena examined in relationship to cellular behavior. One segment is devoted to how colonies of epithelial cells distribute mechanical forces to their environments. In the other segment, I examine the impacts of highly localized electrical stimulation on calcium signaling within colonies of airway smooth muscle cells.

The importance of mechanical considerations to cell biology, arising from both the cells themselves as well as their environment, has long been recognized. In the last few decades, however, mechanobiology has seen a resurgence in interest, owing to increased recognition of the physiological impacts mechanical forces and material properties can induce, and the introduction of new techniques to quantify these effects. Traction force microscopy serves as an example of the latter, as it enables us to measure the location, magnitude, and direction of stresses that cells exert on their environments, and it can do so with subcellular spatial resolution and with good temporal resolution. I have employed traction force microscopy in order to better understand how colonies of epithelial cells organize their traction stresses. In the process of doing so, a previously unreported pattern of stress distribution emerged. In collaboration with theorists who developed a new model of how cell shape emerges and is connected with traction stress exertion, we clarified the origins of the new pattern as being a consequence of fluidity within colonies. We further validated this model with a variety of experimental scenarios.

Electric fields have also been recognized as important aspects of cell physiology since the 1950s, yet the pace of research in bioelectronics is rapidly increasing. One contributor to this rise in interest is the development of new, nanoscale devices that can interface with cells and subcellular components. This has allowed us to rethink the fundamental science of electric fields interacting with cells, as well as engineer new applications with therapeutic potential. Silicon nanowires are one such type of device, which display many desirable properties such as good biocompatibility, and a wide array of functionalities that can be encoded into their structure during synthesis. I have employed doped silicon nanowires with a p-i-n core-shell dopant profile, which have previously been demonstrated to produce electric currents in response to light stimulation, in conjunction with human airway smooth muscle tissues. I found that nanowire stimulation induced changes in calcium signaling for associated cells, including directly stimulated cells and their neighbors.

CHAPTER 1

INTRODUCTION

1.1 Mechanical forces and electric fields in cells and tissues

If there is a single guiding principle behind the research presented herein, it is the exploration of how physical forces operate on systems at different levels of biological organization, namely cells and tissues. A strictly reductionist-constructionist worldview[1] holds that biological molecules are governed by their chemistries, which determine their reactivity and conformation. This allows information that is durably encoded in the identities of nucleotides that compose a strand of DNA to be transcribed to the more readily accessible format of RNA, which can then be translated by the machinery of ribosomes into peptide sequences. Here again, chemical interactions govern the form and function of proteins, which go on to provide the essential identities of individual cells, which interact to form tissues, which interact to form organs, then biological systems, individuals, psychologies, societies, and economies. If there is a singular defining moment for this perspective, it is likely in 1953, when the structure of DNA was published[2]. For successive generations of biologists, DNA served as a foundation of understanding. Just as molecules such as DNA are defined by the properties of their component atoms, organisms are defined by their genes. Cells, then, are treated as "bags of chemicals," containers for an intricate network of biochemical reactions that carry out the functions vital to life. It is difficult to overstate the successes of this way of thinking - the contributions of molecular biology to disease management alone have saved countless lives, and the utility of having a molecular foundation for constructing our knowledge of biology gives it a structure that is organized and comprehensible.

Despite the tremendous advances achieved with a DNA and molecule-oriented approach to cell biology, research in recent decades has exposed some of its limitations. For instance, in the picture described above, mechanical forces originate from sliding between actin filaments and myosin molecular motors, but they only become physiologically relevant at relatively

large length scales, where specialized organs for locomotion and fluid and gas transport are necessary. Conversely, electric fields are mostly considered at the molecular scale, where they are among the dominant factors in governing the conformation and interactions of specific molecules such as enzyme reactivity, as well as factors such as solubility and phase-phase separation. In this perspective, the largest scale of electrical relevance is probably at ion channels, where the cell membrane potential can tune the transport of ions into and out of cells and generating action potentials, which the brain uses as signals. While it is true that cell mechanics are important for transporting fluids and moving muscles, and electric fields are important for molecular interactions, they are also each important to biology at scales beyond their "prescribed limits." Mechanical and electrical considerations are actually relevant throughout all the various levels of biological organization[3][4][5][6]. The intricacy of cellular signaling and responses thus extends beyond the realm of chemical reactions - the "bags of chemicals" are in fact influenced by and exert mechanical forces and electric fields. The core tenet of my research, then, has been to use new experimental and theoretical developments to characterize these mechanical and electrical behaviors, in order to integrate them with the foundation of molecular understanding.

1.2 Model of a cell as a mechanical and electric entity

In order to situate the methods and results of this research within the context of the broader literature, I will construct here a brief overview of a cell, with the essential components relevant to the processes I have examined.

1.2.1 The mechanical cell picture

The mechanical picture of a cell begins with the cytoskeleton. Actin monomers, known as G-actin, are globular proteins that can polymerize to form double helical filaments, known as F-actin[7]. As the filamentous components providing shape and structural integrity to cells, the general cellular network of F-actin is referred to as the actin cytoskeleton. These F-actin filaments can, in turn, assemble into a wide variety of architectures, depending on the cell environment. Broad, flat protrusions on the leading edge of migrating cells known as lamellipodia tend to contain highly branched F-actin structures[8]. Stress fibers represent another possible arrangement of F-actin, where the individual filaments are bundled and crosslinked with one another to form long fibers[9][10]. F-actin is polar, in that it has distinct ends referred to as "barbed" and "pointed," where actin polymerization and depolymerization respectively occur[7]. Myosin motors also decorate F-actin. The myosin family of motor proteins consists of a number of different varieties that all share some common features. They have binding heads that attach to F-actin and allow them to act as crosslinkers between different filaments. Most importantly, they undergo a cyclical power stroke process that results in them pulling on actin filaments. Combined with the crosslinking ability of myosin, this means that myosin can cause F-actin filaments to slide relative to each other[11]. This action, coupled with the forces generated from actin polymerization and depolymerization[12], are the primary contributors to force generation within the cytoskeleton.

While the totality of the different pathways involved in regulating actomyosin contractility is beyond the scope of this picture, the RhoA signaling pathway is of particular importance in influencing contractility[13][14]. RhoA is a small GTPase, and as such can cycle through GTP with Rho GTPase activating proteins (RhoGAPs) aiding in GTP hydrolysis and Rho guanine nucleotide exchange factors (RhoGEFs) aiding in exchanging hydrolyzed GDP for fresh GTP[15]. One of the functions of RhoA is to phosphorylate the cytoskeletal regulatory protein ROCK, which itself can serve to phosphorylate myosin light chain kinase (MLCK). The function of MLCK is to promote myosin contractility by phosphorylating the regulatory

myosin light chain on myosin-II, the dominant form of myosin in muscle and non-muscle animal tissues[16].

Focal adhesions (FAs) are protein complexes found predominantly at cell edges[17]. They form the anchoring ends of stress fibers, and they contain integrin proteins that anchor to the local cellular environment[9]. As such, FAs are the interface between the substrate and the cytoskeleton, and they are the locations where forces generated in the cytoskeleton are exerted on the environment (Figure 1.1)[18]. Besides integrins, FA complexes possess a number of proteins serving various structural and functional means, including paxillin, which links integrins to the rest of the FA structure; talin, which binds to paxillin and connects it to stress fibers; vinculin, which also plays a linking and signaling role and is recruited during the FA "maturation" process; as well as many others[19]. As part of the dynamic cell conditions, FAs first form in a nascent state, then mature to form large plaques, before eventually being disassembled and reforming elsewhere in a general lifecycle known as focal adhesion turnover[20]. This process is most notably essential for cell motion, where FAs must be assembled at the leading edge to anchor the cell as it moves forward, and disassembled at the trailing edge as it retracts[21]. Furthermore, as sites of important mechanical transmission, a number of other molecular actors relevant to cell mechanics are present or enriched at focal adhesions[22]. This namely includes the components of the RhoA pathway, including ROCK and Rac.

A number of junction complexes exist for both mechanical communication and structural integrity between cells. Adherens junctions (AJs) are the most similar to focal adhesions, in that they form at the ends of stress fibers and contain proteins that allow for interface (Figure 1.1) formation[23][24]. In AJs, catenins link the cytoskeleton to other junctional components. Another type of AJ-associated protein comes in the form of cadherins, which are transmembrane proteins with extracellular domains that can ligate to calcium ions[25]. When two cadherins of different cells interact with the same calcium ion, they form a homodimer complex that serves as the nascent site of the eventual AJ, once the intracellular

domains form connections to the cytoskeleton via catenins[26].

Tight junctions are also an important class of cell-cell junction in epithelial and endothelial

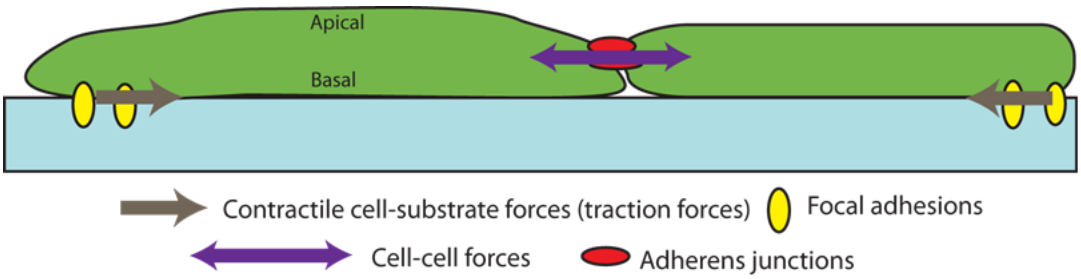

Figure 1.1: Schematic of force transmission from cells. Cells generated in the actomyosin cytoskeleton can be transmitted from cells to their local substrates through focal adhesions. Forces may also be transmitted from the cytoskeleton of one cell to another, which occurs at the cell-cell interface complexes known as adherens junctions.

cells. They are primarily found in the apical region along cell interfaces, and are responsible for maintaining cell polarity, preventing leakage from the intercellular space, and transmitting extracellular signals to the intracellular space[27][28]. Previous work has established the importance of two particular tight junction proteins, zonula occludens 1 and 2 (ZO-1/2) in defining the mechanical characteristics of cells, as well. Specifically, Fanning, et al.[29], and Choi et. al.[30], found that Madin-Darby canine kidney cells expressing a ZO-1/2 double knockdown genotype (ZO-1/2 dKD) display cell-cell junctions that more closely resemble straight lines when viewed from above, and their shapes bear a closer resemblance to regular hexagons when compared with the wild type. This is suggestive of increased tension along the junctions, a proposition which is further supported by the molecular signaling that takes place at tight junctions. Choi et al. observed that ZO-1 and 2 act as inhibitors to Shroom3, a cell shape regulator that aids in recruiting ROCK. ZO-1/2 dKD, then, increases the presence of Shroom3 at apical junctions, which leads to ROCK recruitment and therefore higher contractility.

1.2.2 The Bioelectronic Cell Picture

Our understanding of the subcellular actors relevant to electrical processes in cells tends to center on only a few key components, relative to the numerous pathways that have been elucidated in cell mechanics. There are a number of likely reasons for this. One is the difficulty in applying patch clamp methods, the most widespread electrophysiological technique, to subcellular questions - an issue this work hopes to partially address through the use of nanowires as vehicles for stimulation. Another key difficulty is the apparent greater variability in cellular responses to electrical stimulation. The question of how a given cell type responds to electrical fields can have a dramatically different answer, depending on the cell under question. Neurons, myocytes, and pancreatic β cells, for instance, are capable of transmitting electrical signals in the form of ionic flows, and are thus considered to be electrically excitable cells. Other cells may not interact so directly with electric fields, but may still be responsive through, e.g., electrophoresis of membrane components or mechanical response to electro-osmotic flows in the surrounding medium[31][32][33]. This manifests in a variety of different electrically induced processes in excitable and non-excitable cell types, including preferential motion towards either cathodes or anodes depending on cell type[34], the expression of pre-angiogenic factors[35], or hormone release[36]. Nevertheless, there are a number of recurring components that are involved in many electrical responses, which I will describe here.

First, it is important to note that most biological molecules are in an aqueous environment and are charged to some degree. As noted in Section 1.1, electromagnetic interactions are an essential aspect to biological behaviors on the molecular scale, with manifestations apparent in contexts such backbone hydrogen bonding in proteins, or in charged binding sites for enzymes. Certain key biomolecules, namely DNA, are highly negatively charged such that close packaging in nucleoli requires the presence of positive counter-ions to mitigate Coulombic repulsion. The most physiologically relevant aspect of charge regulation in cells, however, is the maintenance of the cell membrane potential. The predominance of negatively

charged species in the intracellular space results in a negative resting potential, measured relative to the exterior. Changes in the relative concentration of positively and negatively charged ions, whether they originate from internal mechanisms or exogenous stimulation, may change this potential, yielding either depolarization - a positive potential - or hyperpolarization - an even more negative one. When discussing cell-level electrical processes, this membrane potential is frequently the dominant consideration, as changes to it can have strong physiological impacts. Most notably, the membrane potential is the primary factor governing the operation of voltage-gated ion channels.

The most direct way that excitable (and certain non-excitable) cells respond to electric fields is with ion fluxes mediated by voltage-gated ion channels. Such channels exist for calcium, potassium, sodium, and chloride ions, and they may respond to either depolarized or hyperpolarized membrane conditions. Voltage-gated calcium channels have drawn particular interest as representatives of this class of channels, in large part due to the well-known biological importance of Ca^{2+} ions[37]. These channels are structured with six transmembrane α-helix domains (S1-S6) organized to form a pore unit, with a membrane-associated loop between S5 and S6[38]. The voltage-mediated operation of these channels arises from S4, which is enriched in positively charged domains, usually arginine[37]. This charge makes the structure electrically responsive, and in the presence of sufficient electric fields, the helix pivots outwards and induces a conformational change that opens the channel and allows Ca^{2+} to move down the concentration gradient from extracellular fluid to cytosol.

Calcium ions, Ca^{2+}, are particularly relevant for bioelectronics. Voltage-gated calcium channels are present in all excitable cell types, and potentially in certain non-excitable cell types too[39], meaning the connection between calcium signaling and electric fields can be direct. Moreover, Ca^{2+} is singularly important to cell physiology. Calcium is a canonical example of a second messenger, a small molecule that is readily transmitted to different cells and can signal for other biochemical pathways to be induced or inhibited. As such, it is the primary transducer for electrical signals to become biochemical information. Calcium

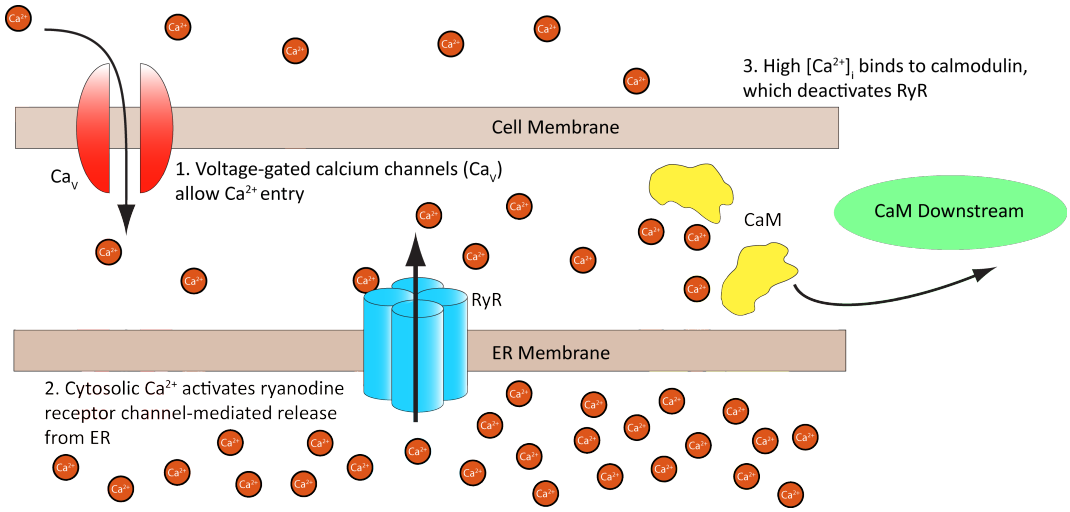

Figure 1.2: Electrical regulation of Ca^{2+} signaling in mammalian cells. Voltage-gated calcium channels (Ca_vs) open in response to transient membrane depolarization, allowing calcium ions to flow into the cytoplasm. This then enables ryanodine receptor channels (RyRs) in the endoplasmic reticulum membrane to open and allow additional Ca^{2+} to enter the cytoplasm and bind to calmodulin (CaM). Sufficient levels of CaM deactivate the RyR, ending the calcium flux, and CaM then participates in numerous additional biochemical pathways.

ion primarily - although not exclusively - functions in concert with calmodulin (CaM), a protein that changes configuration and becomes active upon binding to calcium. Calmodulin itself is very highly conserved for the last 1.5 billion years[37], and its expression is implicated in biological functions as diverse as maintaining smooth muscle tone[40][41] and laying the foundation for the beak shapes of Darwin's finches[42]. Calcium regulation varies substantially between cell types, but in human cells the basic anatomy is consistent (Figure 1.2). The cytosolic concentration of calcium is maintained at a low level, around 100 nm[37]. This is partially accomplished by cation pumps, which continuously move calcium from the cytosol to the extracellular space, where the concentration is around 20,000-fold higher. The largest amounts of calcium, however, are retained in the endoplasmic reticulum (ER). Large calcium fluxes thus arise with concerted action between membrane channels and ER channels, releasing calcium ion at high rates down the concentration gradient to the cytosol, until it is pumped back out to the extracellular space or re-sequestered in the ER. Cells possess the components to follow this basic template in many different ways. A particularly notable mechanism represents the intersection of calcium and G-protein coupled receptor (GPCR)

signaling, in which G-protein stimulates the release of inositol triphosphate, which in turn opens inositol triphosphate receptor channels in the ER membrane[37]. For the purposes of bioelectronic investigations, the most likely source of calcium ion release from the ER is the opening of voltage-gated calcium channels. In this scenario, Ca^{2+} entering the cells can bind to ryanodine receptors (RyRs), which are also ER membrane-spanning channels. RyRs have an indirect biphasic response to calcium, such that the calcium entering from extracellular fluid is sufficient to trigger the channels to open, until increasing concentrations of activated CaM, which inhibits RyRs and causes them to close[43]. In this fashion, transient stimulations may be amplified into larger responses.

1.3 Techniques for Mechanical and Bioelectronic Recording and Modulation

1.3.1 Traction Force Microscopy

Traction force microscopy (TFM) is amongst the most widely used methods for measuring cell mechanical outputs. This is due to its good spatial and temporal precision, its compatibility with other biological techniques, and its relative accessibility. The necessary components are a confocal microscope, fluorescent micro-beads or similar fiducial markers, and a biocompatible elastic substrate, with extracellular matrix-coated polyacrylamide hydrogels being particularly popular choices for the latter.

Figure 1.3 shows the experimental workflow for a basic TFM experiment of the sort employed throughout this thesis. The basic premise of TFM is to take confocal snapshots of fiducial markers at the same position on the substrate surface, both with cells on and cells off. If the markers are sufficiently dense, the displacement of the substrate can be accurately measured, and the forces required to cause such displacements can be inferred. This is done

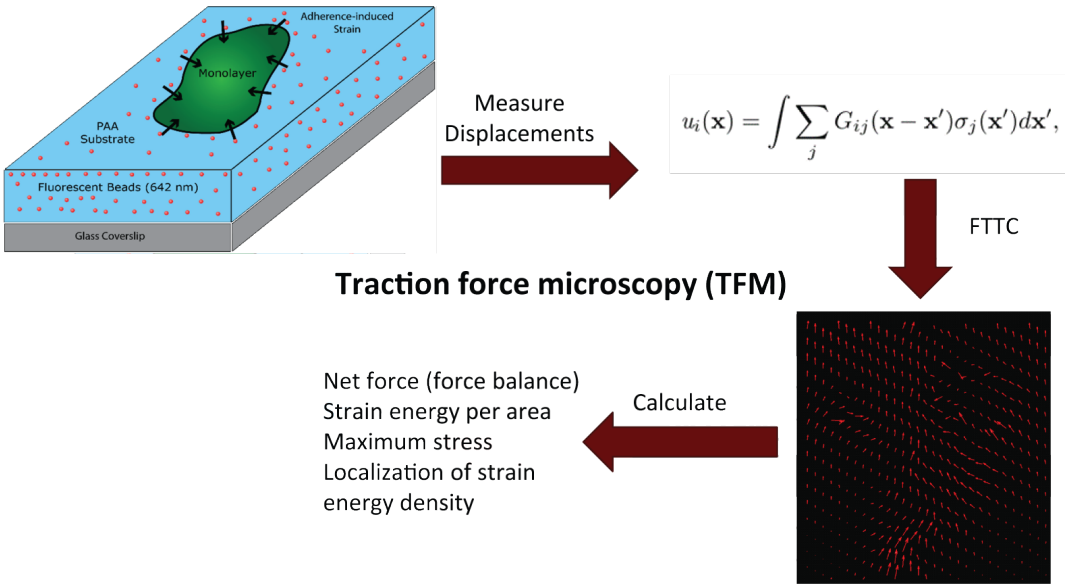

Figure 1.3: Diagram of experimental workflow for traction force microscopy. Using particle imaging velocimetry, strain fields are extracted from pairs of images showing displacements of fiducial markers within the elastic substrate. Fourier transform traction cytometry allows for the rapid and facile computation of the traction stress field. An example of the regularly spaced traction vectors is displayed in the bottom right corner of this diagram. From this field, a number of mechanical properties may be inferred or directly measured.

through the stress-strain relation derived from elasticity theory:

$$\mathbf{u}_{ij}(\mathbf{x}) = \int \sum_j G_{ij}\left(\mathbf{x}-\mathbf{x}'\right)\mathbf{T}\left(\mathbf{x}\right)\mathbf{dx}' \tag{1.1}$$

In this equation, $\mathbf{u}$ is the measured strain field, σ is the stress field that induces the observed strain, and G is the situation-specific Green's function that relates the two. A more compact form of the same equation is $\mathbf{u} = G*\mathbf{T}$, with $*$ denoting convolution. The first step to solving for the stress field is to determine the relevant Green's function. As TFM experiments use mechanically well-characterized substrates that are wide and thick compared to cells, the geometry can be taken to be a linearly elastic isotropic half-space. The relevant Green's function is then the Boussinesq solution, which exists in closed tensor form:

$$G_{ij}(\mathbf{x}) = \frac{1+\nu}{\pi E}\left[(1-\nu)\frac{\delta_{ij}}{r} + \nu\frac{x_i x_j}{r^3}\right],$$

for $i, j \in \{1, 2\}$ and where ν is the Poisson ratio, E is the Young's modulus, and $r = |\mathbf{x}|$. The solution for $\mathbf{T}$ is then found by inverting the equation to infer the stresses. This process introduces its own complexities, however, as it can be very computationally expensive, and as an inverse problem it can suffer from high noise and vary substantially based on small perturbations to initial conditions.

Fourier transform traction cytometry (FTTC) as developed in Butler, et al., 2002 [44] and Sabass et. al., 2008 [45], helps to mitigate both of these problems and is the methodology used for TFM analysis throughout my research. It works by first discretizing the continuous strain field onto a regular grid, and applying the Fourier transform to both sides of equation 1.1:

$$\begin{aligned} \mathcal{F}(\mathbf{u}) &= \mathcal{F}(G * \mathbf{T}) \\ \mathcal{F}(\mathbf{u}) &= \mathcal{F}(G)\,\mathcal{F}(\mathbf{T}) \\ (\mathcal{F}(G))^{-1}\,\mathcal{F}(\mathbf{u}) &= \mathcal{F}(\mathbf{T}), \end{aligned}$$

where $\mathcal{F}$ denotes the Fourier transform. The second line follows from the Fourier convolution theorem, and serves to transform the original problem from a difficult convolution to a matter of matrix multiplication in Fourier space. The original traction stress can then be recovered by applying the inverse Fourier transform to both sides of the equation.

For practical applications, there are several additional steps between acquiring fiducial marker images and producing maps of the cell-induced stresses. The most important of these are image analysis to measure the marker displacements, and separating the signal from low magnitude, high frequency noise. Particle imaging velocimetry methods are a common solution for displacement measuring, because they output a regularly spaced grid by construction, and there are many implementations available for different platforms, including MATLAB and Python. There are many options available for handling noise, including basic frequency cutoff filters and more complex regularization schemes. A standard method is to

employ Tikhonov regularization, with the regularization parameter empirically obtained by minimizing the term $\left|G^{-1}\mathbf{T}-\mathbf{U}\right|+\lambda^2\left|\mathbf{T}\right|^2$ for regularization parameter λ. An appropriately selected value for λ optimizes the tradeoff between the spatial resolution offered by the traction map and the visibility of the signal.

1.3.2 Silicon Nanowires for Bioelectronic Modulation

The following section is adapted from Schaumann and Tian, 2020 [46].

We are amidst a period of growth for bioelectronics — given the toolkit afforded to us from molecular biology, we can now seek to ascertain the roles of each component in response to electrical stimuli. A substantial amount of bioelectronic work has been conducted using macroscopic devices,[34][35][6] but new developments allow us to modulate bioelectronic responses with high spatial resolution, from the scale of tens of nanometers[47][48] to the size of organs [47][49]. In this way it is similar to the advancements being made using optogenetic techniques that have high spatiotemporal resolution relative to systemic genetic manipulations.

We can split modulatory devices into two broad categories, based on whether or not they are freestanding (leadless). In a therapeutic context, freestanding devices offer the advantage of being significantly less invasive to deliver, and their inherently smaller scale means they can be more precisely targeted to specific structures[50]. Substrate-bound or wired devices, on the other hand, can be easily connected to devices that allow for the precise control over the strength and timing of stimulating pulses, as well as recording capabilities.

Among freestanding devices, optically responsive materials are especially appealing because of their fast response time, the ubiquity of light sources that are usable for stimulation, the wide variety of available form factors, and the ability to tune the contributions of different photoresponses. The nature of these responses can be to generate heat (photothermal) [47][51][52], generate a capacitive current (photocapacitive) [47], induce redox reactions

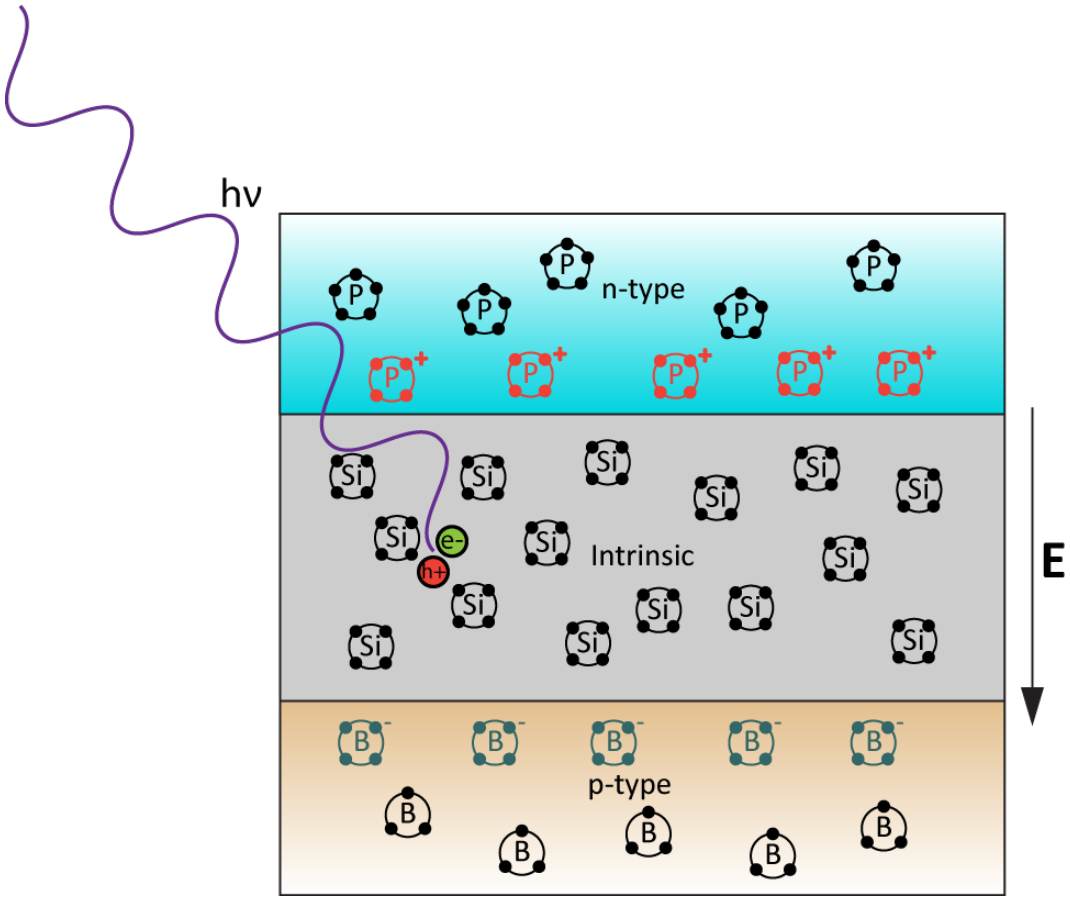

Figure 1.4: Photostimulated electron-hole pair production in a Si p-i-n junction. Sufficiently energetic light can promote an electron from the valence band to the conduction band, leaving behind a hole. The electron and hole then drift away from the intrinsic region - the depletion zone - in accordance with their charge. This charge separation gives rise to the photostimulated electrical phenomena that can be observed in such systems.

(photofaradaic) [53], or to re-emit photons, which can proceed through fluorescence [54] or upconversion [55] mechanisms. Semiconductor nanomaterials, like their macroscopic counterparts, are particularly useful for photocapacitive and photofaradaic applications [56]. Both cases rely on the same fundamental process, wherein photons generate electron–hole pairs in the depletion zone of p-i-n junctions, and the resultant charge separation compels some sort of electrical response (Figure 1.4). Because biological media are rich in electrolytes, the unstimulated state of these materials is defined by the presence of an electrical double layer around the surface. The photo-induced perturbation first disrupts the double layer in what is termed the capacitive response, a large and rapid change in the electrical potential (Figure 1.5, center top). Continued optical stimulation further results in an increased concentration of charge carriers on the device surface, depending on whether the outer material is n-type (electrons) or p-type (holes). The presence of these carriers can induce redox reactions for the duration of the optical stimulation — the photofaradaic response (Figure 1.5, left and bottom). Finally, amid any photoresponse there is the possibility of electron–hole pairs undergoing nonradiative recombination, which produces phonons that ultimately drive the photothermal response. Defect-laden structures can display an enhanced photothermal response (Figure 1.5, top right), owing to defect-induced conical intersections within the range of the band gap that facilitate nonradiative recombination [57]. In a biological setting, the photocapacitive, photofaradaic, and photothermal responses may all be able to alter the membrane potential of cells (Figure 1.5). Because the first two processes directly relate to the manipulation of local electric fields, it is reasonable to expect that they can actuate voltage-gated channels that are responsible for regulating the overall cell membrane potential [58][59]. In the case of photothermal modulation, the change in potential is postulated to arise from the temperature-dependent electrostatic characteristics of cell membranes [60][61]. In particular, the double-layer capacitance increases with increasing temperature [61][62], while the impedivity decreases [60], such that the localized heating yields a depolarizing current, that is, an inward flux of positive ions.

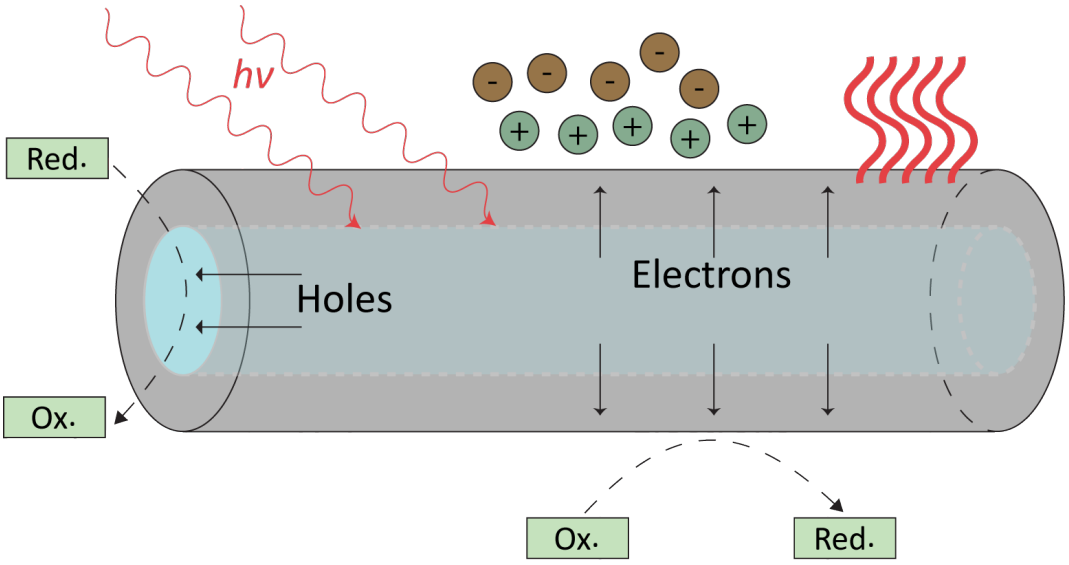

Figure 1.5: Schematic of silicon nanowire (SiNW) responses to photostimulation, using a p-i-n core-shell architecture. Upon charge separation, the electrical double layer of electrolytes at the NW surface (green and brown circles, top edge) can undergo a capacitive discharge. This large, transient spike in current is the photocapacitive current. Additionally, the enrichment of electrons and holes in region of p and n type Si exposed to solution can facilitate redox reactions, which generates a small, photofaradaic current for the duration of illumination ("Red" and "Ox" boxes, left and bottom). Finally, photothermal heating of the environment occurs in the case of nonradiative recombination (wavy red arrows, top right).

Photocapacitive and photofaradaic materials are strong candidates for applications in localized Ca^{2+} stimulation. Silicon p-i-n diode junctions and coaxial p-i-n silicon nanowires (SiNWs) have both been used to induce Ca^{2+} fluxes in response to illumination in dorsal root ganglia (DRG) [47][53]. The simplest, presumed mechanism for this Ca^{2+} response is that it is actuated directly, by a change in local membrane potential that operates voltage-gated calcium channels (Figure 1.2)[37]. That being stated, there are certainly other possible means by which electrical stimulation can have physiological effects, in calcium-dependent and independent ways [32][34][35]. These tend to be most applicable for long term exposures on the scale of tissues [34][35], which renders the putative benefits of optical stimulation with nanoscale devices irrelevant when coupled to these mechanisms. As such, we will focus our attention on Ca^{2+} stimulation and directly related processes in the context of standalone devices.

SiNWs are capable of eliciting Ca^{2+} responses through a primary photofaradaic stimulation

[53], but other related materials may also act through photocapacitive [62] and photothermal [51] mechanisms. They have a low but noticeable capacitive response, a strong faradaic response, and a low but nonzero photothermal response [62]. The photothermal response can be tuned by adjusting the porosity of the NWs by way of metal-assisted chemical etching [51]. A few recent works have used p-i-n SiNWs with the specific aim of modulating Ca^{2+} signaling in cardiomyocytes (CMs), which is, functionally, equivalent to modulating the pace of beating in those cells [63][49]. Because CMs do not readily internalize whole NWs, the approaches presented in each work differ based on their method for forming NW-CM interfaces. The first method sought to program CMs to adopt a target beating frequency through repeated training sessions, per-formed on a polymer mesh-SiNW substrate. The SU-8 mesh-based approach relies on the interfaces formed between cells and NWs embedded in the polymer substrate [49]. While the device is macroscopic, the stimulation relies only upon the photofaradaic response of the NWs, so the overall technique remains leadless. By using a scanning confocal microscope for illumination, stimulation times and locations may be precisely defined by taking into account the scan rate of the system, the size of the relevant airy disk, and the position of the stimulated NWs. The authors defined training periods subject to stimulation at the desired beating frequency as well as rest periods, and monitored the fluorescence of a Ca^{2+}-sensitive dye to find the post-stimulation beating rate. CMs cultured on the mesh substrate could be trained to beat in a target range between 500 and 1200 mHz within four training periods. Furthermore, the flexible mesh could be applied around whole ex vivo hearts, which spontaneously formed interfaces without the need for additional surgical procedures. The target beating rates were set to 1 and 2 Hz, and each rate could be achieved within 400 s of stimulation. This demonstrated the effectiveness of mesh-based photofaradaic devices for cardiac pacing in cell culture as well as entire hearts. An alternate, recently presented, method for accessing CMs with SiNWs involved taking advantage of supporting cell types that spontaneously internalize the NWs, and relying on coupling between those cells and CMs [63]. For putative therapeutic applications, this tech-

nique presents the benefit of being minimally invasive, as it requires only an injection of NW-containing cells, provided the given cells interface with the CMs. In the report, myofibroblasts (MFs) were selected as candidates because they fulfill the criterion of internalization, and because they are the subject of a debate regarding their competency for electrical coupling with CMs [64][65]. Optical stimulation of NWs in cultures of MFs produced clear Ca^{2+} responses in the cells, which appeared to then transmit the Ca^{2+} signal intracellularly. Moreover, in co-cultures of CMs and MFs, stimulation in MFs was recognized by adjacent CMs very rapidly, and much like stimulation using the mesh-based devices, CMs could be trained over the course of about 400 s to beat at a desired frequency. Interestingly, this same level of communication was not evident in whole hearts, where Ca^{2+} responses were typically limited to the specific cells being stimulated.

Within the in vitro context, Parameswaran and co-authors have used coaxial p-i-n SiNWs to elicit action potentials in cultured neurons [53]. In the system studied, gold nanoparticles were used as a catalyst in the chemical vapor deposition-based synthesis, and remain on the final product as metallic gold centers along the NW surface. These gold centers were posited to alter the surface states of the silicon, which facilitated a photofaradaic response to optical stimulation at 532 nm. Cathodic reactions dominated this response, since the shell was composed of n-type silicon, whereas the exposed surface of p-type silicon was comparatively lower. When these NWs were added to a culture of dorsal root ganglion cells, they interfaced with the cells, and the photofaradaic reaction could induce action potentials using laser power as low as 6.75 mW for 1 ms. This included single action potentials, as well as trains at up to 20 Hz. An alternate type of device can be formed from SiNWs crosslinked by Si nanobridges, which yields a material that is chemically heterogeneous and mesoporous [62]. Electrical modulation from these devices is achieved indirectly, through the photothermal effect, rather than through photo-capacitive or photofaradaic means. The induced local heating around membranes reduces impedance across the membrane and facilitates a depolarizing current. Micron-scale segments of this material have been added to DRG cultures,

where they form extracellular interfaces with the component cells. Photothermal stimulation of these interfaces yields the expected depolarization, which triggers action potentials. As such, these materials offer another method for neural modulation, which does not rely on internalizing the relevant structures, as is required with nanowires, but can also be deployed on a subcellular scale.

1.4 The Impact of Geometry on Cellular Behavior

Cell geometry is mutually informative with other aspects of physiology, in that it can act as both an input and an output to various cell behaviors. As discussed in the minimal model for cell mechanics, for instance, double knockdown of the tight junction proteins ZO-1/2 influences the shape of cell-cell junctions making them straight, rather than wavy. In the other direction, some types of muscle cells have evolved to demonstrate two remarkable morphological characteristics: they fuse to form multinucleate syncitia, and they are distinctly elongated along one axis[66]. Their common long axis thus serves as the axis along which the muscles can contract, by the cooperative action of the syncitia.

Geometric considerations are particularly important in how cells distribute traction stresses to their environments. An important model for understanding this was first described in 2011 by Banerjee, et al.[67], and experimentally validated in 2012 by Mertz, et al[68]. It is a continuum model that considers cells as homogeneous and isotropic gels that are elastic, contractile, and coupled to an elastic substrate via focal adhesions. The essential characteristics of the traction forces that are exerted in this model are that they are exerted only at the cell edge – as the homogeneous and isotropic character ensures they are balanced elsewhere in the material – and that they are uniformly directed inward and perpendicular to the cell membrane. A further prediction of this model is that the total mechanical work, i.e., the strain energy, ought to scale linearly with the area footprint of the gel. The experimental observations of Mertz in 2012, which examined traction stress distributions in keratinocytes, validated this model, demonstrating that its predictions of stress localization

and strain energy scaling held, not only for individual cells but for larger colonies as well. An interesting elaboration on this was reported in 2013[24], again by Mertz, Banerjee, and co-authors, where strong cell-cell coupling through cadherin-based adherens junctions was found to be crucial to this functioning. In calcium-depleted growth medium, keratinocytes detached from one another, and colonies whose mechanical output resembled single cells of an equivalent geometry, began displaying stresses as individual, disconnected cells.

Geometry was soon revealed to be a key factor of the good agreement between the continuum model and experimental results. Oakes, et al.[69], found that stresses were not just localized along the cell edge, but that they were restricted to areas of curvature, as well. This effect was not apparent in approximately circular colonies of keratinocytes, but any degree of symmetry breaking revealed the curvature dependence. Such non-circular morphologies could be obtained by forcing cells to adopt stadium-shaped morphologies through micropatterning. Even as changes in shape altered the distribution of stresses, however, the strain energy dependence was still essentially linear with respect to cell area. The total mechanical output, then, was found to arise primarily from the total area, while the localization of the output was related to the shape, such that highly elongated cells exerted large traction forces at their comparatively small curved ends. The original implementation of the continuum model was incompatible with this observation, as it predicted stresses to be distributed uniformly along the cell periphery, without respect to curvature. This conflict was resolved by adding an additional component, a line tension term along the periphery, analogous to an elastic band wrapped around the cell edge. With the addition of this line tension term, the predicted stress distributions were once again in excellent agreement with the observations, at least with respect to single cells. The question of whether this model could be generalized to colonies of epithelial cells formed the motivation for a substantial portion of my research. A further discussion of this, including the observation of novel force distribution patterns and the development of a new model to capture both the continuum and non-continuum behaviors, constitutes Chapter 2.

1.4.1 Enforcing Cell Geometry With Micropatterning

There are a number of methods available for enforcing geometric constraints on colonies. For certain applications, this may be as simple as forming a liquid-tight seal between the culturing substrate and a stencil in the desired shape. In many cases, however, this may interfere with measurements, or introduce undesired mechanical artifacts at the boundaries. Another approach, then, is to limit the adhesive area available to cells; since cells cannot form stable protrusions without focal adhesions to connect to the substrate, the boundaries of the cell or colony will conform to the adhesive region. Protocols for this class of technique, called micropatterning, are available for glass as well as flexible substrates, and for various means of promoting adhesion, including non-specific coatings such as poly-L-lysine and biomimetic options such as extracellular matrix proteins. The remainder of this section is devoted to detailing the method used to micropattern colonies that was employed throughout the course of the research described here. A more compact step-by-step protocol is also included in the Appendix.

This method is adapted from Tseng, et. al, 2011[70], and is ideally suited for patterning extracellular matrix onto polyacrylamide (PAA) hydrogel substrates. Because it can be used with any stiffness of gel and any matrix protein, it is broadly suited for a range of applications, including mechanical measurements such as traction force microscopy. To my knowledge, the chemical modifications that take place at each step have yet to be elucidated and reported in the literature. A partial analysis that I conducted to this end is presented here to both aid in troubleshooting and as a foundation for a potential further characterization of the method.

This method requires the following reagents: Glutaraldehyde-activated coverslips (see Appendix), a quartz-chrome photomask with the desired patterns etched in the chrome, isopropanol and hexane for cleaning, PAA hydrogel reagents, 1-Ethyl-3-(3-dimethylaminopropyl)

carbodiimide (EDC), Sulfo-N-hydroxysuccinimide (Sulfo-NHS), a stable solution of ECM protein, and a solution of buffer corresponding to the desired ECM. For the ECM buffer, 4-(2-hydroxyethyl)-1-piperazineethanesulfonic acid (HEPES) represents a good choice for fibronectin, while 2-(N-morpholino)ethanesulfonic acid (MES) or piperazine-N,N'-bis(2-ethanesulfonic acid) (PIPES) are better options for collagen, owing to the propensity of collagen to bundle at high pH, a consideration which is discussed in more detail below.

Quartz-chrome photomasks with micron or sub-micron feature sizes are commercially available. Custom-designed masks, with user-specified patterns, are most desirable to suit the relevant research questions; software for doing so includes AutoCAD and Adobe Illustrator. The most important practical considerations are the spacing between individual patterns, and the spacing between clusters of patterns. Individual patterns should be sufficiently separated so that colonies cannot protrude out to merge with one another, unless that is a desired feature. This specific distance varies based on the type of cells being used, but an interpattern distance of about twice the size of the pattern itself is usually sufficient. Following this rule, individual patterns can be varied upon and repeated to form a cluster that fills an area corresponding to the type of coverslip to be used. For instance, applications using round coverslips with 25 mm diameter are best organized to fit within the concyclic square that is circumscribed by the edge of the coverslip. This allows for all of the patterns to be used, while also allowing some margin for handling the gels with forceps without disturbing the patterns. The spacing between clusters, then, can be determined by establishing the minimum distance necessary so that two adjacent coverslips, each centered on their respective cluster, will not overlap one another.

For the first step of the process, the chrome surface of the photomask must be cleaned, first with water and then with isopropanol. After this is completed, the surface is more hydrophilic, so it must be treated with hexane to restore hydrophobicity. This can be accomplished by simply rubbing 600 μL of hexane into the surface using a Kimwipe, and is necessary to prevent the PAA hydrogel from adhering to the mask, rather than the coverslip.

Once the mask is treated, the PAA gel of desired stiffness can be prepared, and 11 μL of solution pipetted directly onto each mask position, at which point the activated coverslips are placed on top, such that the PAA solution is sandwiched between mask and coverslip. After polymerization, the patterned regions are activated by placing the photomask in a UV-ozone cleaner with 185 and 254 nm illumination for about two minutes. The specific transformation this induces on the gel surface remains unclear. The EDC and NHS crosslinking chemistry employed in subsequent steps depends on the presence of carboxylates and primary amines, and is most commonly used to link the N-termini of peptides with carboxylate targets. This leads to the supposition that the deep UV illumination somehow effects the transformation of the surface functional groups from amide to carboxylate, but there is little evidence of such amide hydrolysis being catalyzed by UV light or ozonolysis alone, without the presence of strong acids or bases. The use of UV-ozone treatments on polymer surfaces is not without precedent, however. Polyisoprene-based rubber crumb, for instance, has been oxidized with ozone to form carbonyls[71], and more saliently, poly(methyl methacrylate)[72] and polycarbonate[73] have also been observed to form peroxides and hydroxyls under UV-ozone treatment. It is possible that such oxidized species may be similarly generated on the PAA surface in the UV-ozone furnace, which then go on to participate in crosslinking chemistry as if they were carboxylates.

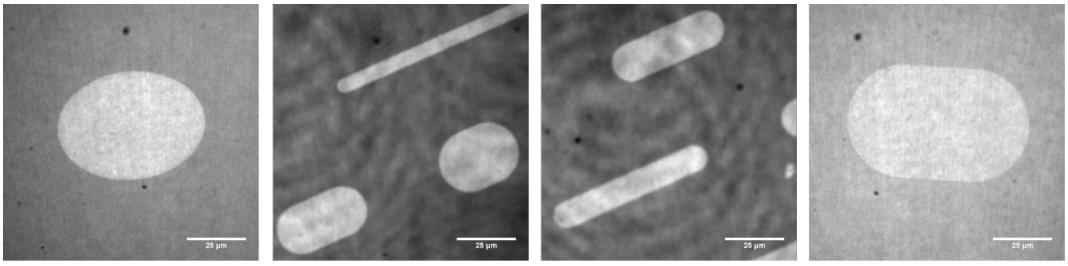

Figure 1.6: Fluorescence of fluorescein-5-semithiocarbazide, a dye that can be used to verify the success of the patterning protocol up to the crosslinking stage.

Whatever the identity of the surface functional groups after illumination, the illuminated regions – and only the illuminated regions – are responsive to EDC/NHS crosslinking

chemistry. Such methods for crosslinking are commercially available and comparatively well-characterized. In the canonical scheme, EDC reacts with carboxylates to form an unstable o-Acylisourea ester intermediate. NHS or its water-soluble analog, Sulfo-NHS, may then substitute with that ester to form a more stable NHS ester. The NHS ester itself is reactive with primary amines, and so may be displaced to yield the final product, where the moieties attached to both the original carboxylate and amine are linked by an amide bond. In the context of this patterning method, the presumptive link is between the activated surface of the gel and the N-terminus of the ECM protein. The effectiveness of the method up to this step can be verified using fluorescein-5-semithiocarbazide instead of NHS, which can be visualized using standard FITC filter settings on a fluorescence microscope. The resulting images should display excellent localization to patterned regions (Figure 1.6).

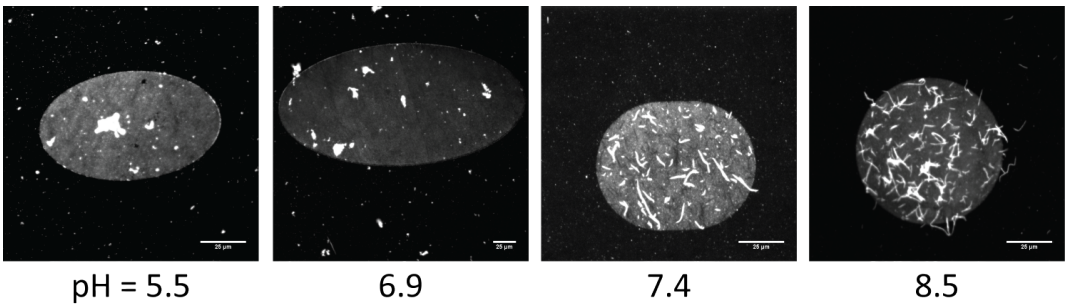

Figure 1.7: Images of AlexaFluor-560 labeled collagen on patterns. The pH of the buffer used to dilute the collagen during deposition was varied, which demonstrated the importance of acidic pH in successful patterning. While low pH did not completely eliminate collagen bundling, the incidence was drastically reduced between pH = 6.9 and pH = 7.4. The buffers used, in order of lowest pH to highest, were MES, PIPES, DPBS, and HEPES.

To prepare the patterned surface for cell adhesion, the desired ECM is added to the EDC/NHS treated gels. The concentration of ECM to use is best left to empirical determination, but the amounts tend to be comparatively high, between 100-500 μg/mL, and frequently on the higher end of that range. Additionally, the pH of the buffer solution during ECM attachment can have a significant impact on the final results. This is most notably evident when working with collagen, as at basic pH, collagen fibrils tend to aggregate and

form bundles, which then do not react with the NHS esters and yield a surface that is not adhesive. This is demonstrated in Figure 1.7, where collagen incubation using different buffers showed the best results with the lowest pH.

CHAPTER 2

CELL MOTILITY CONTRIBUTES TO EPITHELIAL TRACTION STRESS DISTRIBUTION

2.1 Preface

This chapter is adapted from Schaumann et. al, 2018[74]. The experiments described in this chapter were designed and performed by the author. The continuum model described herein was developed by Shiladitya Banerjee[69]. The active vertex model (AVM) was developed by Michael F. Staddon and Shiladitya Banerjee, and all AVM simulations were performed and analyzed by Michael F. Staddon. Margaret L. Gardel and Shiladitya Banerjee provided invaluable guidance and input at all stages of this project.

2.2 Introduction

Mechanical interactions at cell–cell interfaces and between cells and the extracellular matrix (ECM) play pivotal roles in tissue organization [75], developmental morphogenesis [76], wound repair [77], and cancer invasion [78]. These collective cell behaviors rely on long-range transmission of mechanical forces, tightly coordinated by mechanical cell–cell coupling and biochemical signaling [79]. The maintenance of the balance between cell–cell and cell–ECM mechanical forces is essential for tissue cohesiveness and for cooperative cell movement in swirls, packs, and clusters during many developmental processes. However, little is known about the relative roles of cell motility and intercellular mechanical coupling in coordinating mechanical stress transmission and relaxation across tissue scales.

Forces generated by molecular motors are transmitted by the actin cytoskeleton and to neighboring cells via cadherin-based adhesions or to the ECM via integrin-based focal adhesions. The predominant mechanism of cell force generation occurs via the activity of myosin II on actin filaments, collectively known as the actomyosin cytoskeleton, to generate

contractile forces. The actomyosin cytoskeleton, in turn, applies active contractile forces at the sites of integrin-based cell–ECM adhesions. Several studies have implicated that the mechanical cross-talk between actomyosin contractility and cell–cell and cell–ECM adhesions [80][81][82] can regulate cell traction forces, cell shape changes, and cellular motile behavior. We and others have shown how epithelial colonies with strong cell–cell coupling can propagate traction stresses across multicellular length scales [24][68][83]. In the absence of strong intercellular adhesions, cell traction stresses are primarily localized to cell–cell interfaces [24]. While cadherin-based cell–cell forces have been shown to modify traction stress organization and contractility of static epithelial monolayers, we lack a quantitative predictive model for how intercellular tension is propagated to the ECM in highly motile cell colonies with diverse geometries. Progress is limited by the lack of a robust model system that allows precise determination of mechanical forces under controlled environmental conditions, which can be used to build quantitatively accurate cross-scale physical models. Here we address this challenge using an in vitro experimental system together with a computational model that enables multiscale analysis of epithelial mechanics with precise control over cell density, cellular adhesive and motile properties, ECM mechanics, and geometry.

Using a combination of traction force microscopy (TFM) [45] and micropatterning on Madin–Darby canine kidney (MDCK) cell colonies, we show that cellular traction forces can vary widely in magnitude and spatial organization for the same geometry and composition of the colony. For MDCK colonies with peripheral localization of traction stresses, we recapitulate results previously reported for single adherent cells [69] and strongly adherent cell colonies [68]. In this case, the colony behaves like a macroscopic contractile medium, and its overall mechanical output can be accurately described using a previously developed continuum model [67]. However, this model is inadequate to describe traction stress organization in colonies with highly motile cells, where cell traction forces are distributed throughout the colony interior. To this end, we develop an active vertex model for motile epithelial cell colonies adherent to a soft elastic substrate. In contrast to purely mechanical vertex models

[84], our approach accounts for the changes in cell shape and adhesion that occur during cell motion. In quantitative agreement with experiments, our cell-based model predicts a relationship between individual cell motility and traction stress localization in large colonies. Furthermore, our model successfully predicts how colony traction patterns can be modulated by internal cell events such as division, polarized motility, and collective rotations. Thus, we propose a robust quantitative framework for multiscale analysis that allows us to predict the regulation of mechanical stress transmission from the single-cell to tissue level.

2.3 Materials and Methods

2.3.1 Cell Culture

MDCK cells were cultured in high-glucose DMEM and supplemented with 10% fetal bovine serum (Mediatech; Corning, Corning, NY), 2 mM l-glutamine (Corning), and penicillin-streptomycin (Corning). To visualize cell shapes, wild-type MDCK cells were transfected with plasmid DNA constructs encoding for Stargazin green fluorescent protein (Stargazin-GFP) (courtesy of M. Glotzer, University of Chicago, Chicago, IL). These cells were sorted and found to stably express Stargazin-GFP, with no noticeable loss in marker expression after >20 passages. ZO-1/2 KD MDCK (dKD) cells were provided courtesy of M. Peifer, University of North Carolina, Chapel Hill, NC.

2.3.2 Traction Force Substrates

PAA substrates were prepared as previously described[69]. Gels with a Young's modulus of 8.4 kPa were prepared by first making a mixture of 3.125 ml 40% acrylamide (Bio-Rad Laboratories, Hercules, CA), 0.833 ml 2% bis-acrylamide (Bio-Rad), and 1.042 ml water. To this were added 5 μl 110-nm sulfate-modified fluorescent microspheres (Invitrogen, Carlsbad, CA).

2.3.3 Collagen micropatterning

Micropatterned substrates were prepared using the same ultraviolet illumination-mediated procedure described[69]. Briefly, a chrome-plated quartz photomask (Applied Image, Rochester, NY) was cleaned with water and wiped with 0.3 ml hexane (Sigma-Aldrich, St. Louis, MO) to induce hydrophobicity on the photomask surface. Polyacrylamide gel mixtures were polymerized for 40 min between the photomask and prepared glass coverslips with 2.5 µl ammonium persulfate and 0.75 µl tetramethylethylenediamine as radical initiator and coinitiator, respectively. Once the gel was polymerized, the photomask was placed in a UVO-Cleaner 342 (Jelight, Irvine, CA) and illuminated with a combination of 185- and 254-nm ultraviolet light for 90 s. The coverslip and gel were then removed from the photomask by submerging the entire complex in water and gently detaching a corner with a razor blade. Gels were incubated for 10–15 min in a solution containing 5 mg/ml 1-ethyl-3-(3-dimethylaminopropyl)carbodiimide hydrochloride (EDC) (Thermo Fisher Scientific, Hampton, NH) and 10 mg/ml N-hydroxysuccinimide (NHS) (Thermo Fisher Scientific) kept at acidic pH with 2-(4-morpholino)-ethane sulfonic acid (MES) buffer. The EDC–NHS solution was aspirated and replaced with a solution containing 0.5 mg/ml collagen-I in an MES buffer for 40 min. Through this procedure, collagen cross-links only to regions exposed to UV light as defined by the photomask. Gels were washed three times for 5 min in phosphate-buffered saline solution before cells were plated.

2.3.4 Microscopy and live cell imaging

Cells were imaged on an inverted microscope (Ti-E; Nikon, Melville, NY) with a confocal scanhead (CSU-X; Yokogawa Electric, Musashino, Tokyo, Japan); laser merge module containing 491, 561, and 642 laser lines (Spectral Applied Research, Richmond Hill, Ontario, Canada); and an Andor Zyla scientific complementary metal-oxidesemiconductor camera (Belfast, Northern Ireland, UK). METAMORPH acquisition software (Molecular Devices, Eugene, OR) was used to control the microscope hardware. Images were acquired using

a 40× 1 NA Plan Apo oil-immersion objective. Samples were mounted on a live imaging chamber (Chamlide, Seoul, Korea) and maintained at 37°C. For live cell imaging, DMEM was supplemented with 10 mM 4-(2-hydroxyethyl)-1-piperazineethanesulfonic acid.

2.3.5 Traction force microscopy

We measured the mechanical outputs of colonies using TFM, a technique for obtaining the stress field exerted by adherent cells on their environment [45]. In a TFM experiment, cells adhere to a thick, flexible substrate with embedded fiducial markers. For our experiments, we used PAA gels for their ease of preparation and versatility in stiffness, prepared with 0.11 µm fluorescent microspheres as markers. While cells are attached, they contract inward and deform the gel. By imaging the beads underneath cells while they are attached and subsequent to removal via SDS, we can obtain the displacement of the gel due to cell traction stresses. On the basis of the substrate displacement, we use Fourier transform traction cytometry [44][45] to ascertain both the magnitude and location of traction stresses, as well as derive bulk quantities such as the total mechanical output of a colony. TFM thus provides an effective means for measuring the mechanical characteristics of colonies and tissues, which makes it an attractive technique for experimentally testing predictions made by mechanical models of cells and colonies. As TFM is compatible with other imaging techniques, it also allows us to directly compare morphological changes and mechanical outputs.

2.3.6 Annular analysis for TFM

To obtain strain energy as a function of distance from the colony periphery, we adopted an approach similar to that used in Mertz et al. (2013). Starting from a mask of the colony outline, we eroded each outline by a distance x defined in pixels; for our purposes, we used an erosion factor of 15, which corresponded to 2.42 μm. We generated a new mask consisting of the eroded region and used this as the area over which we computed the strain energy, which is given by $W = \frac{1}{2} \int dA \, \mathbf{T}(\mathbf{r}) \cdot \mathbf{u_S}(\mathbf{r})$, where $\mathbf{T}(\mathbf{r})$ is the traction stress at point $\mathbf{r}$ and

$\mathbf{u_s}(\mathbf{r})$ is the substrate surface displacement at the same point. Because the TFM routine has a finite resolution and our settings generate traction footprints with radii of 5 μm or more, we commonly observe stresses exterior to the colony. We therefore included negative Δ, obtained by dilating the original outline mask, to incorporate these stresses. As Δ increases, the regions being analyzed have progressively smaller areas, so we divided strain energies by the area of each corresponding region to find the strain energy density, which decreases solely due to peripheral localization of stresses. As previously mentioned, this normalization to area meant that the strain energy density of regions close to the colony center can diverge, so we ignored any region with an area below μm^2. Finally, to facilitate comparison between different colonies, we normalized all values to $\Delta = 0$, such that a colony with good localization to the colony periphery should have values near 1 at the edge, and 0 elsewhere. We diverge from this process when computing the decay constant for strain energy with respect to Δ, because this quantity tends to increase in colonies with the least peripheral localization, making them unamenable to exponential fitting. We therefore used the strain energy with no normalization to area to extract these values. The strain energy profiles generated this way uniformly decrease with Δ, ensuring that they follow an exponential form. We found that the contribution from the inherent decay in stresses can still be compared with other colonies.

2.3.7 Continuum mechanical model for epithelial colonies

The continuum mechanical model used here is based on our earlier work on stationary adherent cells and cohesive cell clusters [67][68][69]. The model describes adherent cell clusters as a homogeneous and isotropic elastic medium, ignoring all fine-grained details regarding of individual cell mechanics and subcellular cytoskeletal architectures. The mechanical energy of the cell colony is given by $E = \frac{h}{2}\int dA\ \sigma_{ij}u_{ij} + \frac{Y}{2}\int dA\ \mathbf{u}^2$. The first term in the equation characterizes the energy arising from the elastic stress tensor of the cell, which is decomposed as the sum of two parts: $\sigma_{ij} = \sigma_a\delta_{ij} + \sigma_{ij}^{el}$, an active contractile stress and an elastic stress,

respectively. In this model, σ_a represents the bulk contractility acting per unit area of the cell and σ^{el} represents the elastic contribution of colony stress tensor, whose constitutive relation is governed by

$$\sigma_{ij}^{el} = \frac{Y_{cell}}{2\,(1+\nu)}\left(\frac{2\nu}{1-2\nu}u_{kk}\delta_{ij} + 2u_{ij}\right)$$

In this equation, Y_{cell} is the colony Young's modulus and ν is the Poisson ratio. The second term in the energy describes the energetic cost due to adhesions with the elastic substrate, where Y is an effective substrate rigidity related to the substrate stiffness and focal adhesion strength, given by $Y = \frac{1}{Y_a^{-1}+Y_s^{-1}}$ for adhesion stiffness Y_a and substrate stiffness Y_s. This model successfully characterized the traction stress magnitude and localization in approximately circular colonies of keratinocytes and of circular single cells[68][24][69]. In the case of noncircular geometries, traction stresses are observed to localize further to regions of curvature. The model, on the other hand, smeared stresses all along the colony periphery[69], necessitating the addition of a uniform contractile line tension, proportional to the colony perimeter, $f_m P$. This yields the energy functional: $E = \frac{h}{2}\int dA\ \sigma_{ij}u_{ij} + \frac{Y}{2}dA\ \mathbf{u}^2 + f_m P^2$, which includes the three tunable parameters of Y_{cell}, σ_a and f_m, with inputs of colony shape (with area A and perimeter P), colony height h, Poisson ratio ν, and substrate rigidity Y. The resultant colony shape in steady state is determined by minimizing the total mechanical energy of the adherent colony. The traction stresses $\mathbf{T}$ can then be obtained by $\mathbf{T} = Y\mathbf{u}$, where Y is the effective substrate rigidity defined above and u is the cell displacement field. The values for Y_{cell}, σ_a, and f_m were obtained by sweeping a range of values around the values that were previously reported for single cells [69]. The resulting traction stresses were compared with experimental results on the basis of strain energy, maximum traction stress, and the spatial extent of traction stress localization to curved regions for each geometry. The reported values were the closest to the experimental results in all three categories.

2.3.8 *Active adherent vertex model for dynamic epithelial colonies*

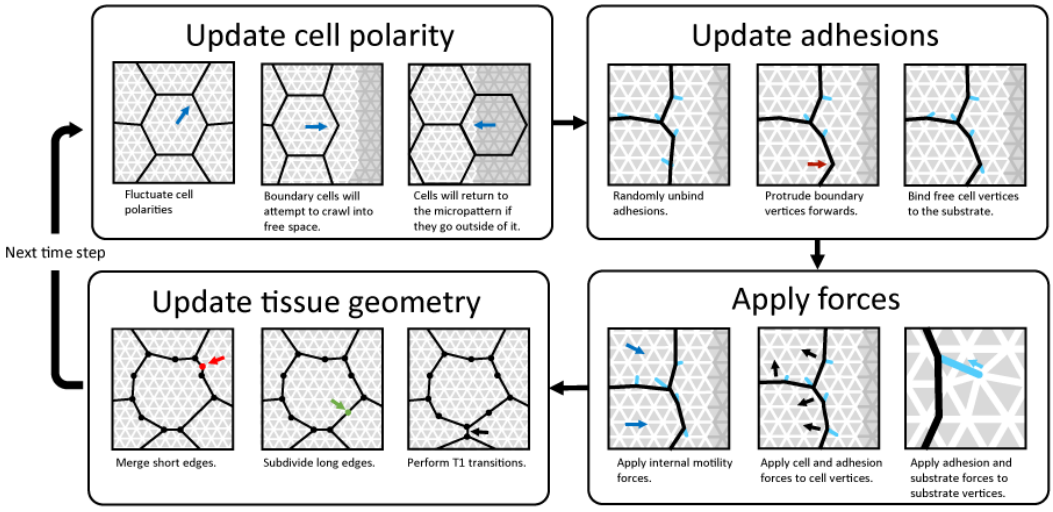

Figure 2.1: Schematic illustrating the computational pipeline in AAVM.

We model the cell colony as a two-dimensional monolayer. Each cell is represented by a two-dimensional polygon with mechanical energy given by $E = K\left(A_i - A_0\right)^2 + \Gamma P_i^2 + \gamma P_i$ [84], where A_i is the cell area, A_0 is the preferred cell area, and P_i the cell perimeter. The first term represents the monolayer volume incompressibility and resistance to changes in height, resulting in an area elasticity; the second term represents active contractility in the actomyosin cortex; the third term represents interfacial energy due to cell–cell adhesion and cortical tension. The mechanical energy a cell can be rearranged as $E_i = K\left(A_i - A_0\right)^2 + \Gamma\left(P_i - P_0\right)^2$[85], where $P_0 = -\frac{\gamma}{2\Gamma}$ is the preferred perimeter of the cells. This gives rise to a dimensionless preferred shape index, $p_0 = P_o/\sqrt{A_0}$, that describes the shape anisotropy of the cell. The lowest possible shape index is that of a circle, $P/\sqrt{A} = 3.54$. At lower values of the shape index the cells are under stress, and energy is minimized by a tissue composed of isotropic, hexagonal cells. For a cell rearrangement to occur, cells must be deformed and energy temporarily increased, resulting in an energy barrier to rearrangements. As the preferred shape index increases, the energy barrier lowers until a critical shape index, $p_0^* \approx 3.81$, where cells can rearrange with no energy cost [85]. Thus, for low preferred shape index, $p_0 < 3.81$ [85], cortical tension dominates, the cells are hexag-

onal, and the tissue acts like a solid. At high preferred shape index, $p_0 > 3.81$, cell–cell adhesion dominates, and the tissue acts like a fluid with cells able to rearrange without energy cost. The substrate is modeled as a dynamic triangular mesh of linear springs,

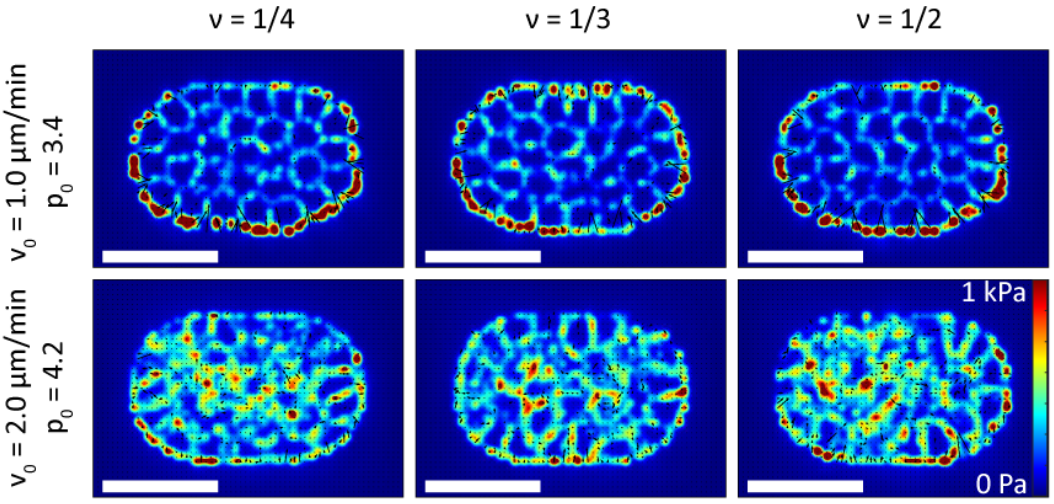

Figure 2.2: : Time averaged traction stress maps for static and motile cell colonies on substrates with varying Poisson's ratio. Using equations of linear elasticity and a square substrate grid, arbitrary Poisson's ratio may be used. Regardless of the Poisson's ratio, traction stresses localize around the colony periphery for low motility (top) and internalize at high motility (bottom). Scale bar represents 50 μm.

with total strain energy $E_{sub} = \sum_j \frac{1}{2} k_s \left(l_j - l_j^0\right)^2$, where k_s is the substrate spring stiffness, l_j is the length of the mesh edges, and l_j^0 is the rest length. Choice of the triangular mesh fixes the Poisson's ratio of the substrate to 1/3, which can be varied by implementing different topologies for the spring mesh (Figure 2.2). Focal adhesion complexes are modeled as stiff springs connecting cell vertices to substrate nodes. The total adhesion energy, summed over all cell–substrate adhesions, joining cell vertex x^α to substrate node y^β, is given by $E_{adh} = \sum_{<\alpha,\beta>} \frac{1}{2} k_f \left(\left|x^\alpha - y^\beta\right| - \left|x_0^\alpha - y_0^\beta\right|\right)^2$, where k_f is the adhesion stiffness, and $\left|x_0^\alpha - y_0^\beta\right|$ is the initial length of the adhesion spring upon binding. The cell–substrate adhesions bind and unbind stochastically. During a binding event, the adhesion springs connect the cell vertices to the nearest node of the substrate mesh, and the rest length of the adhesion bond is set to its initial length on binding. We mimic the effects of the micropattern by disabling binding outside a chosen region of the substrate representing the micropattern

geometry. Cells in the bulk move by self-propulsion with speed v_0 along their polarity vector. Cells on the boundary of the colony are able to protrude their external edges, such that cell vertices are pushed forward with a force f^{α}_{prot} before binding to the substrate. In addition, external edges have an increased line tension, γ_{ext}, to describe the preference for cell–cell adhesion over free edges. The equation of motion for each cell vertex α is given by

$$\mu \frac{dx^{\alpha}}{dt} = -\frac{\partial E_{tot}}{\partial x^{\alpha}} - \frac{\partial E_{adh}}{\partial x^{\alpha}} + f^{\alpha}_{prot} + \mu \frac{1}{n_{\alpha}} \sum_{\alpha \in i} v_0 \hat{\mathbf{p}}_i$$

where μ is the viscous drag coefficient, $E_{tot} = \sum_{i=1}^{n} E_i$ is the total mechanical energy of the cells, $\mu \frac{1}{n_{\alpha}} \sum_{\alpha \in i} v_0 \hat{\mathbf{p}}_i$ is the average self-propulsion velocity from the neighbors of vertex α, and $\hat{\mathbf{p}}_i$ is the polarity vector of cell i which fluctuates over time. The polarity vector for cells protruding out of the micropattern is reversed at a rate τ_b^{-1}. The above equation implies that friction forces balance the mechanical, active, and adhesive forces. The equation of motion for each substrate node β is given by

$$\mu \frac{d\mathbf{y}^{\beta}}{dt} = -\frac{\partial E_{sub}}{\partial \mathbf{y}^{\beta}} - \frac{\partial E_{adh}}{\partial \mathbf{y}^{\beta}}$$

By virtue of force balance, cellular forces, including friction, and mechanical and active forces (due to protrusions or internal motility) are transferred to the substrate via adhesion springs that deform owing to cell movements. From displacements in the substrate we can calculate traction forces. At each time step, we apply the equation of motion to evolve the cell and substrate vertices and update adhesions. We allow cell–cell neighbor exchanges to occur once intercellular junctions shrink beyond a critical length, which would reduce the total mechanical energy of the system.

2.4 Results

2.4.1 Colonies with same geometry vary widely in the spatial organization of traction stresses

We used MDCK cells as a model system for tissue mechanics. Seeding MDCK cells on collagen-coated TFM substrates yields isolated colonies of 10–100 cells. While colonies tend to be circular, they can achieve a variety of shapes due to spontaneous motions and stresses within the colony. Previously, we recognized the roles of geometry in controlling traction stresses in isolated cells [69]. To control colony shape, we employed identical micropatterning techniques for collagen deposition on TFM substrates. As MDCK cells do not adhere to polyacrylamide (PAA) gels, this constrained cell attachment only to areas defined by the collagen micropatterns. Surveying a large number of model colonies, we observed that colonies tended to distribute traction stresses in one of two ways. In some cases, traction stress peaks that are confined to the colony periphery and are oriented inward and perpendicular to the colony edge (Figure 2.3A, left and middle). The second mode of distribution has significant stress peaks in the colony interiors as well as on the periphery (Figure 2.3B, left and middle). Traction vectors associated with this pattern also display a greater variation in their orientation relative to the colony border (Figure 2.3B, middle). In both cases the vector sum of all forces throughout the colony is small, less than 10% of the total strain energy, indicating that the traction forces are balanced across the cell island. To quantify the extent of peripheral localization of stresses, we employed the same procedure used in Mertz et al. (2012) to plot strain energy density as a function of distance from the colony edge. We divided each colony into a series of concentric contours with width x, which followed the shape of the colony outline such that the ring associated with distance Δ covers every point with a distance between Δ and $\Delta + x$. Because the TFM analysis yields traction footprints with widths on the order of several microns, we included negative Δ values to capture stresses that are exerted outside of the border. We calculated the strain energy of each region by

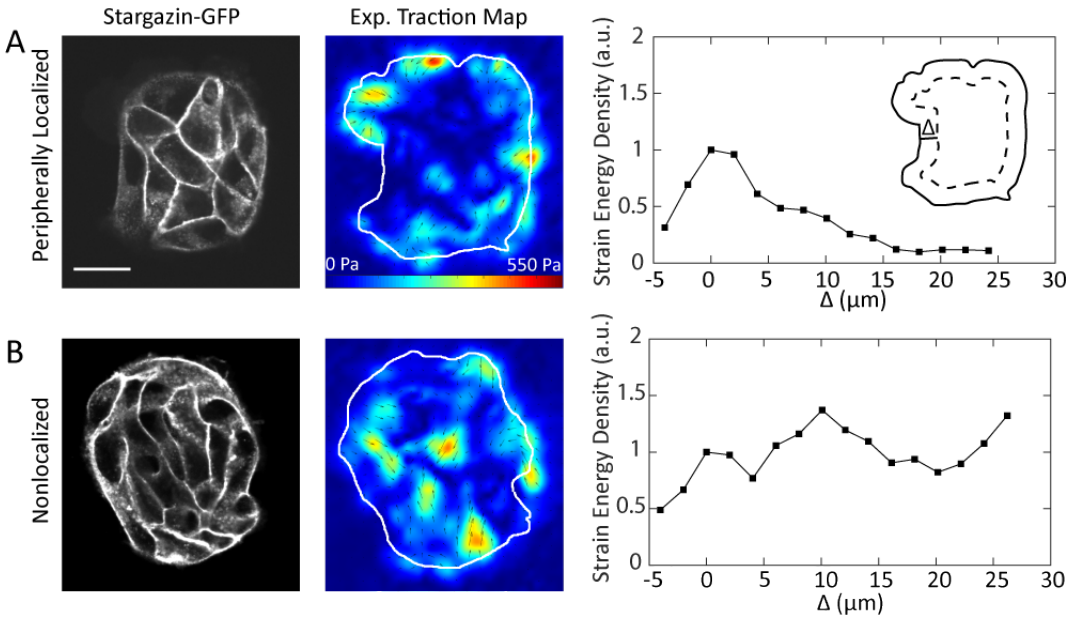

Figure 2.3: (A) A colony with traction stresses localized at the colony periphery. Left, the shapes of cells and the overall pattern shape visualized with the membrane marker Stargazin-GFP, scale bar = 25 μm. Middle, traction stress heatmap for the colony at left — the colony shape is outlined in white. Right, strain energy density as a function of Δ, the distance from the colony border, normalized to the value at $\Delta = 0$. The peak at or near $\Delta = 0$ is the defining feature of colonies with peripheral stress localization. Right, inset, schematic of the procedure used to generate strain energy density profiles. (B) A colony with a higher proportion of internal traction stresses. Left–right: cell and colony shapes visualized with Stargazin-GFP, traction heatmap showing stresses localized to hot spots distributed throughout the colony interior, strain energy density profile that increases with Δ.

taking the dot product of the traction force with the displacement, and obtained the strain energy density by dividing this quantity by the area of the region. To better compare results from several colonies, we normalized each strain energy density to its value at $\Delta = 0$. The resulting plots provide a quantitative profile of traction stress localization relative to the colony edge. Peripherally localized colonies have a maximum value at or near $\Delta = 0$, with the strain energy density rapidly decaying further into the interior (Figure 2.3A, right). For colonies with sizable tractions throughout the interior, strain energy density at $\Delta = 0$ is not necessarily the maximum, and the profile does not decay near the center of the colony (Figure 2.3B, right).

2.4.2 Mechanical output of colonies with peripheral localization of traction stresses are identical to single cells

MDCK colonies with peripherally localized traction stresses bore striking resemblance with previously reported traction stress patterns for adherent single cells [69] and strongly cohesive keratinocyte colonies [68] that are well described by a continuum model[67][86]. Briefly, the continuum model describes the cell colony as an isotropic and homogeneous elastic medium, subject to a uniform contractile stress (force per unit area) due to actomyosin contractility (Materials and Methods). The contractile medium is coupled to a soft elastic substrate via stiff springs that represent adhesion bonds (Figure 2.4A). This isotropic homogeneous model was sufficient to capture traction stress localization in circularly shaped cells and colonies, where traction stresses spread out evenly along the periphery[68][69]. When individual cells are constrained to noncircular adhesive geometries, traction stresses are constrained to regions of high curvature, and an edge contractility parameter was needed for the model to capture the experimental results [69]. The extent to which similar traction stress localization would also occur in noncircular model epithelial colonies remained unknown.

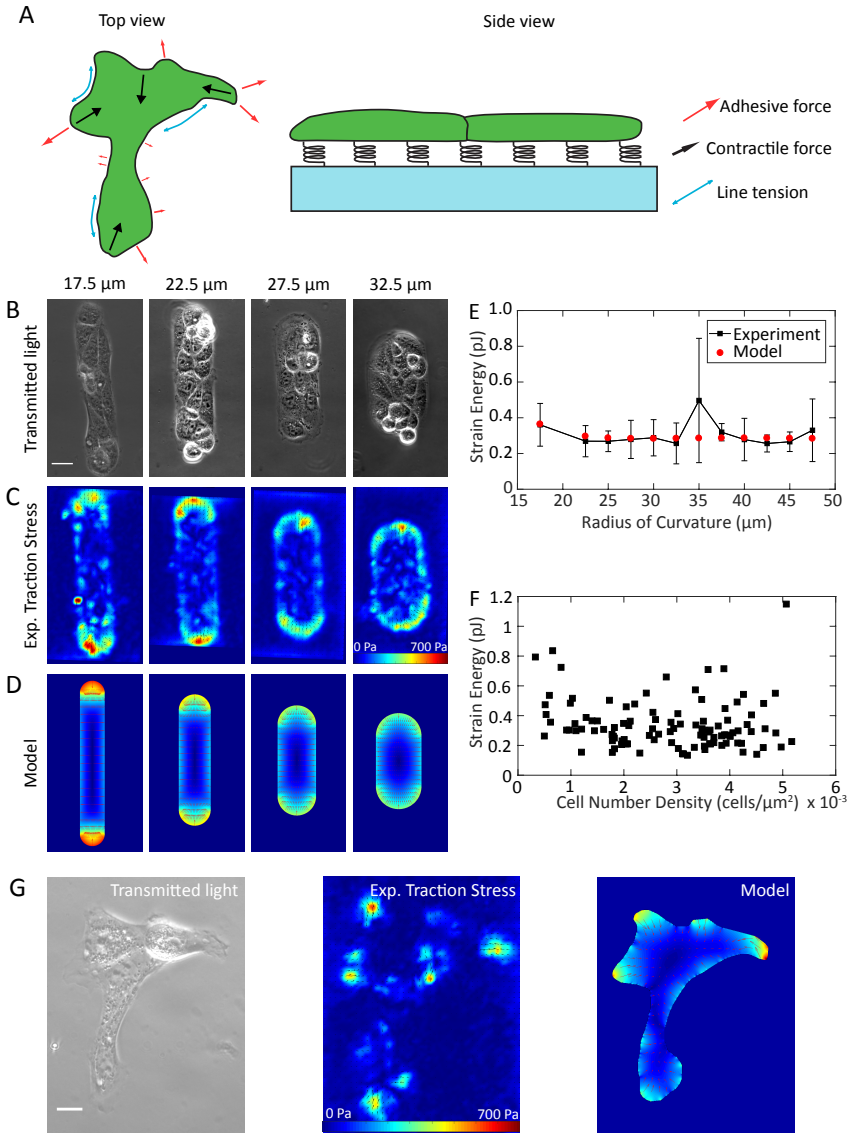

Figure 2.4: For colonies with peripheral localization of traction stress, a continuum mechanical model quantitatively captures traction stress distribution. (A) Schematic of the continuum mechanical model. (B–D) Peripheral localization of traction stresses in ZO-1/2 dKD MDCK colonies is quantitatively captured by a homogeneous continuum model for cohesive cell colonies. (B) Phase contrast images of ZO-1/2 dKD MDCK cells in stadium-shaped micropatterns of constant area and varying radii of curvature. (C) Traction stress heatmaps for constant area colonies, averaged over n = 4–9 different colonies. (D) Continuum model results for given colony geometries with model parameters: $E = 6.8$ kPa, $\sigma_a = 780$ Pa, and $f_m = 0.3$ nN/μm. (E) Colony strain energy is independent of colony shape. Each data point represents the average over n = 4–9 colonies. (F) Strain energy does not depend on the number density of cells within a colony. (G) Traction stress organization in unconstrained MDCK colonies can also be described by the continuum model. Left to right, phase contrast, experimental traction map, and continuum model traction map images for an adherent colony on an unpatterned substrate. Model parameters are the same as in D. All scale bars = 25 μm.

To test whether predictions of this continuum mechanical model (Materials and Methods) were consistent with cell colonies of arbitrary geometries, we used micropatterning to create 8000 μm^2 stadium-shaped patterns, with radii of curvature of the ends that span from 17.5 to 47.5 μm. For these experiments, we used zonula occludens-1/2 double knockdown (ZO-1/2 dKD) MDCK cells [29][30], which display stronger peripheral localization than their wild-type counterparts. For each adhesion geometry, we acquired phase-contrast images of the cells (Figure 2.4B) and measure traction stresses transmitted to the substrate. For each geometry, we measured the traction stresses of multiple colonies and calculated the time-averaged stress field (Figure 2.4C). This revealed that traction stresses are localized to regions of curvature for the model colonies, with the traction vectors oriented inward and perpendicular to the colony edge, similarly to what we observed for single cells [69]. Using the continuum model, we parametrized the elastic modulus for the colony (6.8 kPa), the colony edge line tension (0.3 $nN/\mu m$), and active contractile stress (780 Pa) required to recapitulate the traction stress distribution (Figure 2.4D) and strain energy (Figure 2.4E) of colonies with varied geometry. Consistent with our previous findings for single cells, we found that the total mechanical work (strain energy) of the colony is independent of the colony geometry for a constant area (Figure 2.4E). Further, we established that the mechanical work is independent of the cell number density (Figure 2.4F). This indicates that the tissue-scale mechanical properties that can be described with the continuum model are determined by the global tissue shape and mechanical properties and are independent of cell-scale properties such as their shapes and density.

To demonstrate the applicability of this continuum model to epithelial colonies of arbitrary geometries, we tested its utility in predicting force localization of an unconstrained colony. In Figure 2G, phase contrast (left) and traction force (middle) measurement of a small colony containing four MDCK cells are shown, chosen for its highly extended shape. Traction stresses are localized at the periphery, and are further concentrated in small, high-curvature regions. Using the parameter values benchmarked from the micropattern and

TFM experiments, the continuum mechanical model successfully predicts the spatial localization and magnitude of the traction stresses for this colony shape (Figure 2.4G, right). Thus, colonies with peripheral localization of traction stresses with varying geometries are well characterized by a continuum model that has a bulk contractility and an edge tension, similarly to what we observed previously for single cells [69]. Taken together, these results suggest a regime in which adherent cell colonies exhibit identical mechanical behavior as single cells, such that its global mechanical output is independent of individual cell properties.

2.4.3 Active adherent vertex model for traction stress prediction in dynamic epithelial colonies

Our experimental data suggest another regime for mechanical force transmission in colonies, where traction stresses are distributed throughout the colony interior (Figure 2.3B). One underlying mechanism of interior stresses arises from reduced cell–cell coupling [24]. However, we sought to explore the extent to which cell motion within a confluent tissue could underlie interior traction localization. To predict traction stress localization in dynamic colonies, we developed the active adherent vertex model (AAVM) for predicting mechanical stresses in adherent cell colonies. This approach allows explicit control over the dynamic mechanical properties of individual cells, which are not accessible by a continuum description of colony mechanics. In contrast to purely mechanical cell-resolution vertex models [84][85][87][88][89] or cellular potts models [90][91], AAVM explicitly accounts for the coupling between mechanical forces that drive cell motion and the kinetics of cell–matrix adhesion binding/unbinding, active cell motility from cell protrusions, retractions, and cell polarity fluctuations (Figure 2.5A and Figure 2.1). We model the cell colony as a confluent two-dimensional monolayer, where the geometry of each cell is described by a polygon (Figure 2.5A; Materials and Methods). To allow the formation of curved cell shapes, we subdivide the cell contour into several linear segments. Physical interactions between cells are modeled following the vertex model for epithelial tissues, whose mechanical energy arises from cellular elasticity, cortical tension,

cell–cell adhesion, and actomyosin contractility [84].

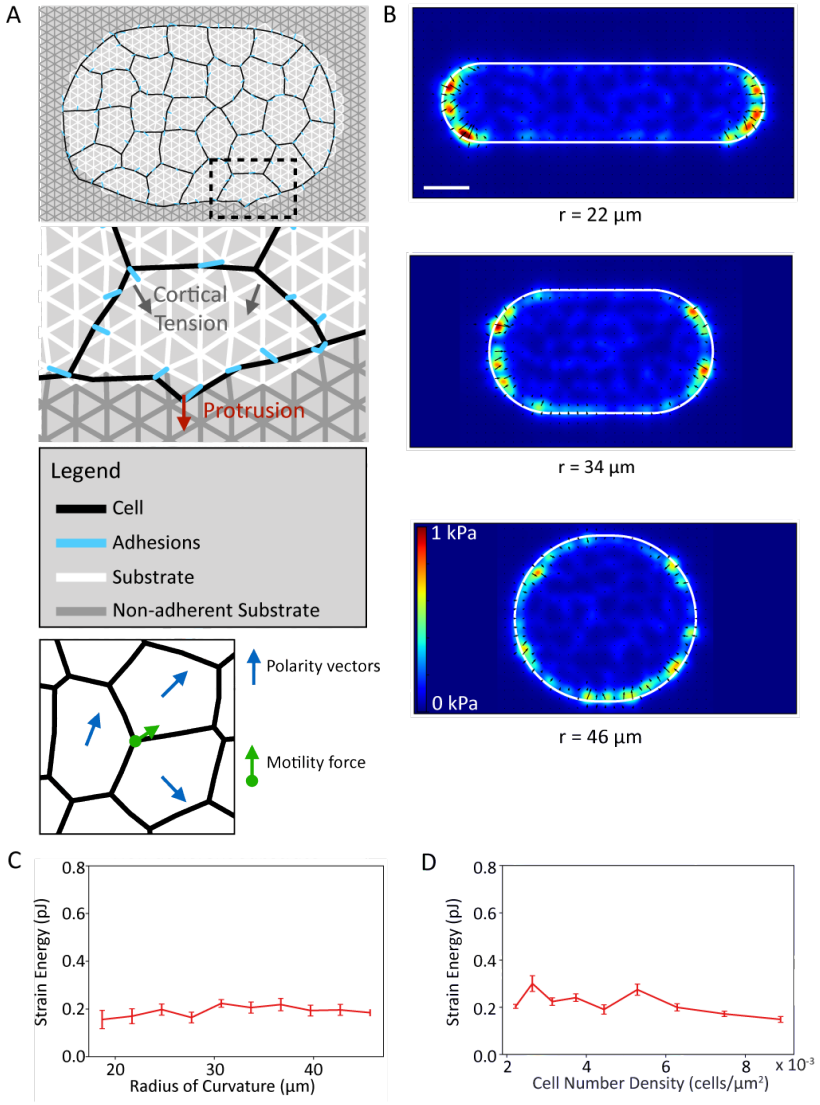

Figure 2.5: Active adherent vertex model for epithelial cell colonies can be benchmarked to experiments to capture spatial variations in traction stress. (A) Simulation image for a cell colony on a micropattern (top) and a zoomed-in region illustrating the mechanical forces acting on adherent cells (bottom). (B) Time-averaged traction stress maps for varying curvature radii of the micropattern: r = 22 μm (top), r = 34 μm (middle), and r = 46 μm (bottom). (C) Strain energy as a function of radius of curvature for a fixed area of the pattern. (D) Strain energy as a function of cell density for fixed pattern shape.

The soft elastic substrate is modeled by a triangular mesh of harmonic springs, which are anchored to cell vertices via stiff springs (Figure 2.5A), representing focal adhesion complexes. The cell–substrate adhesions bind and unbind stochastically at fixed rate constants.

We model the confining effect of the micropattern by disallowing adhesions outside a predefined geometry of the substrate. Cells in the interior of the colony move with a speed v0 in the direction of its polarity (Materials and Methods). Cells on the boundary of the colony assemble protrusions at their external edges, which push the cell vertices forward that subsequently bind and pull on the substrate. Each cell vertex evolves in time following an overdamped equation of motion, where the cell vertex velocity is proportional to forces resulting from total mechanical energy of the colony, cell–substrate adhesions and active cellular motility (Materials and Methods).

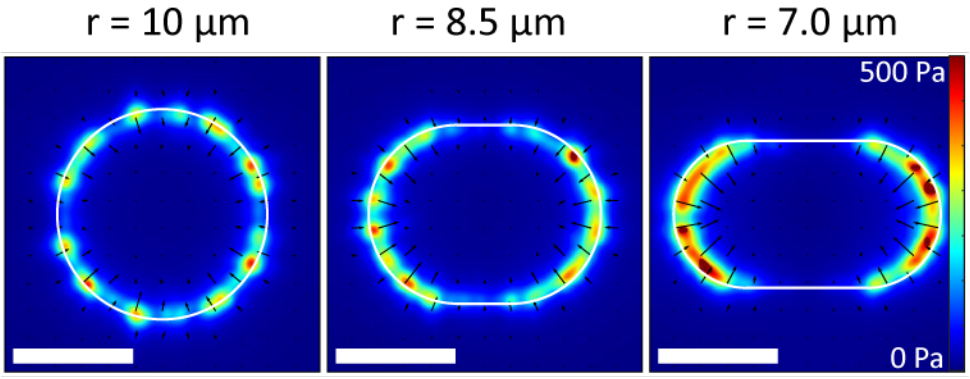

Figure 2.6: Time averaged traction stress maps for single cells in micropatterns with varying curvature. Traction stresses are localized around the curved borders, and increase in magnitude as the curvature increases. Scale bar represents 10 μm.

By benchmarking the physical parameters of AAVM we successfully captured the experimental behavior for cohesive cell colonies in Figure 2.5, as well as single cells (Figure 2.6). To this end, we set the internal motility speed, v0, of the cells to be comparable to the low motility speed for ZO-1/2 dKD MDCK cells. In quantitative agreement with TFM experiments and the continuum model, we find that traction stresses localize around the curved periphery of the cell colony. Furthermore, as the radius of curvature decreases, the local traction stresses increase in magnitude as they are concentrated in a smaller region (Figure 2.5B). By measuring the strain energy density as a function of distance from the colony edge, we find that most strain energy is applied around the periphery of the micropattern, which decays with distance from the edge of the colony (Figure 2.5C and Figure 2.7). While the

magnitude of local traction stresses changes with curvature, the model captures the experimental result that the total strain energy is independent of pattern curvature (Figure 2.5C). With this same set of parameters, our model accurately predicts the linear dependence of the total strain energy on the colony area (Figure 2.8), as observed for single cells and cohesive colonies [68][69]. By altering the preferred cell area for a fixed area of the micropattern, we can control the number density of cells in a given colony. As a result, we found that the colony strain energy is independent of cell number density (Figure 2.5D), in quantitative agreement with our experimental data (Figure 2.4F).

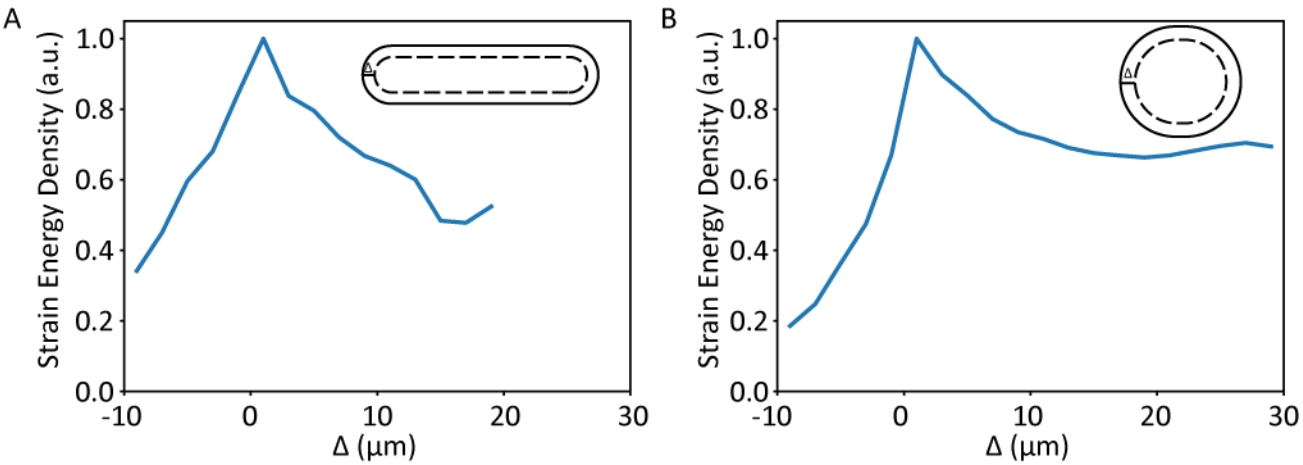

Figure 2.7: Strain energy profiles for simulated colonies with equal areas and varying radii of curvature. Colonies of both geometries exert stresses primarily at the colony periphery, at the elongated special case, (A) r = 22 μm, as well as the nearly circular case, (B) r = 46 μm.

2.4.4 Enhanced cell motility promotes traction stress localization in the colony interior

Since AAVM explicitly accounts for individual cell properties, including tension, adhesion, and motility, we sought to investigate how the interplay between active cell motility and intercellular mechanical coupling regulates stress transmission in the colony. Motile behavior of cells can be induced by increasing the magnitude of the self-propulsion speed, v_0, or by inducing fluid behavior of the colony. Fluidity can be induced by lowering the effective

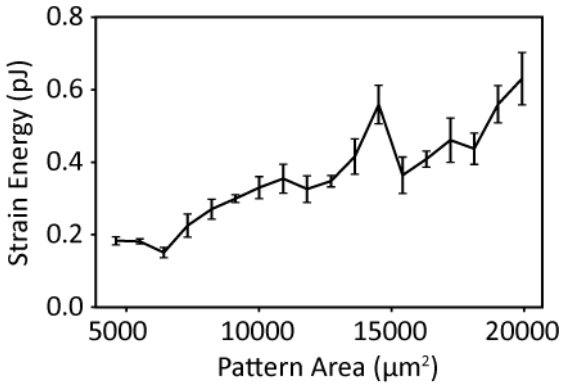

Figure 2.8: The vertex model predicts that the strain energy produced by a colony scales linearly with colony area. This is in agreement with published experimental results for colonies [24][68] and single cells [69].

mechanical tension at cell interfaces by either decreasing cortical tension or by increasing cell–cell adhesion energy. It was recently shown that increase in cell shape anisotropy can reduce the effective tension at cell interfaces, leading to fluidization of a jammed tissue [85]. Cell shape anisotropy can be characterized by the dimensionless preferred shape index, $p_0 = P_0/\sqrt{A_0}$, where P_0 is the preferred cell perimeter and A_0 is the preferred cell area (Materials and Methods). While the molecular mechanisms regulating changes in p_0 remain to be characterized, here we treat p_0 as a control parameter that tunes tissue fluidity by promoting local cell movement and mechanical stress relaxation by cellular neighbor exchanges. Tissue fluidity can be further increased by increasing cell self-propulsion velocity, which increases the propensity of cell–cell rearrangements [92].

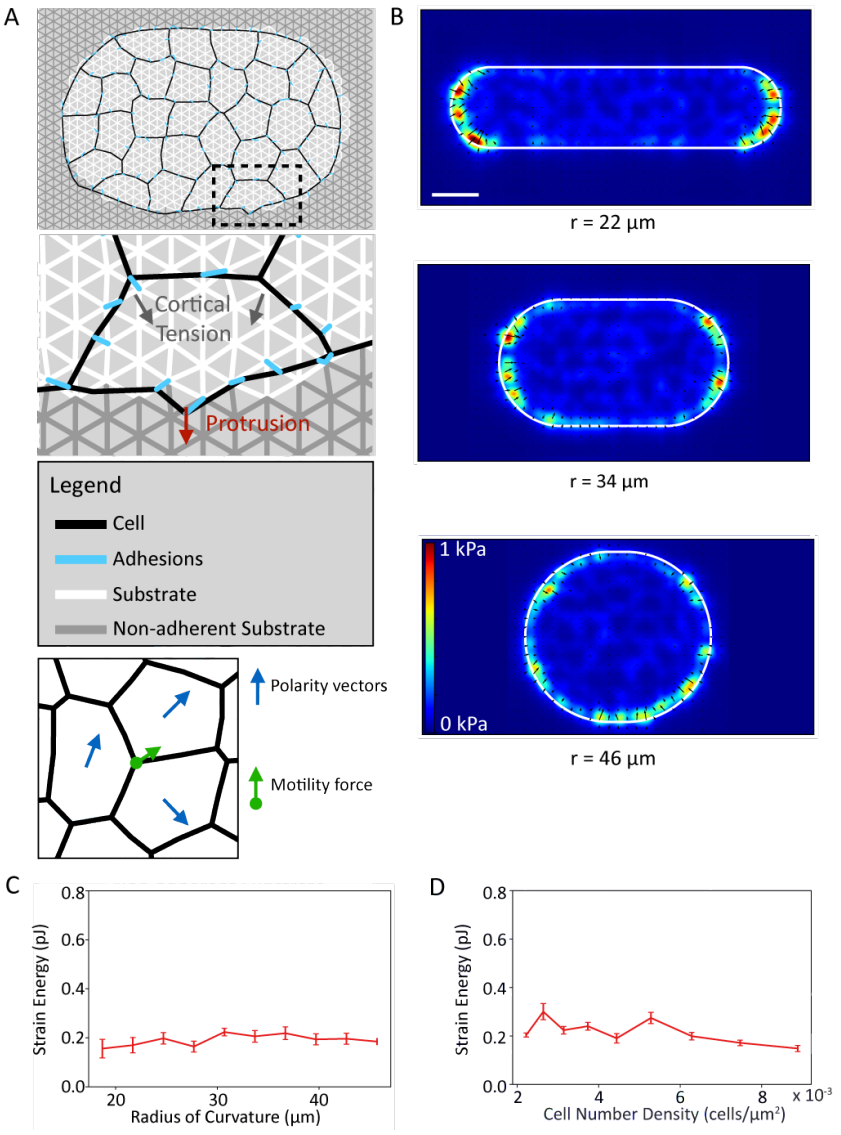

Figure 2.9: Increased cell motility promotes strain energy localization throughout the cell colony. (A) Time-averaged traction stress maps, (B) averaged strain energy density normalized by the boundary value, (C) and cell trajectory plots for low motility cells, $v_0 = 60\mu m$/hr, p_0=3.4 (top), medium motility cells, $v_0 = 90\mu m$/hr, $p_0 = 3.8$ (middle), and high motility cells, $v_0 = 120mum$/hr, $p_0 = 4.2$ (bottom). Δ is the distance from the boundary and is defined as negative outside of the cell colony, and positive inside the cell colony. Scale bar represents 50 μm. (D) Traction stress decay length λ and (E) rate of cell neighbor exchanges (intercalations) for varying cell motility speed and cell shape index. The decay length λ is measured by fitting $SE = Ae^{(-\Delta)/\lambda)}$ to the relevant strain energy density profiles.

As we increase cell motility (by increasing v_0) and tissue fluidity (by increasing p_0), we observe that higher traction stresses are generated in the colony interior (Figure 2.9A). This leads to delocalization of strain energy away from the colony periphery (Figure 2.9B)

and appears in correlation with enhanced cell movement (Figure 2.9C). To quantify the dependence of traction stress distribution on cell motility, we systematically varied the self-propulsion speed, v_0, and the cell shape index, p_0. Over all simulations, we find that the decay length λ of traction stresses from the periphery in relation to cell motility increases monotonically as the mean instantaneous velocity of the cells increases (Figure 2.9D). This quantity is obtained by fitting an exponential function to strain energy density profiles obtained from the earlier annular analysis: $SE = Ae^{\frac{-\Delta}{\lambda}}$ (Materials and Methods). The resulting decay constant provides a length scale over which the strain energy decreases with distance from the colony border, such that a higher value corresponds to a higher proportion of interior stresses. Increasing either the self-propulsion speed or the cell shape index also leads to an increase in the frequency of cellular neighbor exchanges or intercalation rates (Figure 2.9E and Figure 2.10). This increased rate of cell intercalations exhibits a positive correlation with higher internal motility and lower strain energy localization at the colony periphery.

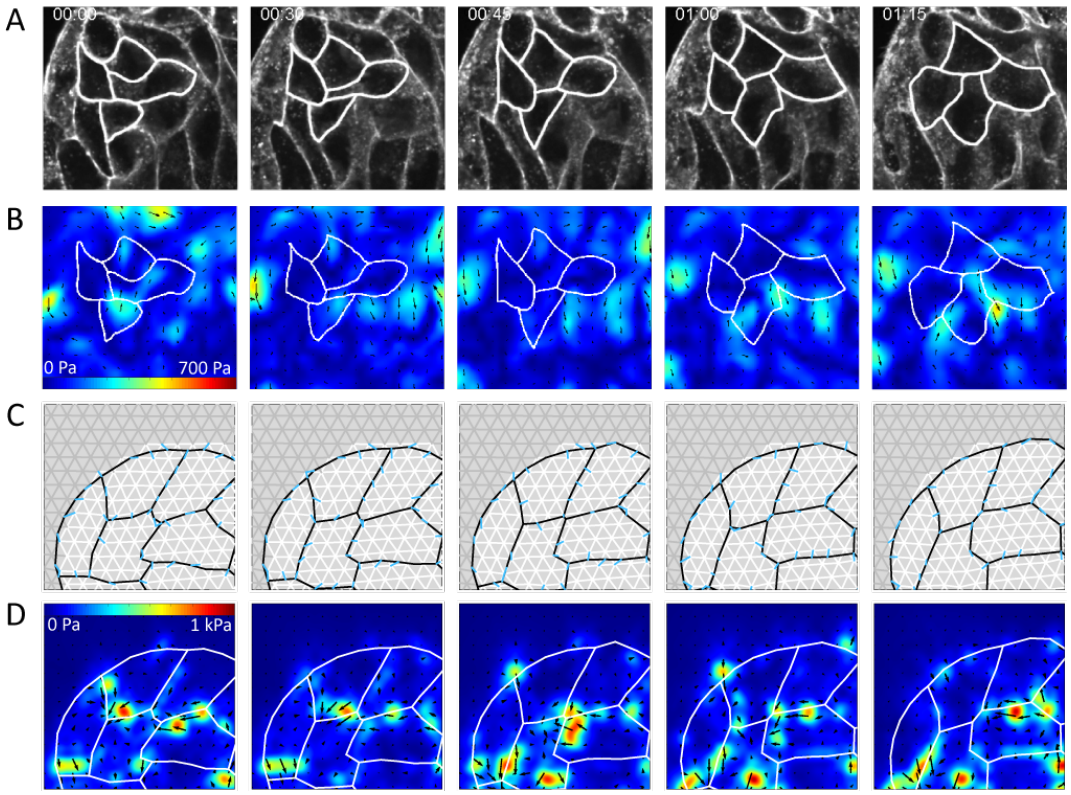

Figure 2.10: Traction stresses associated with cell neighbor exchanges. (A) Stargazin-GFP images of a portion of the colony from a movie over the course of a neighbor exchange. The four participant cells are outlined in white. (B) Traction maps corresponding to (A), showing traction stresses in the vicinity of the exchange event. (C) Cell shapes during a simulated neighbor exchange for a comparable colony. (D) Traction maps corresponding to the event simulated in (C). All scale bars $= 25\ \mu m$.

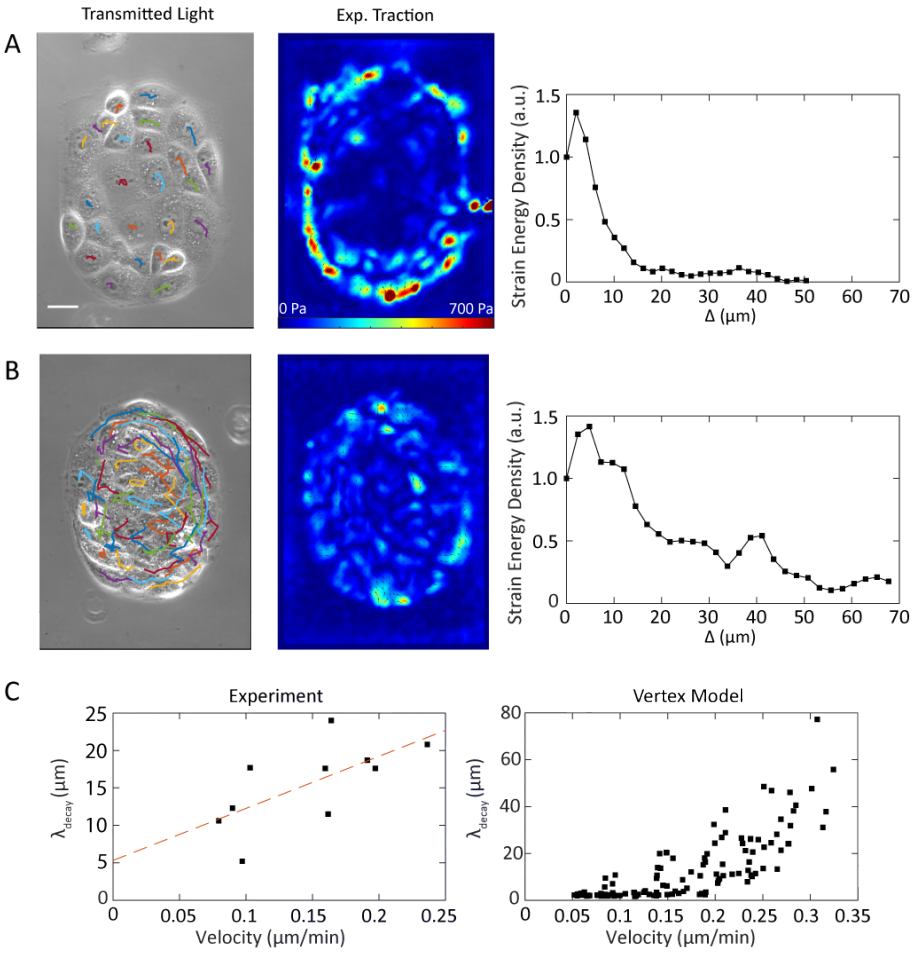

Figure 2.11: Colonies with interior traction stresses exhibit high degree of individual cell motility. (A,B) Colonies with peripheral localization of traction stresses have cells that appear jammed and do not reorganize traction stresses rapidly. By contrast, colonies with interior traction stresses have highly motile cells and exhibit dynamic peaks in traction stresses. From left to right: Phase contrast images and nuclear tracks over 4 h for two colonies of ZO-1/2 dKD MDCK cells, representative traction maps from each colony, and the strain energy density profiles corresponding to the traction maps. Scale bar = 25 μm. (A) A colony with low motility (mean cell speed = 0.079 μm/min) and traction stresses localized to the colony periphery. (B) A colony with higher motility (mean cell speed = 0.236 μm/min) and a higher proportion of internal stresses. (C) Colonies with higher motility have a longer decay length for strain energy as a function of distance from border. This relationship holds in experiments (left) and is predicted by the vertex model (right) to be robust over a wide range of motilities, using each simulation used in Figure 2.9D. The red line in the left panel of (C) shows the linear fit of the data shown with slope = 69.53 and y-intercept = 5.313. The radii of curvature for the colonies shown in (A) and (B) are 65 μm and 70 μm, respectively.

Our experimental results confirmed the model predictions regarding the relationship between individual cell motility and peripheral traction stress localization. Working under the hypothesis that more motile, fluidized colonies may feature more spatially disperse traction

stresses, we considered two representative micropatterned colonies of comparable geometries, which we selected based on differences in mean cell speed over the course of 3.5 h (Figure 2.11, A and B). Figure 2.11A shows representative phase contrast and traction heatmap images from a colony where cells have an average instantaneous velocity of $7.92 \times 10^{-2} \mu m/min$ and travel an average of 16.1 μm over 3.25 h. Cell movement is indicated by the nuclear tracks overlaid on the phase contrast (Figure 2.11A, left panel). In this colony, the traction stresses are visibly confined to the colony periphery (Figure 2.11A, middle panel), an observation that is confirmed by the strain energy profile for that time point (Figure 2.11A, right panel). The same analysis for a colony with considerably higher cell motility, with instantaneous velocity of 0.197 $\mu m/min$ and mean path length of 48.3 μm over 3.25 h (Figure 2.11B, left panel), yields different results. In this case, traction stress peaks are found on both the colony periphery and interior (Figure 2.11B, middle panel), and the strain energy profile reveals a slow decay in strain energy density from the colony border (Figure 2.11B, right panel). These differences in traction stress distribution were concordant with the vertex model predictions (Figure 2.9A)—as the average cell motility in a colony increases, traction stresses reorganize to the colony interior.

We further quantified the relationship between cell motility speed and traction stress organization using the traction stress decay length, λ. We found the average decay length for movies of several colonies, ranging in size from 8000 to 20,000 μm^2, and found that an increase in cell speed was correlated with a higher decay length (Figure 2.11C, left panel). We thus experimentally validated the theoretical prediction that traction stress dispersion should accompany enhanced cell motility (Figure 2.11C, right panel).

2.4.5 Active cell behaviors coordinate localized stress production modes

Our bottom-up computational model and experiments enable us to bridge the gap between single cell dynamics and multicellular mechanical output in adhesive micropatterns. Using this integrative approach, we related the collective modes of traction stress generation in ep-

ithelial colonies with the motile and adhesive behaviors of individual cells (Figures 2.4–2.11). To further apply the predictive power of the AAVM in understanding heterogeneous force transmission in epithelial colonies, we examined two frequently occurring active processes: cell division within a monolayer (Figure 2.12), and spontaneous rotational motion of a colony (Figure 2.13). In a typical mitosis event occurring within a colony, there is significant lateral constriction that occurs prior to a cell division (Figure 2.12A). We further observed that traction stresses gradually reorganize to the region around the mitotic cell (Figure 2.12B, left three panels) and dissipate after cytokinesis (Figure 2.12B, right two panels). This result, while limited spatially by the finite resolution of the TFM analysis, is concordant with published results for single cells [93]. This provides an active mechanism of stress relaxation and movement that locally fluidizes the colony.

To capture this behavior in AAVM, we implemented the mechanics of cell division in four steps (Figure 2.14): 1) a *growth phase*, where the preferred area of the dividing cell is doubled (highlighted in red in Figure 2.12C); 2) a *cell rounding phase*, where an increased line tension on the cell periphery enable cells to adopt a circular shape (Figure 2.14B); 3) a *constriction phase*, where an increased tension at the cell equator results in ingression of the cleavage furrow, around which large traction stresses localize (Figure 2.14B and Figure 2.12D); and 2.9) a *splitting phase*, where the constricting cell separates into two daughter cells (Figure 2.12C). Following cell division, the two daughter cells relax their mechanical energies, which results in traction stress dissipation as the cell shapes reach their equilibrium configurations (Figure 2.12D and Figure 2.14A). This example illustrates how the active vertex model can be used to capture active stress generation and relaxation due to localized cell shape changes (Supplemental Movie S6). In particular, local increases in contractility required to change cell shape prior to division are balanced by localized traction stresses generated by neighboring cells.

Next, we examined the dynamic reorganization of traction stresses in colonies undergoing spontaneous rotational motions. The ability of epithelial cells to undergo collective

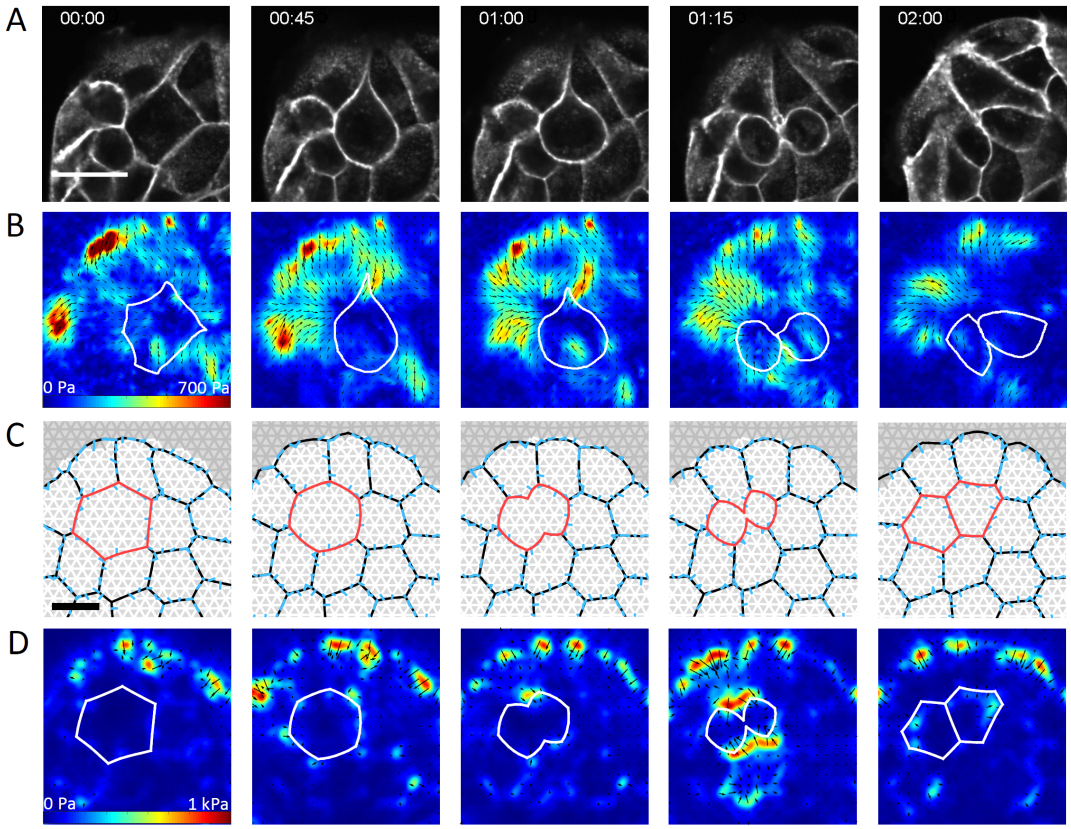

Figure 2.12: Traction stress localization during cell rounding and division. (A) Stargazin-GFP images showing a cell (outlined in white) contracting and dividing. Scale bar = 10 μm. (B) Traction maps corresponding to (A). As the cell contracts, traction stresses are exerted just exterior to the mitotic cell, directed inward towards the plane of division. Once the cell finishes dividing, the stresses begin to dissipate. (C) Cell shapes during a simulated mitotic event in the vertex model, for a low motility cell colony, $v_0 = 30\mu m/\text{hr}$, $p_0 = 3.6$. The dividing cell is highlighted in red. Full details of the cell division implementation are given in the Supplementary Material. (D) Traction maps corresponding to (C).

rotations has been proposed to play an important role in acinus formation, tissue polarity, and embryogenesis [94]. As reported previously [95][96][97], small colonies of epithelial cells can often show spontaneous collective rotational motion, with few internal rearrangements (Figure 2.13A). The limited number of internal rearrangements corresponds to high cohesiveness (low p_0), which is essential for efficient transmission of contact guidance cues from peripheral to interior cells. Based on our findings in Figure 2.9E, lower fluidity (low p_0) would promote a higher degree of peripheral stress localization. Instead, our traction force measurements show abundant internal traction stresses (Figure 2.13B).

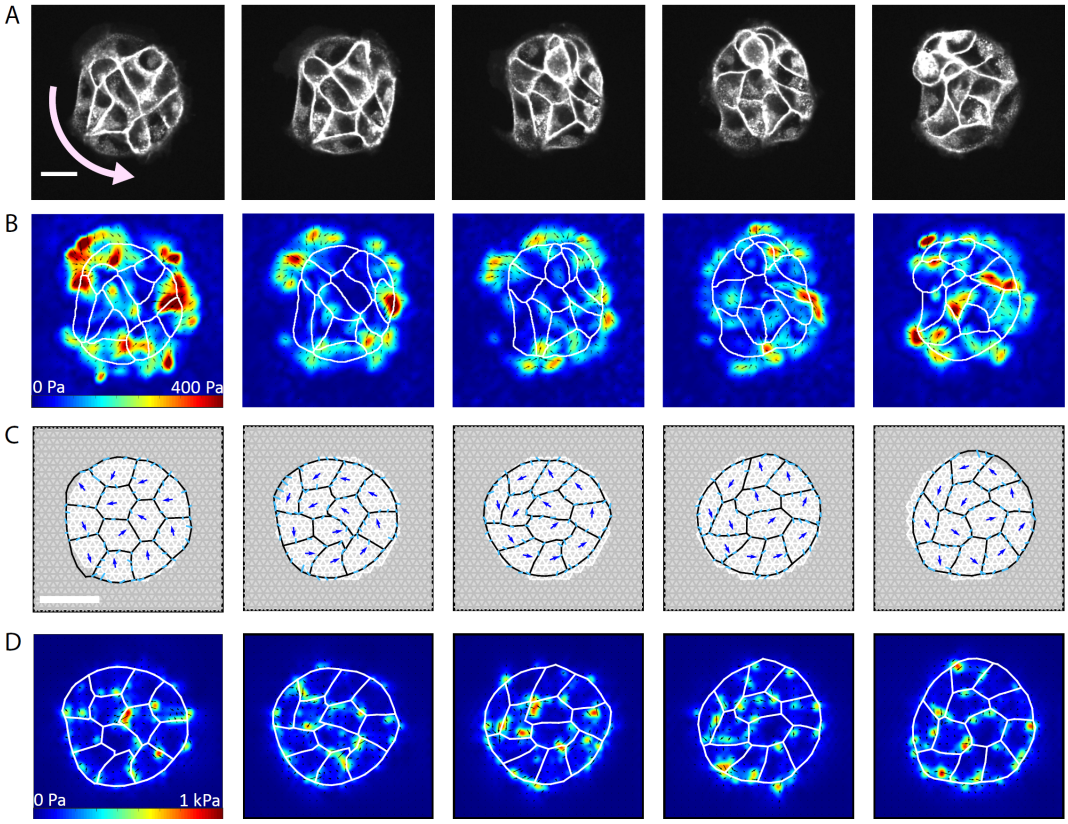

Figure 2.13: Internal traction stresses form during colony rotation. (A) Stargazin-GFP images of a colony on a circular pattern (radius of curvature = 47.5 µm) rotating counter-clockwise about the pattern center. Scale bar = 25 μm, curved arrow indicates direction of motion. (B) Traction maps corresponding to (A). (C) Cell shapes during rotation simulated by the vertex model, for high motility, $v_0 = 90\mu m/\text{hr}$, $p_0 = 3.8$. Blue arrows show the direction of cell motion. Cell polarities align with cell velocity with timescale $\tau_v = 30$ mins, and turn away from the micropattern boundary with timescale $\tau_b = 6$ mins. Full details can be found in the Supplementary Material. (D) Traction maps corresponding to (C).

To recapitulate coordinated cell motion, we simulated a cohesive cell colony with low internal motility $\left(v_0 = 60\ \mu m\ h^{-1}, p_0 = 3.6\right)$, where the cell polarity vectors now align with cell center velocities and are repelled by the pattern boundary (see Supplemental Material). The interplay between polarity alignment with local motion and confinement within the pattern results in a coordinated spontaneous rotational motion of the colony (Figure 2.13C). In the simulations, we find large internal traction stresses localize as the colony coherently rotates (Figure 2.13D). These stresses are subsequently dissipated as the cell polarity vectors change in direction during synchronized rotation. This underscores that internal traction stresses can result from coordinated movement due to long-range transmission of mechanical

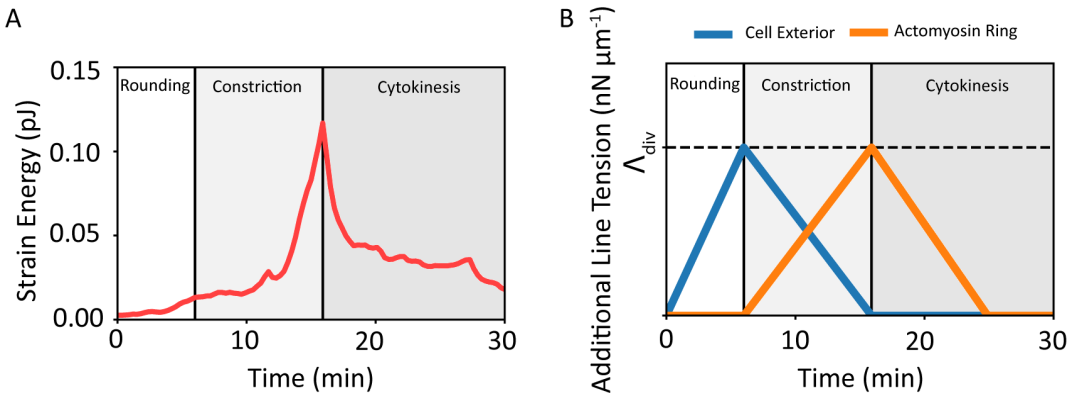

Figure 2.14: (A) Strain energy increases during the simulated cell division process, and dissipates after the division is over. The initial rounding phase produces only a modest elevation in stresses, but increased tension along the periphery of the mitotic cell leads to a dramatic increase in strain energy. After the splitting phase, the daughter cells relax their tension and the strain energy is concomitantly reduced. (B) Additional line tensions during the different phases of cell division. The actomyosin ring is an edge that connects vertices on opposite sides of the side. As its tension increases the cell pinches in two. After the cell divides, this edge becomes the interface between the two daughter cells.

cues by adhesive epithelial cells.

2.5 Discussion

Our work established the relative roles of cell motility and cell–cell interactions on force transmission in multicellular colonies. Through integration of experiments, bottom-up and top-down modeling approaches, we have shown that colony geometry, contractility, cell shape changes, and active motion of constituent cells can profoundly alter the spatial organization of mechanical stresses transmitted to the extracellular matrix. These results provide a robust framework to characterize the role of cell density, motility, geometrical, and mechanical cues on collective cell behavior in adhesive environments.

Our results indicate that epithelial colonies organize traction stresses either peripherally or internally (Figure 2.3) depending on the motile and adhesive behaviors of individual cells. First, we consider the case of cohesive cell colonies exhibiting strong peripheral localization of traction stresses. Consistent with previous results in keratinocytes [68], we find that internal stresses counterbalance in strongly coherent and immobile colonies of cells such that

traction stresses become localized to the periphery (Figure 2.4). The resultant mechanical work performed by the colony on the substrate is independent of the colony shape or cell density but is proportional to changes in the colony spread area. These findings are consistent with the physical model of a colony described by a characteristic contractility (Figure 2, A and D).

Continuum models that treat the multicellular colony as a uniform contractile medium [68] capture this peripheral localization for circular shaped colonies. In previous work on single adherent cells [69], we found that an additional edge contractility was required to capture the traction localization to regions of high curvatures for cells of arbitrary shapes. Here, we find that peripheral contractility is also needed to describe the distribution of traction stresses in multicellular colonies of arbitrary shapes. This edge contractility, characterized by a line tension, naturally arises due to the absence of cell–cell adhesion at free edges, resulting in traction stress localization to regions of curvature. However, this model was insufficient to describe the mechanics of cohesive colonies with sizeable tractions in the interior that fluctuated in space and time (Figures 2.3B and 2.11B). This necessitated a cell-based model, AAVM, that accounts for individual cell activity, motility, shape, and mechanics (Figure 2.5A).

While previous work showed that traction stress localization within the colony interior could be explained by loss of cell cohesion [24], here instead the cells remained cohesive over time, exhibiting local dynamic behaviors. We observed that cells within colonies tend to move, exchange neighbors, and change their individual shapes. We therefore developed a new active adherent vertex model that allowed us to capture the dynamic properties of these adherent colonies. By coupling the AAVM to an elastic substrate, we predicted that internal cell motility leading to effective tissue fluidization resulted in a high degree of internal localization of traction stresses (Figure 2.9). This result was confirmed by our experimental data that showed that the length scale for traction stress penetration increased with increasing cell motility (Figure 2.11). Our model also captures the traction stress field

around a motile cell traversing the colony, which likely arises from weakening of cell–cell adhesions (Figure 2.15).

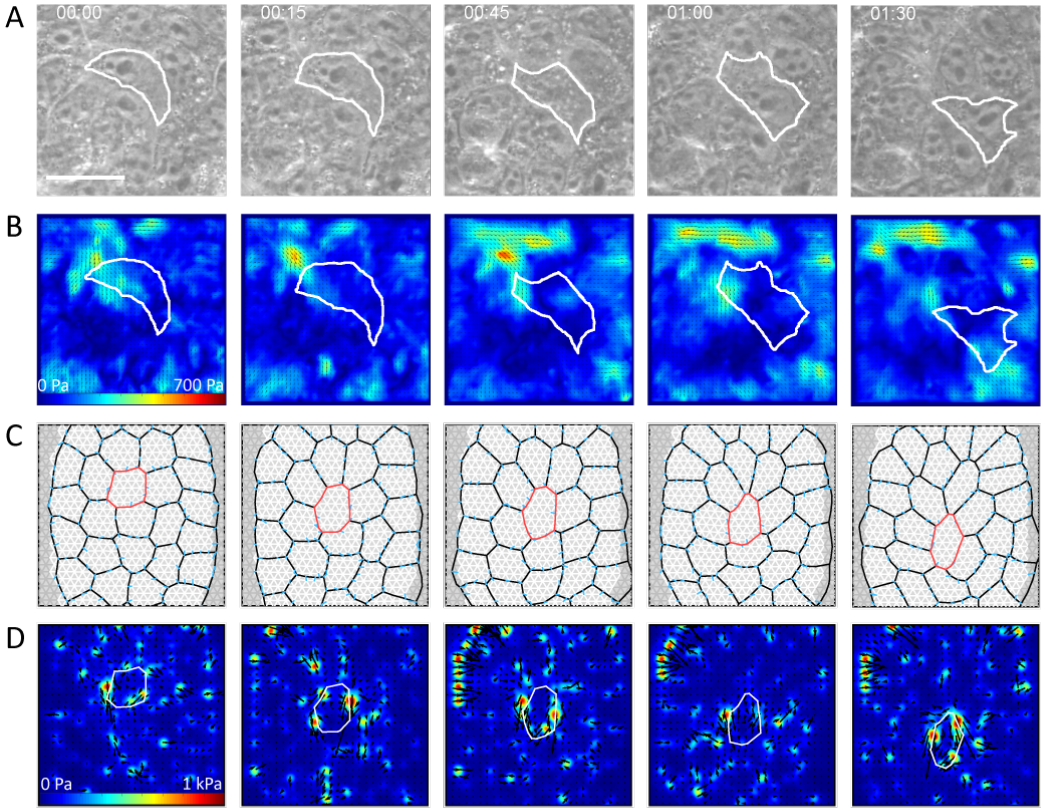

Figure 2.15: Traction stresses associated with high single-cell motility within a colony. (A) Phase contrast images of a cell moving through the bulk of a colony of MDCK cells. The motile cell is outlined in white. (B) Traction stress heatmaps corresponding to the images in (A), showing a small peak in the stresses that appears to follow one of the cell vertices along the trailing edge, although the specific location is limited by the size resolution of stress peaks. (C) Vertex model simulation of a cell deforming and moving through the colony bulk. The motile cell is outlined in red. (D) Traction stress heatmaps corresponding to the simulated cell shapes in (D), demonstrating the accumulation of stresses along vertices on both the leading and trailing edges of the motile cell.

Aside from motility driven fluidization, traction stress fluctuations in the bulk of cohesive colonies also occurred due to cell division and rotations. Contractility-driven shape changes in dividing cells can locally accumulate traction stresses. These stresses are subsequently dissipated following daughter cell separation once cell–cell cohesion is established (Figure 6). We also found traction stress dispersion in colonies with low internal motility but where there was highly correlated rotational motion (Figure 2.13). These persistent rotations have

been previously observed in small cohesive colonies in adhesive micropatterns [95][96][97]. Consistent with previous findings, we find that traction stresses periodically accumulate and dissipate at cell–cell junctions of rotating colonies, arising from coherent transmission of polarity cues by contact guidance. Thus, colonies with the same geometry and adhesive properties can exhibit a rich variety of dynamic properties due to active mechanical behaviors of constituent cells.

In conclusion, we have shown that an interplay between cell motility and cell–cell adhesive interactions can tune the dynamic mechanical properties of cohesive colonies in confined adhesive environments. In doing so, we have developed a quantitatively accurate bottom-up model for dynamic epithelial colonies that allows us to predict patterns of collective motion and traction stress generation in diverse conditions. In particular, we show that local active cell behaviors (motility, intercalations, division) in cohesive tissues can induce heterogeneous properties that cannot be captured by simple continuum models. In the absence of active cell dynamics, however, immobile colonies transmit forces like a continuum medium, akin to single adherent cells. These results provide a quantitative framework to predict collective dynamic and mechanical states of epithelial tissues from their emergent patterns of force transmission.

CHAPTER 3

PHOTOELECTRIC SILICON NANOSTRUCTURES FOR CALCIUM MODULATION IN SMOOTH MUSCLE TISSUES

3.1 Preface

This chapter comprises present work on a forthcoming manuscript to be submitted for publication. The author conducted all experiments and performed all analysis with guidance and suggestions from Margaret L. Gardel and Bozhi Tian. Except where noted, all computational routines were developed by the author. Menahem Y. Rotenberg helped with the optical mapping routines and was very helpful in troubleshooting nanowire stimulation. Kelliann Koehler synthesized the nanowires used in this work.

3.2 Introduction

In recent years, bioelectronic devices in general, and nanoscale bioelectronics in particular, have garnered large amounts of interest for therapeutic applications. In order to validate these uses and identify promising future areas, it is important to examine interface formation as well as modulatory effects across many length scales. The development of bioelectronics has historically been inextricably linked with miniaturization, beginning with Galvani's investigations using frog legs[98], through Hodgkin and Huxley's giant axon electrode studies[99][100], and up to current research using nanoscale devices to examine interactions at the single-cell and even subcellular level[101][102][103]. Recent multi-scale innovations have included a closed-loop system for neural control over bionic arms based on microelectrode arrays[104], nanowire arrays integrated with flexible substrates to modulate pacing in cardiac cells using optical stimulation[49], and the use of upconversion nanoparticles to facilitate infrared vision in mice[105]. From these results and others, it is evident that nanomaterials possess considerable potential for translation up to tissue and organism level effects. In this

work, we investigate the use of silicon nanowires as devices to modulate behavior at the single cell and colony level, and develop a set of analytic tools to discern effects at multiple length scales.

Silicon nanowires (SiNWs) have been deployed in the last 20 years to a great number of biological contexts, ranging from intracellular electrical sensing[103][106], to three-dimensional electronic cell scaffolding[107], to providing photoelectric[53][108] and photothermal[47][51] stimulation in a wide variety of cell and tissue types. The most common means of engineering functionality in them is to synthesize core-shell nanowires with varying levels of dopant in the respective layers using a chemical vapor deposition apparatus[109][110]. The resulting structures can contain coaxial p-n or p-i-n junctions, and display photoinduced charge separation the same as other similar semiconductor junctions[111]. These SiNWs possess a number of characteristics that make them highly desirable and complementary to existing techniques for biological modulation. They can possess similar functionality to microelectrodes, but may be completely leadless and therefore less invasive[46]. Like chemical perturbations, they can be easily administered to biological samples and can act at the subcellular level, but they may also be selectively activated, allowing for spatial resolution in stimulation[53]. This subcellular activity and selective activation is thus similar to optogenetic techniques, but since they are nongenetic they require far less intensive preparation and the ethical considerations are more straightforward in, e.g., primate or human subjects.

Human airway smooth muscle (HASM) cells are present in the trachea and surrounding the bronchial lumen in the bronchial tree[40]. In their function as smooth muscle cells, they are pivotal in maintaining brochomotor tone[40][112], but they have also been suggested to be involved in immune system response and inflammation in the airway[113][114]. Notably, inflammatory responses in HASM tissues are a major component of asthmatic phenotypes[115], and have been implicated in asthma attacks as well as the immune response to rhinovirus in asthmatic patients[116]. HASM contractility is regulated largely in accordance with the canonical picture of vascular smooth muscle excitation-contraction coupling, with certain

key differences arising in the coordination of ionic currents in membrane depolarization and repolarization[117]. Namely, cholinergic agonists, e.g., acetylcholine, can interact with G-protein coupled receptors to induce the release of secondary messengers. These, in turn, activate the Rho/ROCK signaling pathway, while inositol triphosphate (IP_3) additionally opens IP_3 receptor channels in the sarcoplasmic reticulum to release calcium ions into the cytosol. Intracellular Ca^{2+} can then interact with myosin light chain kinase to facilitate contractility, which is aided by the activity of ROCK. Throughout this process, the membrane potential and intracellular Ca^{2+} concentration are carefully regulated[117][118].

The central role of calcium in regulating contractility has made it an important topic of inquiry for smooth muscle tissues, including HASM tissues[119]. A particularly notable phenomenon is the presence of asynchronous oscillations[120]. The first report of asynchronous oscillations of intracellular Ca^{2+} levels in smooth muscle cells emerged in 1994[121], when they were visualized in rat tail arteries. Since then, they have been reported in other smooth muscle contexts, including in human lung slices, i.e., HASM tissues[122]. Such asynchronous oscillations are thought to regulate tonic contraction[123], as opposed to synchronized oscillations, which induce oscillatory contractions. Therefore, in HASM tissues, asynchronous oscillations are the means for the maintenance of brochomotor tone. Compared to oscillations in other excitable cell types, the asynchronous oscillations of smooth muscle cells are slow, with frequencies on the order of 2 - 3 cycles/min[124]. Because of the functional importance of these oscillations, a number of studies have considered means of altering the frequency, mostly through pharmacological means[124][125].

Here, we report on the application of p-i-n SiNWs to modulate Ca^{2+} signaling in HASM cells. Our rationale for this application was based on the electric excitability of HASM cells, and the well-known ability of p-i-n SiNWs to induce calcium fluxes in response to optical stimulation in numerous cell types[49][53][63]. First, we characterize the NW-cell interface with respect to key structural components, finding that NW association is non-perturbative to the actin cytoskeleton, focal adhesions, or gap junctions. We then introduce an analytic

framework for characterizing asynchronous oscillations in stimulated and unstimulated, geometrically controlled colonies of HASM cells. Finally, we apply the optical control provided to us by p-i-n SiNWs with unprecedented cell-level specificity in modulating HASM Ca^{2+} activity with a nongenetic, drug-like delivery system. Further analysis of the stimulation reveals that optical stimulation induces large spikes in Ca^{2+} concentration at stimulation sites, and can lower the frequency of oscillations in adjacent cells.

3.3 Materials and Methods

3.3.1 Cell Culture

Human airway smooth muscle (HASM) cells were provided courtesy of Julian Solway. The cells were cultured in DMEM/Hams F-12 50/50 Mix with L-glutamine (Corning, Corning, NY) and supplemented with 10% fetal bovine serum (Mediatech; Corning), additional L-glutamine to 2 mM (Corning), penicillin-strepomycin (Corning), and antibiotic-antimycotic solution (Corning). Cells were thawed from liquid nitrogen storage at second passage and only imaged at passage numbers 3-5.

3.3.2 Polyacrylamide (PAA) Gels

PAA gel substrates were prepared as previously reported in Oakes et al., 2014[69] and Schaumann et al., 2018[74]. A stock solution for making gels of Young modulus 16 kPA consisted of a mixture of 3.125 mL 40% acrylamide (Bio-Rad Laboratories, Hercules, CA), 1.67 mL 2% bis-acrylamide (Bio-Rad), and 0.21 mL water. To prepare the gels, 150 μL of standard solution were mixed with 347 mL of water, 0.75 μL tetramethylethylenediamine (Sigma-Aldrich), and 2.5 μL of ammonium persulfate (Sigma-Aldrich).

3.3.3 Unpatterned Substrates

For experiments with no collagen patterning, PAA gels were mixed as described above and polymerized while sandwiched between activated coverslips and glass slides treated with Rain-X (ITW Global Brands, Houston, TX). For each 25 mm round coverslip, 800 μL of 2.5 mg/mL Sulfo-SANPAH (Pierce; Thermo-Fisher, Waltham, MA) were added to the surface of each gel. To form crosslinks amenable to ECM protein deposition, the gels were then exposed to UV light for 5 minutes. Afterwards, the gels were washed in DI water, spin dried, and inverted onto 50 μL drops of 100 $\mu g/mL$ collagen in MES buffer overnight at $4°C$.

3.3.4 Micropatterned Substrates

Patterned gels were prepared as reported in Schaumann et al., 2018[74], based on a protocol developed in Tseng et al., 2011[70]. Briefly, PAA gells were mixed as described above and polymerized while sandwiched between activated coverslips and a quartz/chrome photomask. The gels were then illuminated through the photomask with 185 nm and 254 nm light in a UVO-Cleaner 342 (Jelight, Irvine, CA) for 110 seconds, which activated only the regions exposed to light. The coverslip and gel were then removed from the photomask by submerging the entire complex in water and gently detaching a corner with a razor blade. Gels were incubated for 10-15 min in a solution containing 5 mg/ml 1-ethyl-3-(3-dimethylaminopropyl)carbodiimide hydrochloride (EDC) (Thermo-Fisher) and 10 mg/ml N-hydroxysuccinimide (NHS) (Thermo-Fisher) in water. The EDC/NHS solution was aspirated and replaced with a solution containing 0.5 mg/ml collagen-I in an MES buffer for 40 min.

3.3.5 Microscopy and Calcium Imaging

Cells were imaged on an inverted scanning confocal/airydisk microscope (LSM 980; Zeiss, Oberkochen, Germany) with a GaAsP PMT detector. Image acquisition and microscope

control was done using Zen 3.1 Blue management software (Zeiss). To monitor changes in cytosolic calcium concentration, fluo-8 AM (AAT BioQuest, Sunnyvale, CA) was added to samples to be imaged at a final concentration of 3.75 μM. Fluo-8 treated cells were placed back in the incubator for 25 minutes, at which point the medium was replaced with fresh culture medium supplemented with 10 mM 4-(2-hydroxyethyl)-1-piperazineethanesulfonic acid (HEPES). The samples were then transferred immediately to the microscope and imaged.

3.3.6 Silicon Nanowires for Photostimulation

Coaxial p-i-n silicon nanowires (SiNWs) were provided courtesy of Kelliann Koehler and prepared as reported in Parameswaran, et al., 2018[53]. This method uses gold nanoclusters as catalysts to form nanowires in a chemical vapor deposition apparatus. First, 50 nm diameter citrate-stabilized Au nanoparticles (Ted Pella, Redding, CA) were added to Si $\langle 100 \rangle$ substrates (Nova Electronic Materials, n-type, 0.001-0.005 Ωcm). Silane (SiH_4), diboron (B_2H_6, 100 ppm in H_2), and phosphine (PH_3, 1000 ppm in H_2) were used as Si reactant, p-type dopant, and n-type dopant, respectively during the synthesis. H_2 was the carrier gas. The synthesis process occurred in four phases: p-type NW formation, a pause for temperature equilibration, intrinsic shell deposition, and n-type shell deposition. The relevant parameters - temperature, pressure, time, and flow rate of each reagent - were in accordance with Table 3.1.

Phase	Time (min)	Temp $°C$	Pressure (torr)	SiH_4 (sccm)	B_2H_6 (sccm)	PH_3 (sccm)	H_2 (sccm)
p-type NW	30	470	40	2	10	0	60
Pause	20	750	0	0	0	0	0
Intrinsic shell	15	750	20	0.6	0	0	60
n-type shell	15	750	20	0.3	0	1.5	60

Table 3.1: Growth parameters for coaxial p-i-n SiNW synthesis.

3.3.7 Immunofluorescence

Immunofluorescence investigations followed standard fixation and staining protocols. Cells were added to 25 mm round coverglass and left to grow for 24 h. Then, SiNWs were

added to each sample. In lieu of a quantitative method for dosing the number of SiNWs added, different volumes from the same SiNW-containing mixture functioned to alter the dosage. The samples were then placed back in the incubator and left for another 24 h to allow for possible SiNW-cell interactions. At the end of this period, cells were fixed using a solution of 4% paraformaldehyde, 0.5% Triton-X100, and 2.5% bovine serum albumin in PBS for 15 minutes. The staining solution was composed of DPBS with 0.5% Triton-X100 and 2.5% bovine serum albumin. Primary antibodies were rabbit anti-Cx43 (clone number EPR22955-101; Abcam, Cambridge, United Kingdom) at a 1:50 dilution, mouse anti-vinculin (catalog number V9131, Sigma-Aldrich) at a 1:100 dilution, and phalloidin-AlexaFluor488 at a 1:800 dilution. Secondary antibodies were anti-rabbit-AlexaFluor647 and anti-mouse-AlexaFluor568, both at a dilution factor of 1:800.

3.3.8 Calcium oscillation characterization

Movies showing fluo-8 fluorescence in cells and colonies were segmented by hand in ImageJ, using the built-in ROI manager to generate a binary mask that was true for every pixel that was within an oscillatory cell. Normalized change in fluorescence (dF/F_0) movies were produced using a freely available ImageJ plugin. The remainder of the analysis was conducted using a home-built routine written in Python 3.7. For a given cell at a given time point, the signal was calculated as the average dF/F_0 pixel intensity within the cell. Correlation matrices showing the value of Pearson's correlation coefficient for all combinations of cells within a movie were produced using the built-in corrmat function available in the pandas package. Changes in oscillation frequency for individual cells and groups thereof were characterized by plotting the magnitude of the Fourier transform of each time series and observing the frequency with the highest power.

3.4 Results

3.4.1 Silicon nanowires form non-invasive interfaces with HASM cytoskeletons

The development of SiNWs as tools for biological modulation and sensing is comparatively recent, and as such, there are only a few cell types for which there are reports in the literature characterizing the cell-NW interfaces. To understand the nature of NW interactions with HASMs, we employed immunofluorescence to visualize key cytoskeletal targets alongside NW location. The NWs themselves are hydrogen-terminated after washing in HF, and as such do not interact with antibodies. Rather, they are visualized by monitoring the reflected light from 491 nm illumination, similar to procedures that have been described elsewhere.

We found the presence of NWs to be largely non-invasive, with minimal impacts on actin architecture, focal adhesion maturation, or gap junction formation (Fig **??**). In two-dimensional culture without the presence of nanowires, the organization of actin in HASMs is defined by thick, prominent bundles of crosslinked actin called stress fibers, which are aligned along the long axis of each cell. Within isotropic cells, which are more abundant shortly after cell division or when cells are freshly plated, the orientation of the stress fibers remains strongly preferential towards a particular axis. The addition of NWs does not appear to affect this in any meaningful way, as cells with associated NWs display the same essential characteristics.

To examine focal adhesion (FA) activity, we stained for vinculin, a focal adhesion protein that is associated with mature FA plaques, i.e., FAs that have increased in size and recruited a suite of associated proteins in response to cytoskeletal signaling. FAs are the subcellular structures that represent the interface of the cytoskeleton and the extracellular environment, namely the substrate, and in this capacity act as the sites of force transmission between cells and their substrates. After 48 h of culturing, HASMs display large, mature FA plaques at the terminal ends of stress fibers, consistent with most other cell types. Interactions with NWs do not appear to alter this, with NW-associated cells displaying a similar incidence and

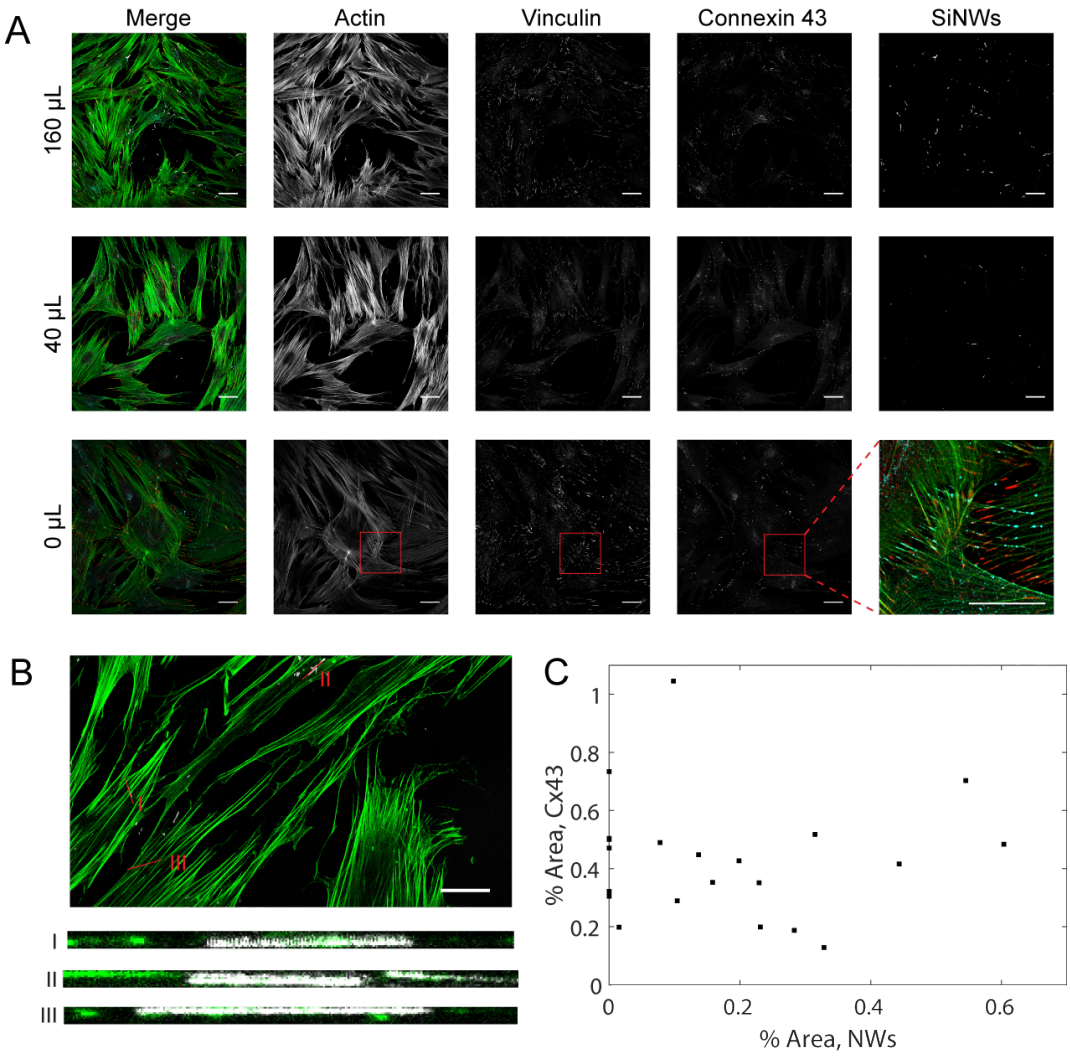

Figure 3.1: SiNWs associate with cells without significant alterations to cytoskeletal structure. (A) (B) (C) All scale bars = 25 μm

size of FAs as compared to the control. Interestingly, we also found no evidence of FA-NW colocalization, suggesting that there is no coordination between NW interface formation and force transmission at the individual cell level.

Finally, we stained for connexin-43 (Cx43), a gap junction marker, to see whether NWs altered electrical connectivity in cells. Broadly speaking, gap junctions are the sites of intercellular electrical communication, as they allow for ionic fluxes to pass through from one cell to another. Cx43 is a transmembrane gap junction protein that is present in most cell types and is thus a good candidate for monitoring the expression of gap junctions. In HASMs

without NWs, Cx43 is visible as small, highly concentrated circular plaques that punctuate the ends of long actin protrusions around cell-cell interfaces. Again, the addition of NWs changes neither the morphology of such plaques, nor the incidence thereof (Figure 3.1C). From these results, we concluded that SiNWs do not perturb the cytoskeletal architecture of HASMs, irrespective of the number or size of NWs present per cell. This raised the possibility that the NWs, in fact, were not interface-forming in the first place, and the lack of noticeable cytoskeletal impact was simply because there were no interactions. To examine this question further, we visualized the position of NWs in the z-direction, relative to the actin channel (Figure 3.1B). These results suggested different degrees of interaction with the actin cytoskeleton. In the case of certain NWs, actin is visible above and below the reflected light from the NWs. Because the resolution in the z-direction is considerably coarser than in the xy-direction, this does not necessarily prove that the NWs are completely internalized in the cell, however, it does suggest that there is a heavy degree of interaction between the NW and cytoskeleton, with the NW potentially even being entangled within actin filaments that compose the stress fibers.

3.4.2 Calcium signaling in HASM colonies is characterized by asynchronous oscillations

To verify our model system of HASMs on patterned substrates, we characterized their calcium signaling in the absence of NW-mediated stimulation. The colonies we imaged typically contained between 150 and 250 cells, with a high proportion of them displaying oscillations. To characterize calcium signaling within individual cells as well as the entirety of the colonies, we produced maps of each movie, where the gray value of each pixel corresponded to the cell that contained that pixel (see Materials and Methods). This allowed us to track changes in fluo-8 fluorescence within each cell as a function of time, and to encode the complete measurements for each cell in the form of an m x n matrix $\mathbf{S}$, where m is the number of cells, n is the number of time points, S_{ij} is the average dF/F_0 signal within the ith cell at the

jth time point, and the ith row represents the time series for the ith cell (Figure 3.2). This organizational scheme for monitoring the signal at multiple sites is fundamentally identical to other multiplexed electrophysiological recordings[126][127], using change in fluorescence as an input rather than, e.g., membrane potential.

Using this methodology, we can rapidly obtain and process data for entire colonies; the limiting factor is typically the time required to segment the cells, although this process may also be automated in the future using parcellation techniques. We used this to monitor the calcium activity of micropatterned colonies to assess the development of signaling for cells under geometric confinement. We selected large rectangular patterns for a number of reasons. Firstly, the shape of the pattern imposes a degree of nematic ordering upon the cells, as the long axis of the cells aligns with the long axis of the rectangle (Figure 3.3A and Figure 3.5H). Because gap junctions were mostly observed at the protrusive ends of cells, this means that controlling the colony geometry can impose a degree of control over the direction of cell-cell transmission. Micropatterning also introduces a degree of crowding to the cells, helping to ensure good cell-cell junction formation. Compared to the patterned samples, unpatterned colonies tended to be sparser and display lower frequencies of oscillations.

To verify that our patterned samples displayed the same essential physiological characteristics as HASM tissues, we observed intracellular calcium levels over time in colonies with no NWs added, one of which is indicated in Figure 3.3A. As was expected, individual cells cycled between high and low calcium levels at low frequencies, approximately 0.5 - 3 cycles/min (Figure 3.3B,C). This was consistent with previously reported rates in tissue slices and other smooth muscle types. A cursory inspection of the signaling patterns suggested that individual cells were periodic in their oscillations, but that the phase and frequency of oscillation was not synchronized with neighbors (Figure 3.3C). To verify this, we examined correlation matrices for the signals from all cells within a given colony. The correlation matrix $\mathbf{C}$ is constructed such that the value of C_{ij} is the Pearson's correlation coefficient R of the signals from cells i and j. For R to be close to unity, two signals must not only have similar frequencies,

but they must be in phase with each other as well. As such, R is an effective measure of how synchronized pairs of cells are. For colonies with no nanowires, the correlation matrices showed correlations mostly limited to $-0.2 < R < 0.4$, suggesting that most cell pairs are either out of phase or at different frequencies with each other, even when they are in close proximity with one another.

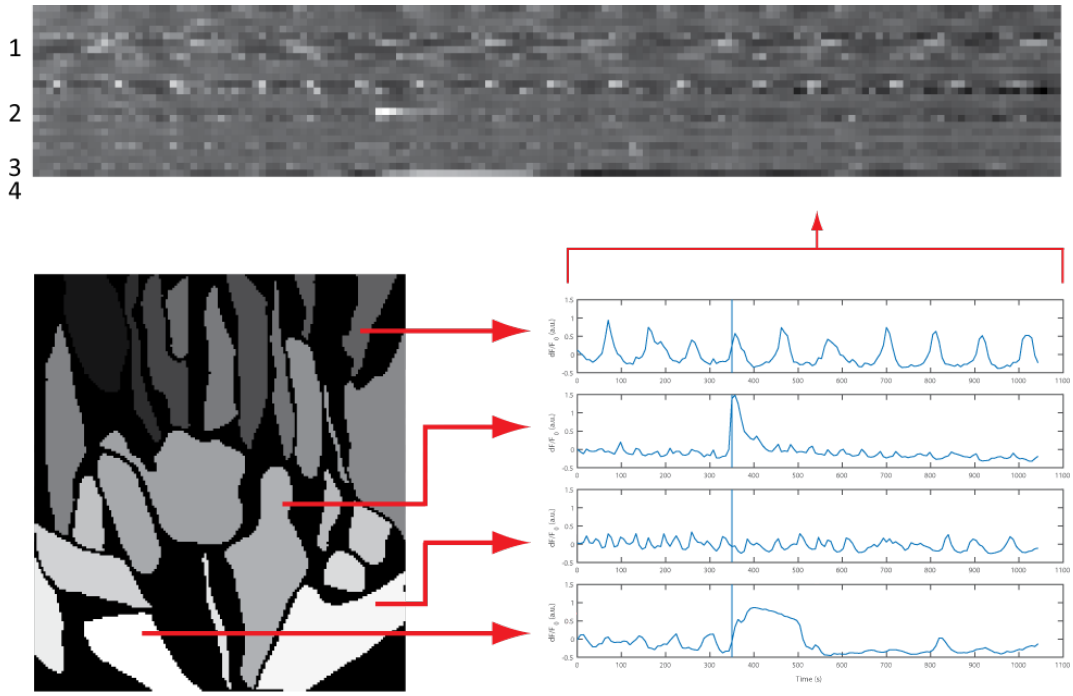

Figure 3.2: Schematic of analytic pipeline for calcium signaling in HASMs. Movies of fluo-8 (Ca^{2+} indicator) fluorescence are segmented by hand to yield maps identifying the location of each cell. The average dF/F_0 signal within each cell can thus be measured and presented as charts of time series. For convenience and ease of pattern identification, the charts for all cells can be compressed down to m x n matrices where each row contains the time series for a single cell. When displayed as images, the gray value indicates the change in fluorescence for a given cell at a given time point. By examining such images row by row, changes in oscillation magnitude and frequency can be quickly located and correlated to location using the labeled map.

3.4.3 Stimulation of NWs in HASMs produces calcium waves

We examined the impact of photostimulation using coaxial p-i-n SiNWs in large and small colonies. Compared to other cell types that have been examined using similar methods,

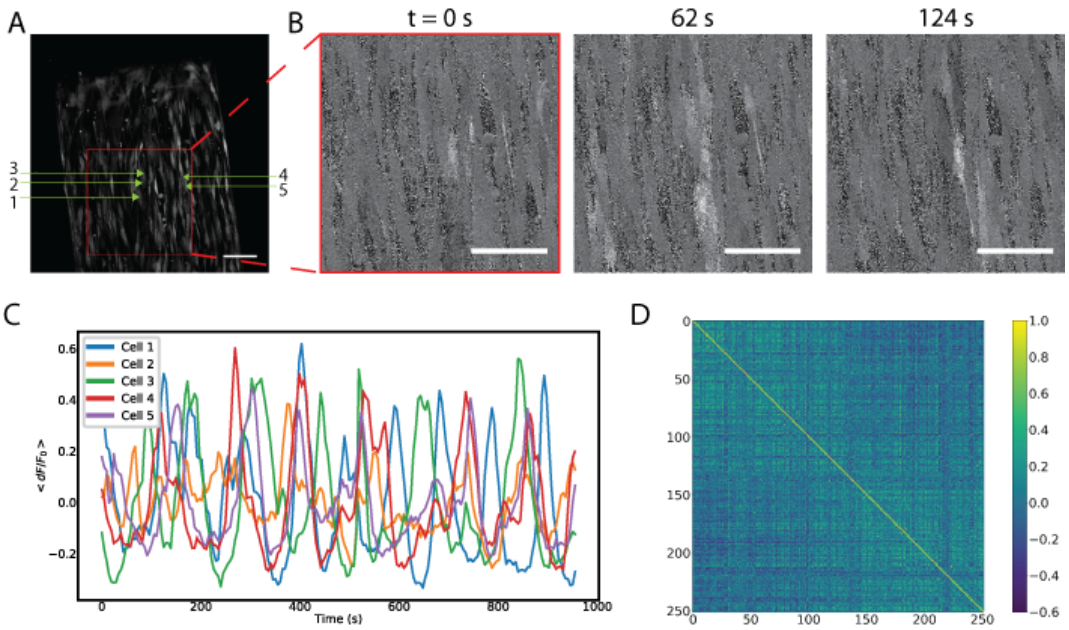

Figure 3.3: Ca^{2+} oscillations in HASM colonies are periodic and uncorrelated. (A) Fluo-8 fluorescence of a patterned colony of HASM cells. Red box indicates zoom-in for subsequent panels, green arrows indicate cell locations for sampling in panel C. (B) Time course of dF/F_0 signal for calcium levels in zoomed-in region of the colony depicted in A. (C) dF/F_0 signals for the five cells indicated in panel A. Each cell displays a periodic oscillatory character, but there is no evident synchronization between them, despite their close proximity to each other. (D) Correlation matrix $\mathbf{C}$ for all cells in panel A, where C_{ij} is the Pearson's correlation coefficient for cells i and j. The overwhelming majority of pairs have low correlation values, suggesting that the overall calcium signaling is asynchronous in the sample. All scale bars = 100 μm.

the dynamics of calcium signaling in HASMs are considerably slower, allowing for high-resolution, large-area monitoring of the responses. In principle, stimulating entire fields of view is possible, however, in order to effect a calcium response the z-position of a given NW and the maximum intensity of the PSF of the illuminating beam must be coincident. Because the micropatterned substrates are not always completely level along, and because the vertical location of NWs can be variable (Figure 3.1B), large-area stimulations functionally only impact a subset of the NWs within a given region. This can still lead to multiple simultaneous stimulations, however (Figure 3.4B), allowing us to examine the development of calcium responses from several originating locations.

Upon a large area stimulation, a sample containing many NWs associated with HASMs displayed a noticeable calcium response (Figure 3.4B). To track the evolution of this response,

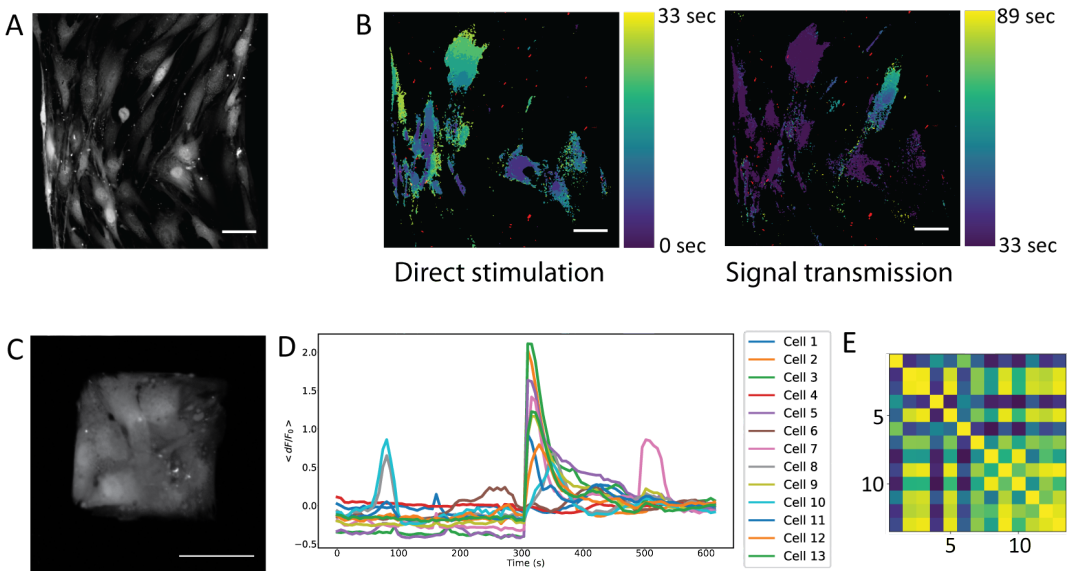

Figure 3.4: Modes of NW-mediated calcium stimulation in large and small HASM colonies. (A) Fluo-8 fluorescence in a large patterned colony. (B) Optical mapping of the colony shown in panel A, of calcium response to NW stimulation separated into two phases. NW locations indicated in red. Initially, NW-associated cells display a rapid calcium response (left). Then, the signal can be transmitted to cells that are not associated with NWs (right). This process is considerably slower than direct stimulation. (C) Fluo-8 fluorescence in a small patterned colony. (D) Average dF/F_0 calcium signal for each cell in the colony shown in panel C. Most cells were stimulated immediately upon illumination, with calcium levels remaining elevated for several seconds before gradually decaying. (E) Post-stimulation correlation matrix for the colony showed in panel C. High levels of correlation suggest that decay patterns were largely similar between cells.

we employed an optical mapping routine that has previously used for monitoring similar processes in cardiac cells [63]. These results indicated that cells with NWs were mostly activated quickly, within the space of 5-10 s, with immediately adjacent cells exhibiting calcium fluxes shortly thereafter (Figure 3.4B, left). This rapid response constitutes the initial phase of cells that are directly stimulated or are immediately adjacent to stimulated cells. Afterwards, in some samples, calcium responses may also transmit from cell to cell to produce an indirect effect (Figure 3.4B, right). This process is significantly slower than the initial response, suggesting that signal transmission occurs through indirect activation, e.g., calcium signaling through gap junctions, rather than the more direct, neurogenic-mimicking stimulation from cells with NWs.

Smaller colonies differ from their larger counterparts in a few significant ways. One is their

evident decreased propensity to oscillate - relative to larger colonies, even densely packed small colonies seldom exhibit calcium fluctuations, and when present the rate seems to be significantly lower. They are, nevertheless, still responsive to NW-mediated stimulation (Figure 3.4D). Since the entire colony can be directly stimulated, the overall response is a rapid increase in calcium levels followed by a more gradual decay. Because calcium signaling events are otherwise infrequent in small colonies, such a spike is a dramatic change in the overall signaling within the colony. While it is tempting to view the decay pattern as an exponential that could be fitted with a characteristic parameter, further investigated revealed that the decay signal is actually more complicated than that, and therefore not amenable to exponential fitting. To verify the uniformity of the decay, however, we were able to construct a correlation matrix for each signal immediately following stimulation (Figure 3.4E). The high correlation values for most cell pairs indicate that most cells followed very similar patterns, with some exceptions for cells that showed a minimal or delayed calcium spike.

3.4.4 Systematic investigation of Ca^{2+} dynamics after NW-mediated stimulation

Based on these results, we set out to determine the effects of NW stimulation on the baseline asynchronous calcium oscillations in tissues. As was observed with small colonies, non-oscillatory cells typically display a strong peak in fluorescence, a gradual decay, and then a return to the steady base level. Some cells in larger colonies are also non-oscillatory, and for these cells, the pattern remains largely the same - a flat line, a large increase, and a return to the original flat line - even when the cell's neighbors are oscillatory (Fig 3.2, lower-right cell/bottommost trace). The presence of oscillations, however, introduces the possibility of more nuanced responses, and so we set out to systematically consider colony-wide effects on synchronization and oscillation frequency, as well as examining single-cell responses after stimulation.

We first examined the possibility of changes in calcium signaling on the scale of entire

colonies, which would imply that the effects of stimulation could transmit significantly further than the comparatively few stimulation sites. Because the unstimulated state is characterized by its asynchronicity, an increase in the overall level of synchronization between cells would suggest that the simultaneous pulses exhibited in stimulated cells may act to "reset" the timing of oscillations in neighboring cells. Such effects were elusive with larger colonies, however (Figure 3.5A). In colonies with NWs, correlation matrices generated from dF/F_0 signals before and after stimulation did not suggest any large-scale coordination, which was consistent with matrices that looked at signals in colonies that were exposed to stimulating light but had no associated NWs (3.5C). Another possible colony-wide impact might be a change in the frequency of oscillations. To measure this, we wrote a spectral analysis routine that plotted the magnitude of the Fourier transforms of signals before and after stimulation against frequency. The frequency corresponding to the highest power was taken to be the predominant oscillation frequency of the cell. We then produced histograms of the predominant frequency for all cells within a colony to visualize any potential changes as a result of stimulation. Once more, there did not appear to be any major impacts on the colony-wide signaling (Figure 3.5B,D). In the stimulated colony, a number of cells beating at higher frequencies appeared to have been attenuated, while the histogram suggests that some low-frequency cells also became slightly quicker (Figure 3.5B). Compared to the no-NW control, however, these results are not dramatic enough to imply significance on the scale of the colony, and in all cases, the histograms are heavily weighted towards low-frequency trends.

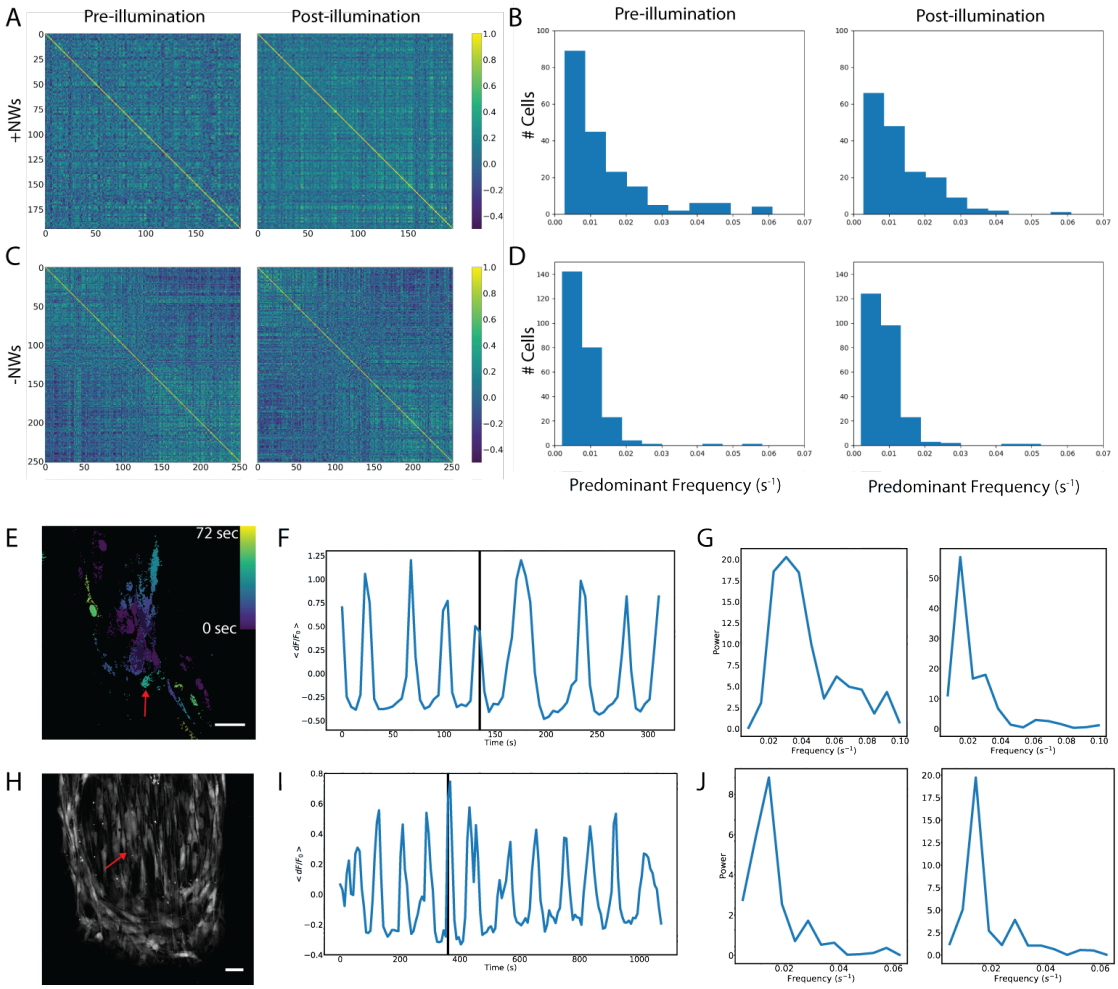

Figure 3.5: Correlation and frequency analyses of calcium signaling after NW-mediated stimulation. (A-D) Localized NW stimulation does not induce large-scale changes. (A) Correlation matrices for a stimulated colony, before (left) and after (right) stimulation. (B) Histograms of highest-power calcium oscillation frequencies for cells within a stimulated colony, before (left) and after (right) stimulation. (C) Correlation matrices for a non-stimulated colony, before (left) and after (right) illumination. (D) Histograms of highest-power calcium oscillation frequencies for cells within a stimulated colony, before (left) and after (right) illumination. (E) Optical mapping of calcium signal after stimulation in an unpatterned colony. Red arrow indicates the location of the cell that is analyzed in the next two panels. (F) Average dF/F_0 signal within a cell adjacent to the stimulated cell. Vertical line indicates the time of stimulation; oscillations remain periodic but adopt a lower frequency after stimulation. (G) Spectral analysis of dF/F_0 signal shown in panel F before (left) and after (right) stimulation. Higher-frequency components are suppressed, and the predominant frequency is lower than before stimulation. (H) Fluo-8 fluorescence of a patterned colony that underwent stimulation. Red arrow indicates a stimulated cell analyzed in the next two panels. (I) Average dF/F_0 signal within a stimulated cell. Vertical line indicates the time of stimulation; oscillations persist largely unchanged after stimulation. (J) Spectral analysis of dF/F_0 signal shown in panel I before (left) and after (right) stimulation, showing the minimal change in frequency. Scale bars = 50 μm.

At the scale of single cells, impacts of stimulation were more evident, namely with respect to cells at or near stimulation sites. Generally, the character of a simple periodic function arises from its amplitude, frequency, and phase. While calcium levels in cells can be somewhat more complicated than this, at times adopting patterns that seem more reminiscent of a superposition of waveforms (Figure 3.6), we observed that most cells could be reasonably approximated with a single frequency and phase, although the amplitude is variable, likely because of a combination of intrinsic variability and the non-ratiometric and therefore non-quantitative nature of fluo-8 as a Ca^{2+} indicator. As such, our investigation of single-cell behavior consisted of the same spectral analysis routines employed at the colony scale, but with particular attention to cells that were local to stimulated regions. At this scale, a recurring motif becomes apparent, of oscillation frequencies decreasing after stimulation (Figure 3.5E-G, also Figure 3.2 traces 1 and 3). A typical dF/F_0 trace of this is presented in Figure 3.5F, where shortly after stimulation, the cell sees a large increase in Ca^{2+} levels, relative to previous oscillations, and afterwards, peaks are spaced somewhat further apart than they were before stimulation (Figure 3.5F). The defining feature of this pattern is a shift in spectral density towards lower frequencies (Figure 3.5G), characterized by a redshift and increase in magnitude of the highest peak, and lower values for higher frequency contributions. This redshift is most frequently observed in cells that are adjacent to stimulated cells, suggesting it is a feature of transmitted calcium signals. Whether it is a response to any large change in calcium or is simply a facet of damage recognition in neighboring cells remains unclear, however. The stimulated cells themselves typically exhibit one of two main patterns. Much like the case for smaller colonies, stimulated cells in large colonies tend to display a large increase in Ca^{2+} and a corresponding decrease, whether the cells were initially oscillatory or not (Figure 3.2, traces 2 and 4). Another observed outcome, however, may arise when the stimulation is coincident with an existing peak in an oscillation (Figure 3.5H-J). In this case, the stimulatory peak is considerably higher than its predecessors, but the overall pattern remains unchanged.

3.5 Discussion

This work presents what is, to our knowledge, the first report of freestanding devices for bioelectronic modulation integrated with airway smooth muscle tissues. As such, we have covered both the fundamental interface formation between SiNWs and HASM cells, as well as the photostimulation capabilities of coaxial p-i-n nanowires. In particular, we found that SiNWs associate with cells without inducing noticeable changes in actin architecture, focal adhesion formation and maturation, or gap junction connectivity. We then validated the use of SiNWs to induce calcium fluxes in small and large HASM colonies. Our key findings in this area were that local stimulation resulted in minimal perturbations to overall colony calcium dynamics and cell-to-cell synchronization thereof, but that cells in the vicinity of stimulation sites had measurable changes in their oscillatory patterns. For cells that were directly stimulated, this commonly took the form of large, transient spikes in Ca^{2+} concentration followed by a decay to the baseline. Cells adjacent to stimulation sites also frequently saw significant spikes, with the additional characteristic of slower oscillations for several minutes after stimulation.

In the course of this analysis, we applied several characterization methods that should prove useful in other studies on bioelectronic modulation in oscillatory systems, such as cardiac cells. The computational routines presented here are suitable for analysis at the scale of single cells up to large colonies and cell monolayers and can help to quickly identify the results of stimulation. Moreover, since SiNWs can be delivered in a drug-like fashion and the only other equipment requirements are a fluorescence microscope and a calcium (or other relevant species) indicator, this routine is completely orthogonal with a wide variety of other techniques of interest, such as FRET sensing, patch clamp microelectrode recording, or optogenetic methods.

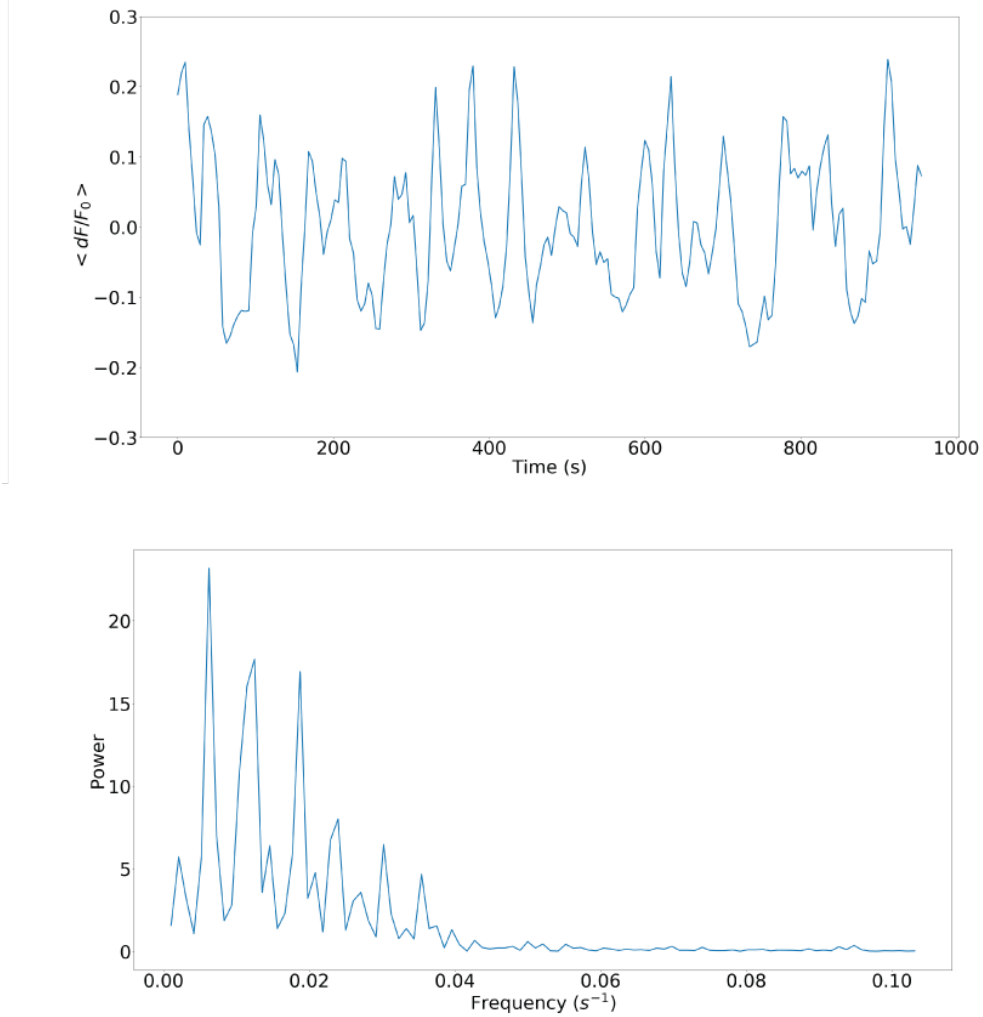

Figure 3.6: Spectral analysis of possible superpositions of wave patterns within the calcium signal of a single cell. (Top) dF/F_0 signal of a cell in an unstimulated colony over the course of 960 s. (Bottom) Spectral analysis indicates contributions from multiple different frequencies.

CHAPTER 4

CONCLUSION

4.1 Summary

My thesis work has primarily fallen into two categories of mechanobiology and bioelectronics, linked by the common theme of treating cells as being more than just biochemical and genetic in nature. By considering cells as physical entities, which can respond to and produce mechanical and electrical stimuli at the cell scale, new perspectives can emerge that complement our present molecular understanding of biology. In Chapter 2, I presented an investigation into how colonies of cells distribute traction stresses, based on an existing hypothesis that the stress distribution patterns would resemble those of single cells. This profile would be characterized by inward force vectors at the colony periphery, localized to regions of curvature. Unexpectedly, it was found that the colonies only fit those patterns under certain conditions - in other instances, the distribution was something in between a collective single cell and a disconnected series of individual cells. Hotspots of stress exertion could appear under the interior of the colony, and they were dynamic: appearing, moving, and dissipating over time. A rationale for the transition between these two modes of distribution arose from a new model. The adherent active vertex model was discussed as a new type of vertex model, one which considered the usual vertex model force balance between cortical contractility and cell-cell adhesion, and added modifications in the form of stochastic motion, focal adhesion turnover, and protrusive dynamics. This model, which was among the first vertex models to make measurable mechanical predictions beyond morphology, was able to explain the different force distribution patterns as arising from differing fluidity of the component cells. The mean velocity of cells was taken as a proxy to this fluidity parameter, and shown to be associated with the presence of dynamic, interior traction stresses. Finally, the model was compared to experimental results with traction stresses at sites of cell division and rotation in circular colonies, and found to agree with the observations. The cell division

results in particular were further validated by subsequent work relating cell divisions within the same cell types to the speed of cells within monolayers, an observation that was itself demonstrated through a vertex model[128].

In Chapter 3, my focus shifted to applications of p-i-n silicon nanowires (SiNWs) in human airway smooth muscle (HASM) tissues. This study began with an examination of the cell-NW interface, which found that there was minimal impacts on the cytoskeletal structure of NW-associated cells. The main analytic machinery was introduced by way of quantifying the asynchronous oscillations in colonies of HASM cells, and verifying that they would display similar oscillatory patterns and frequencies as tissues, even under geometrically confined conditions. The primary tools for showing this were correlation matrices, which indicated that there is little correlation between cells, and spectral analysis to identify the peak frequencies of individual cells within a given colony. The next topic considered was photostimulation of NWs in HASM tissues, distinguishing between large and small colonies. In large colonies, a subset of cells would be stimulated, with effects gradually transmitting outwards from stimulation sites. By contrast, we found that oscillatory behavior in small colonies was initially smaller, and stimulation did little to change that. Rather, it would induce large spikes in intracellular Ca^{2+} concentration, followed by a decay to the baseline. Finally, the effects of stimulation were considered on a whole colony and cell by cell basis in large colonies. Because the extent of stimulation was small relative to the size of the colonies, the impacts on cell-cell correlation as well as average frequency within the whole colony were minor. On the individual cell basis, however, different effects could be observed. Most notably, cells adjacent to stimulation sites were prone to displaying a reduction in oscillation frequency after stimulation.

Both of these projects represent novel contributions to the existing academic corpus. Taken together, they each shed light on different facets of our understanding of how biological cells respond to their environments. In the first case, a central result was the importance of cell-cell interactions in determining the final force distribution to the local environment. If

a cell's neighbors were in motion, the cell itself was likely to also be in motion, resembling a fluid rather than a jammed solid, and the forces that were exerted reflected that dynamic nature. In the second case, the stimulation was external, provided selectively by way of photostimulation on nanowires that spontaneously formed interfaces with cultured cells. The observation of lower frequency oscillations near stimulated cells provides clues as to future applications and side effects of nanowire technology.

4.2 Future directions

Given that the research presented here draws heavily from mechanical and electrical considerations in cell biology, a question very naturally emerges: What is the overlap between these two areas of research? To date, much work has been conducted to link mechanical processes with molecular signaling, and a robust body of literature also exists to link cell and tissue level electrical processes with molecular biology. Surprisingly, these two areas of research even have some elements in common, namely the RhoA signaling pathway, which is a major regulator of myosin contractility, and which also plays a role in excitation-contraction coupling. Based on this relationship, it may be hypothesized that there is indeed crosstalk between cell mechanics and bioelectronics. Alas, research explicitly linking these two distinct areas is comparatively sparse in the literature.

What explains this discrepancy? To be sure, the connection to RhoA is somewhat more tenuous with electrical processes than with mechanical ones, as RhoA itself does not appear to be regulated by electrical stimuli, but other components of the pathway, namely myosin light chain kinase (MLCK), are more directly related. MLCK is both downstream of RhoA activity, and it is promoted by high intracellular calcium concentrations. Both RhoA activity and elevated calcium act to increase MLCK[129], and given how closely that is regulated, it is not entirely surprising that there is evidence of explicit links between the two pathways[130][131]. MLCK is not the only direction to pursue in consideration of this overlap, either. In the last ten years, the Piezo family of channel proteins has emerged as an

increasingly important target of inquiry[132]. It is mechanically responsive - stretching activates it[133] - but it has also been recently announced to operate in a purely voltage-sensing mode as well[134], in that its probability of being open increases at positive voltages. Some recent reports have explicitly considered electromechanical coupling in cells through Piezo channels[135][136], and have even connected Piezo-mediated calcium signaling to traction forces[137]. Optogenetic methods, which were originally introduced in the context of ion channel regulation, have been employed to help elucidate the nature of electrical signaling in cells[39], and have recently also been successfully applied in mechanical contexts[138][139]. To rigorously explore the relationships between bioelectronics and cell mechanics, however, the length scales of the two fields must converge, which implies that bioelectronic devices need to be able to operate and interact at the subcellular level. Chapter 3 of this dissertation comprises an early exploration of bioelectronics at this scale, but it is likely that future developments in nanoscale devices and computational modeling will help to clarify this intersection.

Another recurring theme in all of my areas of interest, and one which will no doubt become increasingly important in the foreseeable future, is the role of computational routines throughout the scientific process. The work presented here all relies on computers, whether they are being applied to quickly handle discrete data in the form of images, or to acquire those images in the first place. For instance, a major motivation for the research that forms Chapter 2 was to examine the experimental relevance of active vertex models, a class of models that had seen large amounts of interest, but which had been mostly confined to the theoretical domain[140]. This sort of dialectic between experiment and theory is likely to proceed with heavy input from the computational domain. One way this might happen is through the increasing relegation of pattern recognition duties to machine learning algorithms, particularly convolutional neural networks, which are ideally suited to detect subtle relationships that may not be immediately obvious to the human eye[141][142]. Increasing capabilities for modeling and simulation are likely to make major contributions, as

well[143][144]. Vast libraries of simulations for pharmacological interactions and material properties have both been applied to identify promising candidates for further investigation[145][146]. Our understanding of cell mechanics as well as bioelectronics are likely to deepen as a result of similar developments in these spaces[147].

APPENDIX A

STANDARD METHODS AND MATERIALS

A.1 Cleaning and activation of glass coverslips

Flexible or micropatterned substrates must use glass that has been silanized and treated with glutaraldehyde in order for the gel to adhere to the glass. This is the standard protocol used for this process, as well as the requisite cleaning beforehand, referred to elsewhere as coverslip "activation."

A.1.1 "Squeekie cleaning" for coverslips

Eliminate as many bubbles as possible in every step.

1. Place new coverslips into a beaker of tap water, sonicate for 30 minutes.
2. Exchange solution to dilute versa-clean in DI water, sonicate for 30 minutes.
3. Exchange solution to DI water, sonicate for 30 minutes.
4. Exchange solution for 30% ethanol, sonicate 30 minutes.
5. Exchange solution for 70% ethanol, sonicate 30 minutes.
6. Exchange solution for 100% ethanol, sonicate 30 minutes.
7. Exchange solution with fresh 100% ethanol, sonicate 30 minutes.
8. Pour out 100% ethanol and place coverslips in a jar with 100% ethanol for storage.

A.1.2 Activating coverslip surface

1. Place squeaky clean coverslips in stainless steel rack. Flame coverslips individually to get rid of the ethanol.

2. Immerse in 2% 3-(aminopropyl)trimethyoxysilane diluted in isopropanol for 10 minutes. 3-(aminopropyl)triethoxysilane should also function to serve the same purpose.

3. Dispose of the waste in a container dedicated to coverslip activation waste. Rinse converslips in DI water 3-4 times.

4. Dry coverslips at low temperature in incubator.

5. Immerse in 1% gluteraldehyde solution in H2O for 30 minutes. Dispose of waste in dedicated container.

6. Wash in DI water for 10 minutes, exchange solution and repeat 2 times.

7. Dry in incubator.

8. Store at room temperature in a petri dish or covered by aluminum foil to prevent dust from adhering to the surface.

A.2 PAA Micropatterning

This is a condensed protocol of the micropatterning technique described in further detail in Section 4.1 of Chapter 1. These steps are adapted from a protocol written by Patrick W. Oakes in 2013.

1. Prepare PAA gel mixture with standard solution, water, beads (if using).

2. Clean Cr side of photomask with DI water (approx. 0.5 - 1 mL) first, then with approx. 0.5 - 1 mL hexane. Apply uniform pressure and avoid streaking.

3. Add TEMED and APS to gel solution and pipette up and down to mix.

4. Add a drop of the gel mixture to the center of the pattern on the chrome side of the photomask. Heuristically, 11 - 15 μL is appropriate for a 25 mm round slide Volume can be scaled appropriately to the size of the coverslip.

5. Gently lower coverslip onto spot, avoiding touching the mask with tweezers.

6. Cover lightly with foil. Let polymerize 30 min. The gel should retract at the edges of the coverslip and the leftover gel mixture should be fully polymerized in the tube.

7. Put mask with polymerized gels into UV oven, quartz side up, edges resting on spacers (slides). Set oven for 90 s, then let rest an additional 5 min to let ozone clear.

8. Make 1 mL aqueous solutions of 1 aliquot EDC (8 - 12 mg, stored in a -20° freezer) and NHS (approx. 15 - 20 mg, stored at room temp). Vortex.

9. Mix EDC and NHS solutions 1:1.

10. Spot 250 μL EDC-NHS onto parafilm on cardboard for each coverslip.

11. Submerge mask inside a glass dish filled with DI water. Use a new razor blade to lift edge of slide and tweezers to grab. Keep razor blade flat, avoid touching mask with tweezers, and avoid getting anything close to the pattern.

12. Gently wick away extra moisture by touching the edge of the coverslip to a kimwipe (avoid touching the gel to anything). Place gel-side down onto EDC-NHS. Let rest 10 min. You should see small bubbles forming indicating the reaction is taking place.

13. Carefully dry mask, making sure to remove any leftover gel and water before storing. Any remnant gel stuck to the mask can be removed using just DI water.

14. Prepare a 10 $\mu g/mL$ solution of your protein of interest in HEPES (pH 8.5). Spot 100 μL per slide onto another piece of parafilm.

15. Remove coverslips from EDC-NHS and wick away excess liquid, then invert coverslip gel-side down on protein solution. Let rest 15 - 30 min.

16. Set coverslip in a dish gel-side up. Wash 3x with PBS, with 5 min between washes.

17. Store in cold PBS.

BIBLIOGRAPHY

[1] Philip W. Anderson. "More Is Different". In: *Science* 177.4047 (Aug. 4, 1972). Publisher: American Association for the Advancement of Science Section: Articles, pp. 393–396. DOI: 10.1126/science.177.4047.393.

[2] Rosalind E. Franklin and Raymond G. Gosling. "Molecular Configuration in Sodium Thymonucleate". In: *Nature* 171.4356 (1953), pp. 740–741.

[3] Kyle H. Vining and David J. Mooney. "Mechanical forces direct stem cell behaviour in development and regeneration". In: *Nature Reviews Molecular Cell Biology* 18.12 (Dec. 2017). Number: 12 Publisher: Nature Publishing Group, pp. 728–742. DOI: 10.1038/nrm.2017.108.

[4] Jeroen Eyckmans et al. "A Hitchhiker's Guide to Mechanobiology". In: *Developmental cell* 21.1 (July 19, 2011), pp. 35–47. DOI: 10.1016/j.devcel.2011.06.015.

[5] Yanhang Zhang, Jiangyu Li, and Gregory S. Boutis. "The Coupled Bio-Chemo-Electro-Mechanical Behavior of Glucose Exposed Arterial Elastin". In: *Journal of physics D: Applied physics* 50 (2017). DOI: 10.1088/1361-6463/aa5c55.

[6] Yihong Chen et al. "Physiological electric field works via the VEGF receptor to stimulate neovessel formation of vascular endothelial cells in a 3D environment". In: *Biology Open* 7.9 (Sept. 15, 2018). Publisher: The Company of Biologists Ltd Section: Research Article. DOI: 10.1242/bio.035204.

[7] Thomas D. Pollard. "Actin and Actin-Binding Proteins". In: *Cold Spring Harbor Perspectives in Biology* 8.8 (Aug. 1, 2016). Company: Cold Spring Harbor Laboratory Press Distributor: Cold Spring Harbor Laboratory Press Institution: Cold Spring Harbor Laboratory Press Label: Cold Spring Harbor Laboratory Press Publisher: Cold Spring Harbor Lab, a018226. DOI: 10.1101/cshperspect.a018226.

[8] Tatyana Svitkina. "The Actin Cytoskeleton and Actin-Based Motility". In: *Cold Spring Harbor Perspectives in Biology* 10.1 (Jan. 2018), a018267. DOI: 10.1101/cshperspect.a018267.

[9] Patrick W. Oakes et al. "Tension is required but not sufficient for focal adhesion maturation without a stress fiber template". In: *The Journal of Cell Biology* 196.3 (Feb. 6, 2012), pp. 363–374. DOI: 10.1083/jcb.201107042.

[10] Pirta Hotulainen and Pekka Lappalainen. "Stress fibers are generated by two distinct actin assembly mechanisms in motile cells". In: *Journal of Cell Biology* 173.3 (May 8, 2006). Publisher: The Rockefeller University Press, pp. 383–394. DOI: 10.1083/jcb.200511093.

[11] Adar Sonn-Segev, Anne Bernheim-Groswasser, and Yael Roichman. "Dynamics in steady statein vitroacto-myosin networks". In: *Journal of Physics: Condensed Matter* 29.16 (Mar. 2017). Publisher: IOP Publishing, p. 163002. DOI: 10.1088/1361-648X/aa62ca.

[12] Alex Mogilner and George Oster. "Force Generation by Actin Polymerization II: The Elastic Ratchet and Tethered Filaments". In: *Biophysical Journal* 84.3 (), pp. 1591–1605. DOI: 10.1016/S0006-3495(03)74969-8.

[13] Campbell D. Lawson and Anne J. Ridley. "Rho GTPase signaling complexes in cell migration and invasion". In: *Journal of Cell Biology* 217.2 (Feb. 5, 2018). Publisher: The Rockefeller University Press, pp. 447–457. DOI: 10.1083/jcb.201612069.

[14] Shuh Narumiya and Dean Thumkeo. "Rho signaling research: history, current status and future directions". In: *FEBS Letters* 592.11 (2018), pp. 1763–1776. DOI: 10.1002/1873-3468.13087.

[15] Richard G. Hodge and Anne J. Ridley. "Regulating Rho GTPases and their regulators". In: *Nature Reviews Molecular Cell Biology* 17.8 (Aug. 2016). Number: 8 Publisher: Nature Publishing Group, pp. 496–510. DOI: 10.1038/nrm.2016.67.

[16] Elena Kassianidou, Jasmine H. Hughes, and Sanjay Kumar. "Activation of ROCK and MLCK tunes regional stress fiber formation and mechanics via preferential myosin light chain phosphorylation". In: *Molecular Biology of the Cell* 28.26 (Oct. 18, 2017). Publisher: American Society for Cell Biology (mboc), pp. 3832–3843. DOI: 10.1091/mbc.e17-06-0401.

[17] Fabiana Martino et al. "Cellular Mechanotransduction: From Tension to Function". In: *Frontiers in Physiology* 9 (), p. 824. DOI: 10.3389/fphys.2018.00824.

[18] Venkat Maruthamuthu, Yvonne Aratyn-Schaus, and Margaret L. Gardel. "Conserved F-actin dynamics and force transmission at cell adhesions". In: *Current Opinion in Cell Biology* 22.5 (Oct. 2010), pp. 583–588. DOI: 10.1016/j.ceb.2010.07.010.

[19] Pakorn Kanchanawong et al. "Nanoscale architecture of integrin-based cell adhesions". In: *Nature* 468.7323 (Nov. 2010). Number: 7323 Publisher: Nature Publishing Group, pp. 580–584. DOI: 10.1038/nature09621.

[20] Patrick W Oakes and Margaret L Gardel. "Stressing the limits of focal adhesion mechanosensitivity". In: *Current Opinion in Cell Biology* 30 (), pp. 68–73. DOI: 10.1016/j.ceb.2014.06.003.

[21] Joshua A. Broussard, Donna J. Webb, and Irina Kaverina. "Asymmetric focal adhesion disassembly in motile cells". In: *Current Opinion in Cell Biology* 20.1 (Feb. 2008), pp. 85–90. DOI: 10.1016/j.ceb.2007.10.009.

[22] Paul A. Janmey, Daniel A. Fletcher, and Cynthia A. Reinhart-King. "Stiffness Sensing by Cells". In: *Physiological Reviews* 100.2 (Nov. 21, 2019). Publisher: American Physiological Society, pp. 695–724. ISSN: 0031-9333. DOI: 10.1152/physrev.00013.2019. (Visited on 03/31/2020).

[23] Nicolas Borghi et al. "E-cadherin is under constitutive actomyosin-generated tension that is increased at cell–cell contacts upon externally applied stretch". In: *Proceedings of the National Academy of Sciences* 109.31 (July 31, 2012). Publisher: National

Academy of Sciences Section: Biological Sciences, pp. 12568–12573. DOI: 10.1073/pnas.1204390109.

[24] Aaron F. Mertz et al. "Cadherin-based intercellular adhesions organize epithelial cell-matrix traction forces". In: *Proceedings of the National Academy of Sciences of the United States of America* 110.3 (Jan. 15, 2013), pp. 842–847. DOI: 10.1073/pnas.1217279110.

[25] K. A. Knudsen et al. "Interaction of alpha-actinin with the cadherin/catenin cell-cell adhesion complex via alpha-catenin." In: *Journal of Cell Biology* 130.1 (July 1, 1995). Publisher: The Rockefeller University Press, pp. 67–77. DOI: 10.1083/jcb.130.1.67.

[26] Zhijun Liu et al. "Mechanical tugging force regulates the size of cell–cell junctions". In: *Proceedings of the National Academy of Sciences* 107.22 (June 1, 2010). Publisher: National Academy of Sciences Section: Physical Sciences, pp. 9944–9949. DOI: 10.1073/pnas.0914547107.

[27] Catherine Kirkpatrick and Mark Peifer. "Not just glue: cell-cell junctions as cellular signaling centers". In: *Current Opinion in Genetics & Development* 5.1 (Feb. 1, 1995), pp. 56–65. DOI: 10.1016/S0959-437X(95)90054-3.

[28] Teresa T. Bonello et al. "Rap1 acts via multiple mechanisms to position Canoe and adherens junctions and mediate apical-basal polarity establishment". In: *Development* 145.2 (Jan. 15, 2018). Publisher: Oxford University Press for The Company of Biologists Limited Section: RESEARCH ARTICLE. DOI: 10.1242/dev.157941.

[29] Alan S. Fanning, Christina M. Van Itallie, and James M. Anderson. "Zonula occludens-1 and -2 regulate apical cell structure and the zonula adherens cytoskeleton in polarized epithelia". In: *Molecular Biology of the Cell* 23.4 (Dec. 21, 2011). Publisher: American Society for Cell Biology (mboc), pp. 577–590. DOI: 10.1091/mbc.e11-09-0791.

[30] Wangsun Choi et al. “Remodeling the zonula adherens in response to tension and the role of afadin in this response”. In: *Journal of Cell Biology* 213.2 (Apr. 25, 2016). Publisher: The Rockefeller University Press, pp. 243–260. DOI: 10.1083/jcb.201506115.

[31] Youngbin Cho et al. “Electric field–induced migration and intercellular stress alignment in a collective epithelial monolayer”. In: *Molecular Biology of the Cell* 29.19 (). Ed. by Yu-Li Wang, pp. 2292–2302. DOI: 10.1091/mbc.E18-01-0077.

[32] Greg M. Allen, Alex Mogilner, and Julie A. Theriot. “Electrophoresis of Cellular Membrane Components Creates the Directional Cue Guiding Keratocyte Galvanotaxis”. In: *Current Biology* 23.7 (Apr. 8, 2013). Publisher: Elsevier, pp. 560–568. DOI: 10.1016/j.cub.2013.02.047.

[33] Sreeja B. Asokan et al. “Two-Dimensional Manipulation and Orientation of Actin−Myosin Systems with Dielectrophoresis”. In: *Nano Letters* 3.4 (Apr. 1, 2003). Publisher: American Chemical Society, pp. 431–437. ISSN: 1530-6984. DOI: 10.1021/nl0259434.

[34] Min Zhao et al. “Electrical signals control wound healing through phosphatidylinositol-3-OH kinase-gamma and PTEN”. In: *Nature* 442.7101 (July 27, 2006), pp. 457–460. DOI: 10.1038/nature04925.

[35] Min Zhao et al. “Electrical stimulation directly induces pre-angiogenic responses in vascular endothelial cells by signaling through VEGF receptors”. In: *Journal of Cell Science* 117 (Jan. 26, 2004), pp. 397–405. DOI: 10.1242/jcs.00868.

[36] Krzysztof Krawczyk et al. “Electrogenetic cellular insulin release for real-time glycemic control in type 1 diabetic mice”. In: *Science* 368.6494 (May 29, 2020). Publisher: American Association for the Advancement of Science Section: Research Article, pp. 993–1001. DOI: 10.1126/science.aau7187.

[37] David E. Clapham. “Calcium Signaling”. In: *Cell* 131.6 (Dec. 2007), pp. 1047–1058. DOI: 10.1016/j.cell.2007.11.028.

[38] William A. Catterall. "Voltage-Gated Calcium Channels". In: *Cold Spring Harbor Perspectives in Biology* 3.8 (Aug. 2011). DOI: 10.1101/cshperspect.a003947.

[39] Jin Man Kim et al. "Optogenetic toolkit reveals the role of Ca $^{2+}$ sparklets in coordinated cell migration". In: *Proceedings of the National Academy of Sciences* 113.21 (May 24, 2016), pp. 5952–5957. DOI: 10.1073/pnas.1518412113.

[40] Yassine Amrani and Reynold A. Panettieri. "Airway smooth muscle: contraction and beyond". In: *The International Journal of Biochemistry & Cell Biology* 35.3 (Mar. 2003), pp. 272–276. DOI: 10.1016/s1357-2725(02)00259-5.

[41] Jacquelyn E. Van Lierop et al. "Activation of Smooth Muscle Myosin Light Chain Kinase by Calmodulin ROLE OF LYS30 and GLY40". In: *Journal of Biological Chemistry* 277.8 (Feb. 22, 2002). Publisher: American Society for Biochemistry and Molecular Biology, pp. 6550–6558. DOI: 10.1074/jbc.M111404200.

[42] Arhat Abzhanov et al. "The calmodulin pathway and evolution of elongated beak morphology in Darwin's finches". In: *Nature* 442.7102 (). Number: 7102 Publisher: Nature Publishing Group, pp. 563–567. DOI: 10.1038/nature04843. (Visited on 06/02/2020).

[43] A Tripathy et al. "Calmodulin activation and inhibition of skeletal muscle Ca2+ release channel (ryanodine receptor)." In: *Biophysical Journal* 69.1 (July 1995), pp. 106–119.

[44] James P. Butler et al. "Traction fields, moments, and strain energy that cells exert on their surroundings". In: *American Journal of Physiology. Cell Physiology* 282.3 (Mar. 2002), pp. C595–605. DOI: 10.1152/ajpcell.00270.2001.

[45] Benedikt Sabass et al. "High Resolution Traction Force Microscopy Based on Experimental and Computational Advances". In: *Biophysical Journal* 94.1 (Jan. 1, 2008), pp. 207–220. DOI: 10.1529/biophysj.107.113670.

[46] Erik N. Schaumann and Bozhi Tian. "Biological Interfaces, Modulation, and Sensing with Inorganic Nano-Bioelectronic Materials". In: *Small Methods* (Mar. 8, 2020), p. 1900868. ISSN: 2366-9608, 2366-9608. DOI: 10.1002/smtd.201900868. (Visited on 03/23/2020).

[47] Yuanwen Jiang et al. "Rational design of silicon structures for optically controlled multiscale biointerfaces". In: *Nature Biomedical Engineering* 2.7 (July 2018). Number: 7 Publisher: Nature Publishing Group, pp. 508–521. DOI: 10.1038/s41551-018-0230-1.

[48] Shuo Chen et al. "Near-infrared deep brain stimulation via upconversion nanoparticle–mediated optogenetics". In: *Science* 359 (2018), pp. 679–684. DOI: 10.1126/science.aaq1144.

[49] Ramya Parameswaran et al. "Optical stimulation of cardiac cells with a polymer-supported silicon nanowire matrix". In: *Proceedings of the National Academy of Sciences* 116.2 (), pp. 413–421. DOI: 10.1073/pnas.1816428115.

[50] John F. Zimmerman et al. "Cellular uptake and dynamics of unlabeled freestanding silicon nanowires". In: *Science Advances* 2.12 (Dec. 1, 2016), e1601039. DOI: 10.1126/sciadv.1601039.

[51] Yin Fang et al. "Texturing Silicon Nanowires for Highly Localized Optical Modulation of Cellular Dynamics". In: *Nano Letters* 18.7 (July 11, 2018). Publisher: American Chemical Society, pp. 4487–4492. DOI: 10.1021/acs.nanolett.8b01626.

[52] João L. Carvalho-de-Souza et al. "Optocapacitive Generation of Action Potentials by Microsecond Laser Pulses of Nanojoule Energy". In: *Biophysical Journal* 114.2 (Jan. 23, 2018), pp. 283–288. DOI: 10.1016/j.bpj.2017.11.018.

[53] Ramya Parameswaran et al. "Photoelectrochemical modulation of neuronal activity with free-standing coaxial silicon nanowires". In: *Nature nanotechnology* 13.3 (Mar. 2018), pp. 260–266. DOI: 10.1038/s41565-017-0041-7.

[54] Simon Haziza et al. “Fluorescent nanodiamond tracking reveals intraneuronal transport abnormalities induced by brain-disease-related genetic risk factors”. In: *Nature Nanotechnology* 12.4 (2017), pp. 322–328. DOI: 10.1038/nnano.2016.260.

[55] J.F. Suyver et al. “Novel materials doped with trivalent lanthanides and transition metal ions showing near-infrared to visible photon upconversion”. In: *Optical Materials* 27.6 (Mar. 2005), pp. 1111–1130. DOI: 10.1016/j.optmat.2004.10.021.

[56] Yuanwen Jiang and Bozhi Tian. “Inorganic semiconductor biointerfaces”. In: *Nature reviews. Materials* 3.12 (Dec. 2018), pp. 473–490. DOI: 10.1038/s41578-018-0062-3.

[57] Yinan Shu et al. “Understanding Nonradiative Recombination through Defect-Induced Conical Intersections”. In: *The Journal of Physical Chemistry Letters* 8.17 (Sept. 7, 2017). Publisher: American Chemical Society, pp. 4091–4099. DOI: 10.1021/acs.jpclett.7b01707.

[58] Adrian N. Holm et al. “Whole cell current and membrane potential regulation by a human smooth muscle mechanosensitive calcium channel”. In: *American Journal of Physiology-Gastrointestinal and Liver Physiology* 279.6 (Dec. 1, 2000). Publisher: American Physiological Society, G1155–G1161. DOI: 10.1152/ajpgi.2000.279.6.G1155.

[59] Jeanne M. Nerbonne and Robert S. Kass. “Molecular physiology of cardiac repolarization”. In: *Physiological Reviews* 85.4 (Oct. 2005), pp. 1205–1253. DOI: 10.1152/physrev.00002.2005.

[60] Jon F. Edd, Liana Horowitz, and Boris Rubinsky. “Temperature dependence of tissue impedivity in electrical impedance tomography of cryosurgery”. In: *IEEE transactions on biomedical engineering* 52.4 (Apr. 2005), pp. 695–701. DOI: 10.1109/TBME.2005.844042.

[61] Mikhail G. Shapiro et al. "Infrared light excites cells by changing their electrical capacitance". In: *Nature Communications* 3.1 (Mar. 13, 2012). Number: 1 Publisher: Nature Publishing Group, p. 736. DOI: 10.1038/ncomms1742.

[62] Yuanwen Jiang et al. "Heterogeneous silicon mesostructures for lipid-supported bioelectric interfaces". In: *Nature Materials* 15.9 (Sept. 2016). Number: 9 Publisher: Nature Publishing Group, pp. 1023–1030. DOI: 10.1038/nmat4673. (Visited on 05/25/2020).

[63] Menahem Y. Rotenberg et al. "Living myofibroblast–silicon composites for probing electrical coupling in cardiac systems". In: *Proceedings of the National Academy of Sciences* 116.45 (), pp. 22531–22539. DOI: 10.1073/pnas.1913651116.

[64] Stanley Nattel. "Electrical coupling between cardiomyocytes and fibroblasts: experimental testing of a challenging and important concept". In: *Cardiovascular Research* 114.3 (Mar. 1, 2018). Publisher: Oxford Academic, pp. 349–352. DOI: 10.1093/cvr/cvy003.

[65] T. Alexander Quinn et al. "Electrotonic coupling of excitable and nonexcitable cells in the heart revealed by optogenetics". In: *Proceedings of the National Academy of Sciences* 113.51 (Dec. 20, 2016). Publisher: National Academy of Sciences Section: Biological Sciences, pp. 14852–14857. DOI: 10.1073/pnas.1611184114.

[66] Rohit Manchanda, Shailesh Appukuttan, and Mithun Padmakumar. "Electrophysiology of Syncytial Smooth Muscle". In: *Journal of Experimental Neuroscience* 13 (Jan. 17, 2019). DOI: 10.1177/1179069518821917.

[67] Shiladitya Banerjee and M. Cristina Marchetti. "Contractile Stresses in Cohesive Cell Layers on Finite-Thickness Substrates". In: *Physical Review Letters* 109.10 (Sept. 4, 2012). Publisher: American Physical Society, p. 108101. DOI: 10.1103/PhysRevLett.109.108101.

[68] Aaron F. Mertz et al. “Scaling of Traction Forces with the Size of Cohesive Cell Colonies”. In: *Physical review letters* 108.19 (May 11, 2012), p. 198101.

[69] Patrick W. Oakes et al. “Geometry Regulates Traction Stresses in Adherent Cells”. In: *Biophysical Journal* 107.4 (), pp. 825–833. DOI: 10.1016/j.bpj.2014.06.045.

[70] Qingzong Tseng et al. “A new micropatterning method of soft substrates reveals that different tumorigenic signals can promote or reduce cell contraction levels”. In: *Lab on a Chip* 11.13 (July 7, 2011), pp. 2231–2240. DOI: 10.1039/c0lc00641f.

[71] Franco Cataldo, Ornella Ursini, and Giancarlo Angelini. “Surface oxidation of rubber crumb with ozone”. In: *Polymer Degradation and Stability* 95.5 (May 1, 2010), pp. 803–810. DOI: 10.1016/j.polymdegradstab.2010.02.003.

[72] Hideji Ichijima et al. “Surface modification of poly(methyl methacrylate) by graft copolymerization”. In: *Die Makromolekulare Chemie* 192.5 (1991), pp. 1213–1221. DOI: 10.1002/macp.1991.021920520.

[73] R. O. F. Verkuijlen et al. “Surface modification of polycarbonate and polyethylene naphtalate foils by UV-ozone treatment and μPlasma printing”. In: *Applied Surface Science* 290 (Jan. 30, 2014), pp. 381–387. DOI: 10.1016/j.apsusc.2013.11.089.

[74] Erik N. Schaumann et al. “Force localization modes in dynamic epithelial colonies”. In: *Molecular Biology of the Cell* 29.23 (Nov. 15, 2018). Ed. by Leah Edelstein-Keshet, pp. 2835–2847. DOI: 10.1091/mbc.E18-05-0336.

[75] Jennifer A. Zallen. “Planar polarity and tissue morphogenesis”. In: *Cell* 129.6 (June 15, 2007), pp. 1051–1063. DOI: 10.1016/j.cell.2007.05.050.

[76] Victor D. Varner and Celeste M. Nelson. “Cellular and physical mechanisms of branching morphogenesis”. In: *Development* 141.14 (July 15, 2014). Publisher: Oxford University Press for The Company of Biologists Limited Section: REVIEW, pp. 2750–2759. DOI: 10.1242/dev.104794.

[77] Agustí Brugués et al. “Forces driving epithelial wound healing”. In: *Nature Physics* 10.9 (), pp. 683–690. DOI: 10.1038/nphys3040.

[78] Peter Friedl and Darren Gilmour. “Collective cell migration in morphogenesis, regeneration and cancer”. In: *Nature Reviews Molecular Cell Biology* 10.7 (July 2009). Number: 7 Publisher: Nature Publishing Group, pp. 445–457. DOI: 10.1038/nrm2720.

[79] Benoit Ladoux and René-Marc Mège. “Mechanobiology of collective cell behaviours”. In: *Nature Reviews Molecular Cell Biology* 18.12 (Dec. 2017). Number: 12 Publisher: Nature Publishing Group, pp. 743–757. DOI: 10.1038/nrm.2017.98.

[80] Johan de Rooij et al. “Integrin-dependent actomyosin contraction regulates epithelial cell scattering”. In: *The Journal of Cell Biology* 171.1 (Oct. 10, 2005), pp. 153–164. DOI: 10.1083/jcb.200506152.

[81] Jones Tsai and Lance Kam. “Rigidity-Dependent Cross Talk between Integrin and Cadherin Signaling”. In: *Biophysical Journal* 96.6 (Mar. 18, 2009), pp. L39–L41. DOI: 10.1016/j.bpj.2009.01.005.

[82] Venkat Maruthamuthu et al. “Cell-ECM traction force modulates endogenous tension at cell-cell contacts”. In: *Proceedings of the National Academy of Sciences of the United States of America* 108.12 (Mar. 22, 2011), pp. 4708–4713. DOI: 10.1073/pnas.1011123108.

[83] Dhananjay T. Tambe et al. “Collective cell guidance by cooperative intercellular forces”. In: *Nature Materials* 10.6 (June 2011). Number: 6 Publisher: Nature Publishing Group, pp. 469–475. DOI: 10.1038/nmat3025.

[84] Reza Farhadifar et al. “The influence of cell mechanics, cell-cell interactions, and proliferation on epithelial packing”. In: *Current biology: CB* 17.24 (Dec. 18, 2007), pp. 2095–2104. DOI: 10.1016/j.cub.2007.11.049.

[85] Dapeng Bi et al. “A density-independent rigidity transition in biological tissues”. In: *Nature Physics* 11.12 (Dec. 2015), pp. 1074–1079. DOI: 10.1038/nphys3471.

[86] Carina M. Edwards and Ulrich S. Schwarz. "Force Localization in Contracting Cell Layers". In: *Physical Review Letters* 107.12 (Sept. 15, 2011). Publisher: American Physical Society, p. 128101. DOI: 10.1103/PhysRevLett.107.128101.

[87] Hisao Honda and Goro Eguchi. "How much does the cell boundary contract in a monolayered cell sheet?" In: *Journal of Theoretical Biology* 84.3 (June 7, 1980), pp. 575–588. DOI: 10.1016/S0022-5193(80)80021-X.

[88] Alexander G. Fletcher et al. "Vertex models of epithelial morphogenesis". In: *Biophysical Journal* 106.11 (June 3, 2014), pp. 2291–2304. DOI: 10.1016/j.bpj.2013.11.4498.

[89] Daniel L. Barton et al. "Active Vertex Model for cell-resolution description of epithelial tissue mechanics". In: *PLOS Computational Biology* 13.6 (June 30, 2017). Publisher: Public Library of Science, e1005569. DOI: 10.1371/journal.pcbi.1005569.

[90] Francois Graner and James Glazier. "Simulation of biological cell sorting using a two-dimensional extended Potts model". In: *Physical Review Letters* 69.13 (Sept. 28, 1992), pp. 2013–2016. DOI: 10.1103/PhysRevLett.69.2013.

[91] Philipp J. Albert and Ulrich S. Schwarz. "Dynamics of Cell Ensembles on Adhesive Micropatterns: Bridging the Gap between Single Cell Spreading and Collective Cell Migration". In: *PLoS computational biology* 12.4 (Apr. 2016), e1004863. DOI: 10.1371/journal.pcbi.1004863.

[92] Dapeng Bi et al. "Motility-Driven Glass and Jamming Transitions in Biological Tissues". In: *Physical Review X* 6.2 (Apr. 21, 2016). Publisher: American Physical Society, p. 021011. DOI: 10.1103/PhysRevX.6.021011.

[93] Hirokazu Tanimoto and Masaki Sano. "Dynamics of traction stress field during cell division". In: *Physical Review Letters* 109.24 (Dec. 14, 2012), p. 248110. DOI: 10.1103/PhysRevLett.109.248110.

[94] Kandice Tanner et al. “Coherent angular motion in the establishment of multicellular architecture of glandular tissues”. In: *Proceedings of the National Academy of Sciences* 109.6 (Feb. 7, 2012). Publisher: National Academy of Sciences Section: Biological Sciences, pp. 1973–1978. DOI: 10.1073/pnas.1119578109.

[95] Kevin Doxzen et al. “Guidance of collective cell migration by substrate geometry”. In: *Integrative Biology: Quantitative Biosciences from Nano to Macro* 5.8 (Aug. 2013), pp. 1026–1035. DOI: 10.1039/c3ib40054a.

[96] M. Deforet et al. “Emergence of collective modes and tri-dimensional structures from epithelial confinement”. In: *Nature Communications* 5.1 (May 6, 2014). Number: 1 Publisher: Nature Publishing Group, p. 3747. DOI: 10.1038/ncomms4747.

[97] Jacob Notbohm et al. “Cellular Contraction and Polarization Drive Collective Cellular Motion”. In: *Biophysical Journal* 110.12 (June 21, 2016), pp. 2729–2738. DOI: 10.1016/j.bpj.2016.05.019.

[98] Alexei Verkhratsky, O. A. Krishtal, and Ole H. Petersen. “From Galvani to patch clamp: the development of electrophysiology”. In: *Pflügers Archiv* 453.3 (Dec. 1, 2006), pp. 233–247. DOI: 10.1007/s00424-006-0169-z.

[99] Christof J Schwiening. “A brief historical perspective: Hodgkin and Huxley”. In: *The Journal of Physiology* 590 (Pt 11 June 1, 2012), pp. 2571–2575. DOI: 10.1113/jphysiol.2012.230458.

[100] A. L. Hodgkin and A. F. Huxley. “A quantitative description of membrane current and its application to conduction and excitation in nerve”. In: *The Journal of Physiology* 117.4 (Aug. 28, 1952), pp. 500–544.

[101] Alexander M. Xu et al. “Temporally resolved direct delivery of second messengers into cells using nanostraws”. In: *Lab on a Chip* 16.13 (June 22, 2016). Publisher: The Royal Society of Chemistry, pp. 2434–2439. DOI: 10.1039/C6LC00463F.

[102] Alexander M. Xu et al. “Direct Intracellular Delivery of Cell-Impermeable Probes of Protein Glycosylation by Using Nanostraws”. In: *Chembiochem: A European Journal of Chemical Biology* 18.7 (2017), pp. 623–628. DOI: 10.1002/cbic.201600689.

[103] Xiaojie Duan et al. “Intracellular recordings of action potentials by an extracellular nanoscale field-effect transistor”. In: *Nature Nanotechnology* 7.3 (Mar. 2012). Number: 3 Publisher: Nature Publishing Group, pp. 174–179. DOI: 10.1038/nnano.2011.223.

[104] J. A. George et al. “Biomimetic sensory feedback through peripheral nerve stimulation improves dexterous use of a bionic hand”. In: *Science Robotics* 4.32 (July 24, 2019). Publisher: Science Robotics Section: Research Article. DOI: 10.1126/scirobotics.aax2352.

[105] Yuqian Ma et al. “Mammalian Near-Infrared Image Vision through Injectable and Self-Powered Retinal Nanoantennae”. In: *Cell* 177.2 (Apr. 2019), 243–255.e15. DOI: 10.1016/j.cell.2019.01.038.

[106] Bozhi Tian et al. “Three-Dimensional, Flexible Nanoscale Field-Effect Transistors as Localized Bioprobes”. In: *Science* 329.5993 (Aug. 13, 2010). Publisher: American Association for the Advancement of Science Section: Report, pp. 830–834. DOI: 10.1126/science.1192033.

[107] Bozhi Tian et al. “Macroporous nanowire nanoelectronic scaffolds for synthetic tissues”. In: *Nature Materials* 11.11 (Nov. 2012), pp. 986–994. DOI: 10.1038/nmat3404.

[108] Anqi Zhang and Charles M. Lieber. “Nano-Bioelectronics”. In: *Chemical Reviews* 116.1 (Jan. 13, 2016). Publisher: American Chemical Society, pp. 215–257. DOI: 10.1021/acs.chemrev.5b00608.

[109] Yi Cui et al. “Diameter-controlled synthesis of single-crystal silicon nanowires”. In: *Applied Physics Letters* 78.15 (Apr. 9, 2001), pp. 2214–2216. DOI: 10.1063/1.1363692.

[110] S. Sharma, T.I. Kamins, and R. Stanley Williams. "Synthesis of thin silicon nanowires using gold-catalyzed chemical vapor deposition". In: *Applied Physics A* 80.6 (Mar. 1, 2005), pp. 1225–1229. DOI: 10.1007/s00339-004-3155-3.

[111] Jacques I. Pankove. *Optical Processes in Semiconductors*. 2nd. Dover Publications, 1975. 448 pp. ISBN: 978-0-486-60275-2.

[112] Edwin J. Yoo et al. "Gα12 facilitates shortening in human airway smooth muscle by modulating phosphoinositide 3-kinase-mediated activation in a RhoA-dependent manner". In: *British Journal of Pharmacology* 174.23 (2017), pp. 4383–4395. DOI: 10.1111/bph.14040.

[113] Omar Tliba and Reynold A. Panettieri. "Noncontractile Functions of Airway Smooth Muscle Cells in Asthma". In: *Annual Review of Physiology* 71.1 (2009). _eprint: https://doi.org/10.1146/annurev.physiol.010908.163227, pp. 509–535. DOI: 10.1146/annurev.physiol.010908.163227.

[114] Gautam Damera, Omar Tliba, and Reynold A. Panettieri. "Airway smooth muscle as an immunomodulatory cell". In: *Pulmonary Pharmacology & Therapeutics* 22.5 (Oct. 2009), pp. 353–359. DOI: 10.1016/j.pupt.2008.12.006.

[115] Alaina J. Ammit et al. "Sphingosine 1-phosphate modulates human airway smooth muscle cell functions that promote inflammation and airway remodeling in asthma". In: *The FASEB Journal* 15.7 (Mar. 20, 2001). Publisher: Federation of American Societies for Experimental Biology, pp. 1212–1214. DOI: 10.1096/fj.00-0742fje.

[116] Brian GG Oliver et al. "Increased proinflammatory responses from asthmatic human airway smooth muscle cells in response to rhinovirus infection". In: *Respiratory Research* 7.1 (May 3, 2006), p. 71. DOI: 10.1186/1465-9921-7-71.

[117] Simon Hirota et al. "Airway smooth muscle excitation-contraction coupling and airway hyperresponsiveness". In: *Canadian Journal of Physiology and Pharmacology*

83.8 (Aug. 1, 2005). Publisher: NRC Research Press, pp. 725–732. DOI: 10.1139/y05-070.

[118] Girolamo Pelaia et al. "Molecular mechanisms underlying airway smooth muscle contraction and proliferation: Implications for asthma". In: *Respiratory Medicine* 102.8 (Aug. 1, 2008), pp. 1173–1181. DOI: 10.1016/j.rmed.2008.02.020.

[119] R. K. Murray and M. I. Kotlikoff. "Receptor-activated calcium influx in human airway smooth muscle cells." In: *The Journal of Physiology* 435.1 (1991). _eprint: https://onlinelibrary.wiley.com/doi/pdf/10.1113/jphysiol.1991.sp018501, pp. 123–144. DOI: 10.1113/jphysiol.1991.sp018501.

[120] Cheng-Han Lee et al. "Asynchronous calcium waves in smooth muscle cells". In: *Canadian Journal of Physiology and Pharmacology* 83.8 (Aug. 1, 2005). Publisher: NRC Research Press, pp. 733–741. DOI: 10.1139/y05-083.

[121] M Iino, H Kasai, and T Yamazawa. "Visualization of neural control of intracellular Ca2+ concentration in single vascular smooth muscle cells in situ." In: *The EMBO Journal* 13.21 (Nov. 1, 1994), pp. 5026–5031.

[122] Albrecht Bergner and Michael J. Sanderson. "Acetylcholine-induced Calcium Signaling and Contraction of Airway Smooth Muscle Cells in Lung Slices". In: *Journal of General Physiology* 119.2 (Feb. 1, 2002), pp. 187–198. DOI: 10.1085/jgp.119.2.187.

[123] Y. Asada et al. "Dynamic Ca2+ signalling in rat arterial smooth muscle cells under the control of local renin-angiotensin system". In: *The Journal of Physiology* 521 Pt 2 (Dec. 1, 1999), pp. 497–505. DOI: 10.1111/j.1469-7793.1999.00497.x.

[124] Serguei Y. Cheranov and Jonathan H. Jaggar. "Mitochondrial modulation of Ca2+ sparks and transient KCa currents in smooth muscle cells of rat cerebral arteries". In: *The Journal of Physiology* 556 (Pt 3 May 1, 2004), pp. 755–771. DOI: 10.1113/jphysiol.2003.059568.

[125] Yasuyo Kasai et al. “Endothelium-dependent frequency modulation of Ca2+ signalling in individual vascular smooth muscle cells of the rat”. In: *The Journal of Physiology* 504.2 (1997), pp. 349–357. DOI: 10.1111/j.1469-7793.1997.349be.x.

[126] Qiang Li et al. “Cyborg Organoids: Implantation of Nanoelectronics via Organogenesis for Tissue-Wide Electrophysiology”. In: *Nano Letters* 19.8 (Aug. 14, 2019). Publisher: American Chemical Society, pp. 5781–5789. ISSN: 1530-6984. DOI: 10.1021/acs.nanolett.9b02512. (Visited on 07/09/2020).

[127] Anna Kalmykov et al. “Organ-on-e-chip: Three-dimensional self-rolled biosensor array for electrical interrogations of human electrogenic spheroids”. In: *Science Advances* 5.8 (Aug. 1, 2019). Publisher: American Association for the Advancement of Science Section: Research Article, eaax0729. ISSN: 2375-2548. DOI: 10.1126/sciadv.aax0729. (Visited on 07/09/2020).

[128] John Devany et al. *Cell division Rate Controls Cell Shape Remodeling in Epithelia*. preprint. Biophysics, Oct. 14, 2019. DOI: 10.1101/804294.

[129] Aldrin V. Gomes, James D. Potter, and Danuta Szczesna-Cordary. “The role of troponins in muscle contraction”. In: *IUBMB life* 54.6 (Dec. 2002), pp. 323–333. DOI: 10.1080/15216540216037.

[130] Ming Jin et al. “Ca2+-Dependent Regulation of Rho GTPases Triggers Turning of Nerve Growth Cones”. In: *Journal of Neuroscience* 25.9 (Mar. 2, 2005). Publisher: Society for Neuroscience Section: Development/Plasticity/Repair, pp. 2338–2347. DOI: 10.1523/JNEUROSCI.4889-04.2005.

[131] Alex Veksler and Nir S. Gov. “Calcium-Actin Waves and Oscillations of Cellular Membranes”. In: *Biophysical Journal* 97.6 (Sept. 16, 2009), pp. 1558–1568. DOI: 10.1016/j.bpj.2009.07.008.

[132] Bertrand Coste et al. “Piezo proteins are pore-forming subunits of mechanically activated channels”. In: *Nature* 483.7388 (), pp. 176–181. DOI: 10.1038/nature10812.

[133] Charles D. Cox et al. “Removal of the mechanoprotective influence of the cytoskeleton reveals PIEZO1 is gated by bilayer tension”. In: *Nature Communications* 7.1 (), p. 10366. DOI: 10.1038/ncomms10366.

[134] Mirko Moroni et al. “Voltage gating of mechanosensitive PIEZO channels”. In: *Nature Communications* 9.1 (), p. 1096. DOI: 10.1038/s41467-018-03502-7.

[135] Ruhma Syeda et al. “Piezo1 Channels Are Inherently Mechanosensitive”. In: *Cell Reports* 17.7 (Nov. 8, 2016), pp. 1739–1746. DOI: 10.1016/j.celrep.2016.10.033.

[136] Carlos Pardo-Pastor et al. “Piezo2 channel regulates RhoA and actin cytoskeleton to promote cell mechanobiological responses”. In: *Proceedings of the National Academy of Sciences* 115.8 (Feb. 20, 2018). Publisher: National Academy of Sciences Section: Biological Sciences, pp. 1925–1930. DOI: 10.1073/pnas.1718177115.

[137] Kyle L. Ellefsen et al. “Myosin-II mediated traction forces evoke localized Piezo1-dependent Ca 2+ flickers”. In: *Communications Biology* 2.1 (Aug. 7, 2019). Number: 1 Publisher: Nature Publishing Group, pp. 1–13. DOI: 10.1038/s42003-019-0514-3.

[138] Kate E. Cavanaugh, Patrick W. Oakes, and Margaret L. Gardel. “Optogenetic Control of RhoA to Probe Subcellular Mechanochemical Circuitry”. In: *Current Protocols in Cell Biology* 86.1 (). DOI: 10.1002/cpcb.102.

[139] Kate E. Cavanaugh et al. “RhoA Mediates Epithelial Cell Shape Changes via Mechanosensitive Endocytosis”. In: *Developmental Cell* 52.2 (), 152–166.e5. DOI: 10.1016/j.devcel.2019.12.002.

[140] Ricard Alert and Xavier Trepat. “Physical Models of Collective Cell Migration”. In: *Annual Review of Condensed Matter Physics* 11.1 (2020), pp. 77–101. DOI: 10.1146/annurev-conmatphys-031218-013516. (Visited on 06/02/2020).

[141] Chad Bouton. “Neural Decoding and Applications in Bioelectronic Medicine”. In: *Bioelectronic Medicine* 2.1 (), pp. 20–24. DOI: 10.15424/bioelectronmed.2014.00012.

[142] ThomasGeorge Olsen et al. “Diagnostic performance of deep learning algorithms applied to three common diagnoses in dermatopathology”. In: *Journal of Pathology Informatics* 9.1 (), p. 32. DOI: 10.4103/jpi.jpi_31_18.

[143] Albert P. Bartók et al. “Machine Learning a General-Purpose Interatomic Potential for Silicon”. In: *Physical Review X* 8.4 (), p. 041048. DOI: 10.1103/PhysRevX.8.041048.

[144] Volker L. Deringer et al. “Realistic Atomistic Structure of Amorphous Silicon from Machine-Learning-Driven Molecular Dynamics”. In: *The Journal of Physical Chemistry Letters* 9.11 (), pp. 2879–2885. DOI: 10.1021/acs.jpclett.8b00902.

[145] Paul J. McGinn. “Thin-Film Processing Routes for Combinatorial Materials Investigations—A Review”. In: *ACS Combinatorial Science* 21.7 (), pp. 501–515. DOI: 10.1021/acscombsci.9b00032.

[146] Jessica Vamathevan et al. “Applications of machine learning in drug discovery and development”. In: *Nature Reviews Drug Discovery* 18.6 (), pp. 463–477. DOI: 10.1038/s41573-019-0024-5.

[147] Giuseppe Carleo et al. “Machine learning and the physical sciences”. In: *Reviews of Modern Physics* 91.4 (), p. 045002. DOI: 10.1103/RevModPhys.91.045002.